

Hopper Railcars: A Preliminary Study on the use of Fibre Reinforced Polymers in Structural Components

by

Sadeem Faisal Al Attar, B.Eng.

A thesis submitted to the Faculty of Graduate and Postdoctoral Affairs in partial fulfillment of the requirements for the degree of

Master of Applied Science

in

Aerospace Engineering

Carleton University
Ottawa, Ontario

© 2015

Sadeem Al Attar

..... There is a famous saying by an educator that goes like this, “*there are one million reasons not to do something*”. This project taught me that you only need one reason to do something.

Dedicated to the dearest person to my heart, to my role model

.... My father

Abstract

Transport Canada is investing in research areas and enforcing new regulations to enable the Government of Canada fulfil its commitment in reducing the nation's total greenhouse gas emissions. This research was supported in part by Transport Canada's Clean Rail Academic Grant Program to develop and apply new technologies that can reduce the weight of railcars, which lead to reduction in greenhouse gas emissions in the Canadian rail sector.

A piece cut from a decommissioned hopper railcar was determined to be a low-carbon steel with experimentally determined mechanical properties through a series of metallographic, tensile, and hardness tests. A 6.4% potential weight reduction in the structural weight of a hopper railcar was achieved by using aramid/epoxy, fabricated using vacuum assisted resin transfer moulding, as a substitute material for the low-carbon steel in the sidewalls. Structural analysis was performed using ABAQUS to insure a safe design that meets the requirements set by the Association of American Railroads. Further work can be done to study the environmental effects on the performance parameters of selected composite material.

Acknowledgements

I would like to express my sincere gratitude to my advisor Prof. Jeremy Laliberte for his selfless time and care that kept me going. I am grateful for the motivation, enthusiasm, and immense knowledge I received from him. He was always available for me when I needed him for mentoring or advice. I am forever in your debt.

Special thanks to Steve Truttmann, Alex Proctor and Ian Lloy for assisting me with my experiments throughout my academic career. Their help and accommodations were greatly appreciated.

I would like to also thank Transport Canada's Clean Rail Academic Grant for providing me with this opportunity and the majority of my funding.

Special thanks for David Gill, from Gerdau Long Steel North America, for providing me with the steel plate removed from a decommissioned grain hopper railcar. His help put an end to a long and exhausting search for critical information.

Last but not least, I would like to thank my family for their support in all its forms. Without them, I would not have been able to finish this project. Special thanks to my not so-little-brother Sayar Al Attar for helping me keep my sanity.

Table of Contents

Abstract	ii
Acknowledgements.....	iii
List of Tables.....	vii
List of Illustrations.....	viii
Nomenclature	xiii
Chapter 1 Introduction	1
1.1 Thesis Motivation	2
1.2 Thesis Objectives	4
1.3 Thesis Overview	4
Chapter 2 Review of the Canadian Rail System Operations and State-of-the-Art Technologies	6
2.1 Association of American Railroads Car Classification Code	6
2.2 Railway Performance	8
2.2.1 Cars On line	8
2.2.2 Carloads Weekly Trends	9
2.3 Carload and Accommodating Car Type	10
2.4 Locomotive Emissions in Canada	11
2.4.1 Transport Canada-RAC Memorandum of Understanding	11
2.4.1.1 Action Plan	12
2.4.1.2 Canadian Locomotive Emission Monitoring Program	12

2.4.2	Emission Assessment	13
2.5	Design Trends in Freight Cars	14
Chapter 3 Design Requirements & General Hopper Design		18
3.1	Design of Typical Hopper Cars	18
3.2	Design requirements	22
Chapter 4 Material and Fabrication Process Selection		24
4.1	Typical Hopper Railcar	24
4.1.1	Hardness Testing of Steel Hopper Railcar Specimens	27
4.1.2	Uniaxial Tensile Testing of Steel Hopper Railcar Specimens	30
4.1.3	Optical Microscopy	37
4.1.4	Results and Discussion	41
4.2	Fibre Reinforced Polymer Options	42
4.3	Fabrication Processes	45
4.3.1	VARTM Fabrication Processes	51
4.3.2	Effects of Manufacturing On the Quality and Performance of the Final Product	53
4.4	VARTM Fabrication Trials	55
4.4.1	VARTM Process Trial Methodology	55
4.4.2	VARTM Process Trial results and Discussion	57
Chapter 5 Structural Analysis of Improved Sidewall Design		62
5.1	Thin Plate Theory and Comparison to Finite Element Analysis	62
5.2	FEA Setup and Assumptions	71

5.3	FE Analysis of Steel and FRP Side Panels	73
5.4	Structural Analysis Results and Discussion	75
Chapter 6	Conclusions	81
6.1	Conclusions	81
6.2	Recommendations	82
References		85
A	Weekly Railroad Traffic Carload and Intermodal Traffic Category Definitions	94
B	Specifications of All Published North American Existing Hopper Cars	97
C	Setup for VARTM manufacturing	99
D	FE Analysis of a Thin Plate Model Using ABAQUS	101

List of Tables

Table 1: A list of some AAR freight car types and their corresponding codes relevant to research [7].....	7
Table 2: Typical cargo of railcars according to types, deduced from [11] and CN’s main website:	11
Table 3: List of critical design requirements.	23
Table 4: Hardness numbers obtained using 1/16th inch diameter steel ball, scale B, and 100kg major load.....	29
Table 5: conversion of the average HRB values to tensile strength of each sample in Table 4.	30
Table 6: Summary of the key mechanical properties obtain from the uniaxial tensile testing.....	36
Table 7: Summary of the key mechanical properties obtained from hardness and tensile testing.....	41
Table 8: Common fibre material properties [37] [30].	43
Table 9: Comparison between the mechanical properties of Advanced Vacuum Assisted Resin Transfer Moulding and prepreg materials [44].	48
Table 10: material strength reduction in composite with void volume content in the range 0 - 4% [54].....	54
Table 11: Mesh convergence for a simply supported plate under bending.	69
Table 12: Summary of the results obtained from ABAQUS and thin plate theory for different boundary condition at the same number of elements, 25000.	71
Table 13: Summary of key results obtained from FE analysis.	77

List of Illustrations

Figure 1: Canada's emissions breakdown by intergovernmental sectors for the year 2013 [3].....	1
Figure 2: Research path taken to identify areas of interest.....	3
Figure 3: An average weekly number for each car type of Cars On Line for CP and CN Railways (for the weeks ending from 31 Jan 2014 to 24 Oct 2014) [8].....	9
Figure 4: The total commodity grouping of shipped goods by CN and CP Railways for the year 2013 [9].....	10
Figure 5: Plotted values of emission intensity, from the LEM reports, from 1990 to 2011 [14].....	13
Figure 6: Glasshopper, the first reinforced plastic covered hopper (overall length: 16.15 m) [19].....	15
Figure 7: Composite hopper car body produced by vacuum infusion (overall length: 13.7 m) [21].....	16
Figure 8: Walmart's concept truck. Picture depicting the trailer (overall length: 16.15 m) [22].	17
Figure 9: Common goods transported via a Hopper freight car [23].	19
Figure 10: Covered hopper railcar with cylindrical sidewalls [24].	20
Figure 11: Covered hopper railcar with flat sidewalls [25].	20
Figure 12: Hopper car with its main components labelled [27].	21
Figure 13: A 1 m X 0.72 m steel plate cut from the sidewall of a decommissioned hopper car.	25
Figure 14: Location and orientation of the test specimens used in for the tensile, hardness, and metallography tests.	26
Figure 15: A Rockwell device with a diamond indenter.	28

Figure 16: Rockwell device with a 1/16 th in steel ball.	28
Figure 17: Test specimen geometry obtained from ASTM E8, all units are in millimetre.	31
Figure 18: Test specimen showing the location of the two perpendicular strain gauges.	31
Figure 19: Final setup with the strain gauges and extensometer.....	31
Figure 20: MTS 810 Test System, 100 kN, used to conduct the tensile tests.....	32
Figure 21: P3 Strain Indicator and Recorder used to collect readings from the strain gauges.	33
Figure 22: schematic representation of typical stress-strain behaviour found for some steels [30]......	35
Figure 23: Plotted values for the engineering stress-strain curve of the unknown steel for sample #1.....	35
Figure 24: The linear (elastic region) from Figure 23.	36
Figure 25: Data point corresponding to tensile strength values from Table 6; error bars indicate the degree of scatter corresponding to the average tensile strength value plus and minus the standard deviation.	36
Figure 26: The initial and final stage of sample preparation for sample 1 (a,d), sample 2 (b,e), and sample 3 (c,f)	38
Figure 27: Microstructure graph of a cold worked metal sample [35]......	39
Figure 28: The microstructure images of each face from the three samples.	40
Figure 29: Microstructure images of a) AISI 1018 b) AISI 1020 and c) AISI 1045 [36].	42
Figure 30: A short list of benefits and disadvantages of each of the relevant fabrication processes sorted ascendingly from left to right in terms of quality and cost.	46

Figure 31: An illustrative comparison between Autoclave and VARTM manufacturing [44].....	47
Figure 32: Cost comparison for MRJ empennage box structure [39].	49
Figure 33: Cost per process showing contributions from equipment, tools, labours, energy, and consumables [40].....	50
Figure 34: Total CO ₂ eq emissions related to energy use during processing showing contributions from cutting, de-bulking, cure, and oven operation [40].....	51
Figure 35: schematic diagram of a typical VAP setup [51].....	52
Figure 36: Schematic diagram of the CAPRI setup [52].....	52
Figure 37: schematic diagram of SCRIMP setup [51].	53
Figure 38: Schematic illustration of the setup of the VARTM process.	55
Figure 39: VARTM setup for a fibreglass panel, 0.33 m X 0.33 m.	56
Figure 40: VARTM setup for a carbon fibre panel, 0.15 m X 0.15 m.	56
Figure 41: Fibreglass panel manufactured using VARTM showing major manufacturing defects.....	57
Figure 42: Top surface showing irregularities and roughness from contact with the distribution medium.....	58
Figure 43: Bottom surface showing smoothness from contact with the tool.....	58
Figure 44: The bottom view of the first produced fibreglass panel showing the location of dry spots.....	59
Figure 45: The bottom view of the last produced fibreglass panel showing the location of dry spots.....	60
Figure 46: Inlet and distribution channel location caused the resin to flow straight to the outlet port.	61

Figure 47: schematic representation of the Kirchhoff assumptions for unreformed and deformed geometrics edge of a plate [59].....	63
Figure 48: Positive shear forces and moments and distributed lateral load, q [N], shown on a plate element [60].....	66
Figure 49: Convergence curve of stress based on the number of elements.	69
Figure 50: Stress distribution, in Pa, of a simply supported thin plate under 2600 Pa transverse pressure.....	70
Figure 51: Deflection plot, in m, of a simply supported thin plate under 2600 Pa transverse pressure.....	70
Figure 52: Front view of a complete sidewall built in ABAQUS.	72
Figure 53: shell model of the steel plate with clamped condition at the bottom and simply supported everywhere else.....	73
Figure 54: The stress distribution, in psi and MPa, shown on the front view of the steel panel.....	76
Figure 55: Deflection of the steel panel, in inches and m.....	77
Figure 56: Open hopper railcar with a hybrid steel and aluminium design [63].	79
Figure 57: schematic illustration of the main failure modes in bolted joints if FRP [37].	80
Figure 58: [0/90/0/0/90/0] stacking sequence of the fibreglass preform.	99
Figure 59: Placement of Peel Ply (green film) under the Distribution Medium (red mesh) and the breather cloth (white fabric).	100
Figure 60: Placement of the resin distribution channel to the left side for the inlet under the peel ply.	100
Figure 61: Stress distribution, in 2600 Pa, for a steel plate with SSSS boundary conditions.....	101

Figure 62: Stress distribution, in 2600 Pa, for a steel plate with CCSS boundary conditions.....	102
Figure 63: Stress distribution, in 2600 Pa, for a steel plate with SSCC boundary conditions.....	102
Figure 64: Stress distribution, in 2600 Pa, for a steel plate with CCCC boundary conditions.....	103

Nomenclature

Abbreviations:

GHG	Greenhouse Gas
RAC	Railway Association of Canada
CN	Canadian National
CP or CPR	Canadian Pacific Railway
CAC	Criteria Air Contaminates
MOU	Memorandum of Understanding
RTK	Revenue Tonne Kilometers
GTK	Gross Tonne Kilometers
LEM	Locomotive Emissions Monitoring
AAR	Association of American Railroads
FAA	Federal Aviation Administration
MSRP	Manual of Standards and Recommended Practices
FRP	Fibre-Reinforced Polymer
OoA	Out of Autoclave
AISI	American Iron and Steel Institute
HR	Rockwell Hardness
ASTM	American Society for Testing and Materials
HB	Brinell hardness
TS	Tensile Strength
LRM	Liquid Resin Moulding
LCM	Low-Cost Manufacturing
RI	Resin Infusion

MRJ	Mitsubishi Regional Jet
VARTM	Vacuum Assisted Resin Transfer Moulding
CV	Coefficient of Variation
VAP	Vacuum-Assisted Process
CAPRI	Controlled Atmospheric Pressure Resin Infusion
SCRIMP	Seemann Composites Resin Infusion Moulding Process
SSSS	All sides simply supported
CCSS	long sides simply supported and short sides clamped
SSCC	short sides simply supported and long sides
CCCC	all sides clamped
LIMS	Liquid Injection Molding Simulation

Latin Symbols:

P	Lateral force	[N/m of length]
W	Specific weight of lading	[N/m ³]
h	Depth of lading	[m]
\emptyset	Static angle of repose	[25°]
TS_{STD}	Standard Deviation of tensile strength	[MPa]
l_0	Initial gauge length	[mm]
Δl	Change in length at some instant	[mm]
A_0	Cross-sectional area	[mm ²]
σ	Engineering stresses	[MPa]
F	Instantaneous axial load	[N]
ϵ	Engineering Strain	-

ν	Poisson's ratio	-
E	Modulus of Elasticity or Young's Modulus	[GPa]
σ_y	Yield strength	[MPa]
V_f	Fibre volume fraction	-
ρ_c	Theoretical density	[kg/m ³]
w_f	Fibre weight fraction	-
w_m	Matrix weight fraction	-
ρ_f	Fibre density	[kg/m ³]
ρ_m	Matrix density	[kg/m ³]
V_v	Voids volume fraction	-
ρ	Density	[kg/m ³]
u, v, w	Displacement in x direction	[m]
v	Displacement in y direction	
w	Displacement in z direction	
τ_{xy}	Shear stress	[MPa]
G	Shear modulus	[GPa]
γ_{xy}	Shear Strain	-
Q_x, Q_y	Shear forces	[N per unit length]
M_x, M_y	Bending moment	[Nm per unit length]
M_{xy}	Twisting moment	[Nm per unit length]
h	Height of element	[m]

Chapter 1

Introduction

The Canadian rail system handles the fourth largest volume of goods in the world and is the fifth largest network in the world [1], with approximately 48,000 km of track. It moves more than 80% of surface goods in Canada [2].

Figure 1 shows the breakdown of the nation's greenhouse gas (GHG) emissions for the year 2013 [3]. Canada's transportation sector produces 28% of the GHG emissions, where less than 3.5% of that total is produced from rail. In other words, the rail transportation system itself produces less than 1% of the national (GHG) emissions portfolio [2] [3]. Additionally, Canada only accounts for 2% of global GHG emissions [4].

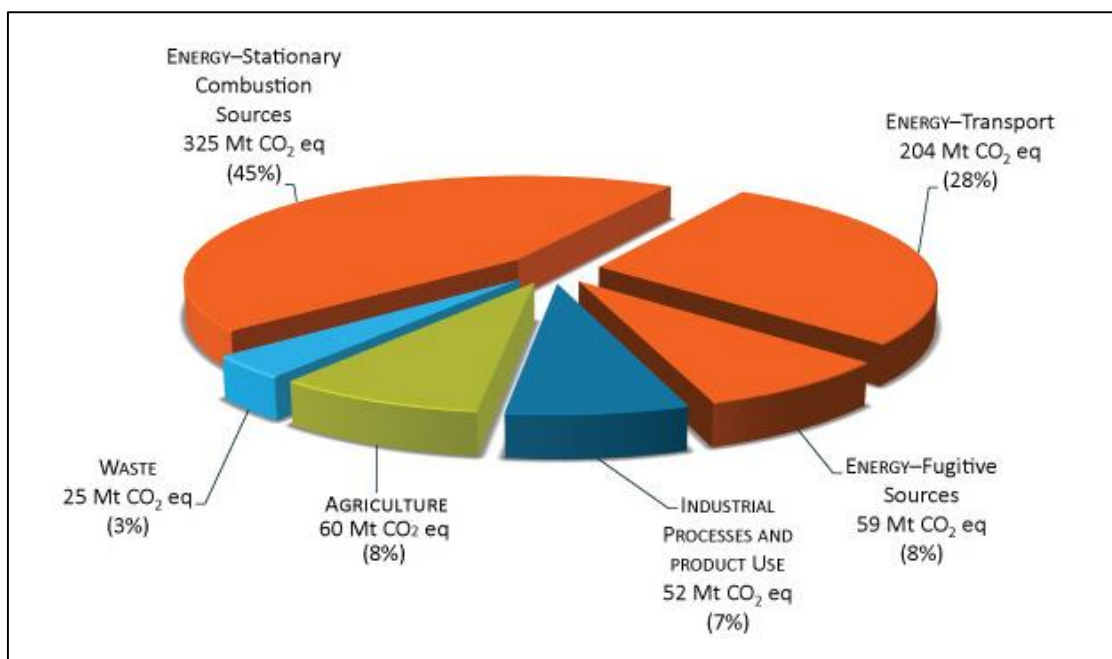


Figure 1: Canada's emissions breakdown by intergovernmental sectors for the year 2013 [3].

These figures seem favourable in their own right, but Canada's *per capita* emission rate is among the highest in the world [3]. The Government of Canada developed and is implementing regulatory measures, listed under Canada's Clean Air Act, to improve the domestic situation. In fact, the Government of Canada has committed to reduce the nation's total GHG emissions by 17% of 2005 levels by 2020 while keeping the economy strong [2]. Transport Canada, therefore, is doing its part to enforce these regulations and invest in research areas to reduce Canada's carbon footprint.

1.1 Thesis Motivation

This research is supported in part by Transport Canada's Clean Rail Academic Grant Program to support research and development projects that aim to develop and apply new technologies that will reduce GHG emissions in the Canadian rail sector. The research described in this thesis focuses on the use of composite materials to reduce the structural weight of freight cars to increase the lading capacity (lading is bulk commodities in the form of ore, aggregate, granules, grain, ash or pellets [5]) and thus improve the overall network fuel efficiency. In particular, the composite material technologies explored are well-established and proven in the aerospace sector. Figure 2 illustrates the top-down method taken by this research to reach to a specific research topic.

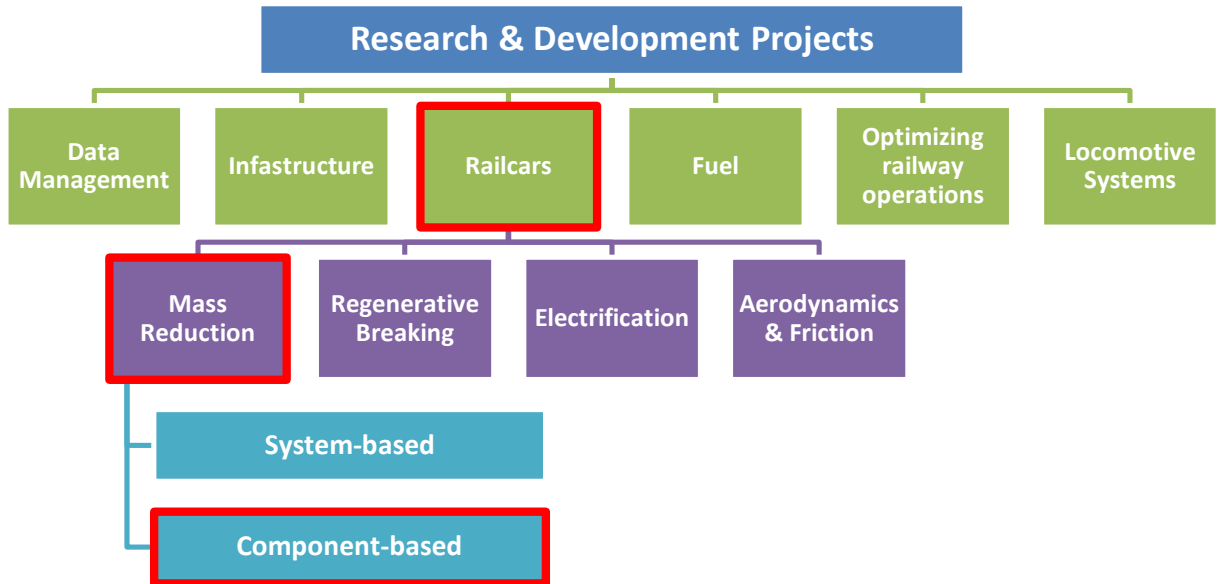


Figure 2: Research path taken to identify areas of interest.

It is very important to point out early on that estimating savings in energy consumption, GHG emissions, or operating costs is extremely difficult in the rail sector. For instance, railway operators constantly share freight cars and do not have a fixed number of railcars on each trip. There are studies such as the ongoing RailEnergy Project¹, which seeks to recognise the interaction between infrastructure, train operating companies, regulators, and manufacturers in the European Union. This is beyond the scope of this project but important to understand before continuing with the research.

Therefore, the objective of this research is to investigate the effect of lightweighting the structural components on a single freight railcar through material substitution. Estimating weight saving per car is more attainable and qualitatively more beneficial for railcar operators. There are different types of railcars used by Canadian railcar operators for different applications. Hence, a market survey was conducted to

¹ Further information about this project is presented on their main website: www.railenergy.eu

help determine which of these types is most operated by Canadian rail operators. By doing so, lightweighting these railcars will ensure the greatest energy savings impact across the fleet.

1.2 Thesis Objectives

The specific objectives of this research were:

- To increase the understanding of the Canadian rail system and perform a study of the state-of-the-art technologies and advancements in global railcar designs;
- To determine the performance parameters of the materials used in the sidewall structures of current hopper cars;
- To select an applicable fabrication process for the proposed new fibre reinforced sidewall based on the study of existing manufacturing methods. Also, to perform fabrication trials to identify specific challenges with the chosen fabrication process for future studies;
- To perform numerical structural analysis on the new design configuration part(s) in accordance with the requirements and standards of the Association of American Railroads to determine the layup of the fibre reinforced polymers; and,
- To estimate the potential structural weight savings in a hopper railcar from using fibre reinforced polymers in comparison to the steel baseline railcar.

1.3 Thesis Overview

This thesis presents a review of the Canadian rail system operation and function to help formulate a solution to meet the emissions target set by the Government of Canada. In addition, a review of novel design ideas and state-of-the-art technologies considered by

global freight car manufacturers were carefully investigated. The objective to reduce the structural weight of each railcar set forth various experiments and design efforts to substitute current materials with fibre reinforced polymers. This thesis is organized into the following chapters:

- Chapter 2** - details the literature review regarding railcar industries, standards, performance parameters, and design trends.
- Chapter 3** - review of the relevant design requirements and standards for hopper railcars set by the Association of American Railroads.
- Chapter 4** - results of key mechanical properties obtained from a piece cut from the sidewall of a steel hopper railcar. In addition, a discussion of relevant fabrication processes and results of fabrication trials using vacuum assisted resin transfer mould.
- Chapter 5** - results of estimated weight reduction in hopper railcars predicted from performing finite element analysis on improved fibre reinforced polymer sidewalls.
- Chapter 6** - conclusion from the project and recommendations for future work.

Chapter 2

Review of the Canadian Rail System Operations and State-of-the-Art Technologies

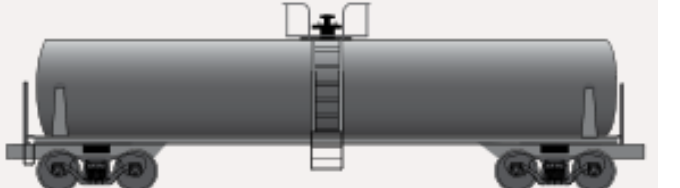
The Railway Association of Canada (RAC) recognizes three Canadian Class I railway members: Canadian National (CN), Canadian Pacific Railway (CPR or CP), and VIA Rail. Combined, these members consume approximately 94% of all locomotive diesel fuel burned in Canada [6]. The CP and CN are freight railcar operators who ship products (such as grains, oil, other bulk commodities and intermodal containers) across Canada and the USA, whereas VIA Rail is the primary intercity passenger rail operator within Canada. Determining the impact of improving an intercity passenger railcar was found to be complex to quantify the network efficiency due to its dependence on fluctuating number of passengers per ride. Also, changes in the structural components, such as the outer shell, were interlinked with various health and safety requirements and standards. Hence, the research conducted hereafter will focus solely on the performance parameters of the two freight railways, CP and CN, and include relevant information on freight railcars.

2.1 Association of American Railroads Car Classification Code

The Association of American Railroads (AAR) has designated special car classification codes for each freight car type to be used in a computerized traffic-generated program. That is, these classifications are used to track the prototypical operation of each classification to be categorised in terms of weekly railroad performance measures.

Table 1 lists the car types, and their code, relevant to this research.

Table 1: A list of some AAR freight car types and their corresponding codes relevant to research [7].

Code	Freight Car Type	
C	<p>Covered Hopper</p> <p><i>(Grain & Fertilizers, Forest Products, Metals & Minerals)</i></p>	
H, J or K	<p>Open Hopper</p> <p><i>(Coal, Forest Products, Metals & Minerals)</i></p>	
G or E	<p>Gondola</p> <p><i>(Coal, Forest Products, Metals & Minerals)</i></p>	
P, Q or S	<p>Intermodal</p> <p><i>(Grain & Fertilizers, Forest Products, Metals & Minerals)</i></p>	
T	<p>Tank</p> <p><i>(Grain & Fertilizers, Forest Products, Petroleum & Chemicals)</i></p>	

2.2 Railway Performance

The CP and CN railways voluntarily report their railroad performance, number of cars on line and carloads data, on a weekly basis to the Association of American Railroads. This information is also accessible to the public on CP and CN websites².

These railroad performance measures can be used as indicators of some railroad performances, such as most frequently used freight car type. By knowing which product group is shipped, the AAR guidelines determine which freight car type is used the most. Hence, this data will be relied on to aid in the selection of the most frequently used type of freight car for possible redesign and lightweighting based on the assumption that the most common cars will also contribute the largest proportion of GHG production.

2.2.1 Cars On line

This weekly report lists the following key performance parameters:

1. AAR Cars On Line, by owner and car type;
2. Average Train Speed (mph); and,
3. Terminal Dwell.

Averaging out the number of Cars On Line, by car type, for the weeks ending from 31 Jan 2014 to 24 Oct 2014 shows that the most used car type is Covered Hopper for both CN and CP, refer to Figure 3 below.

² <http://www.cpr.ca/en/investors/key-metrics> and <http://cn.ca/en/investors>

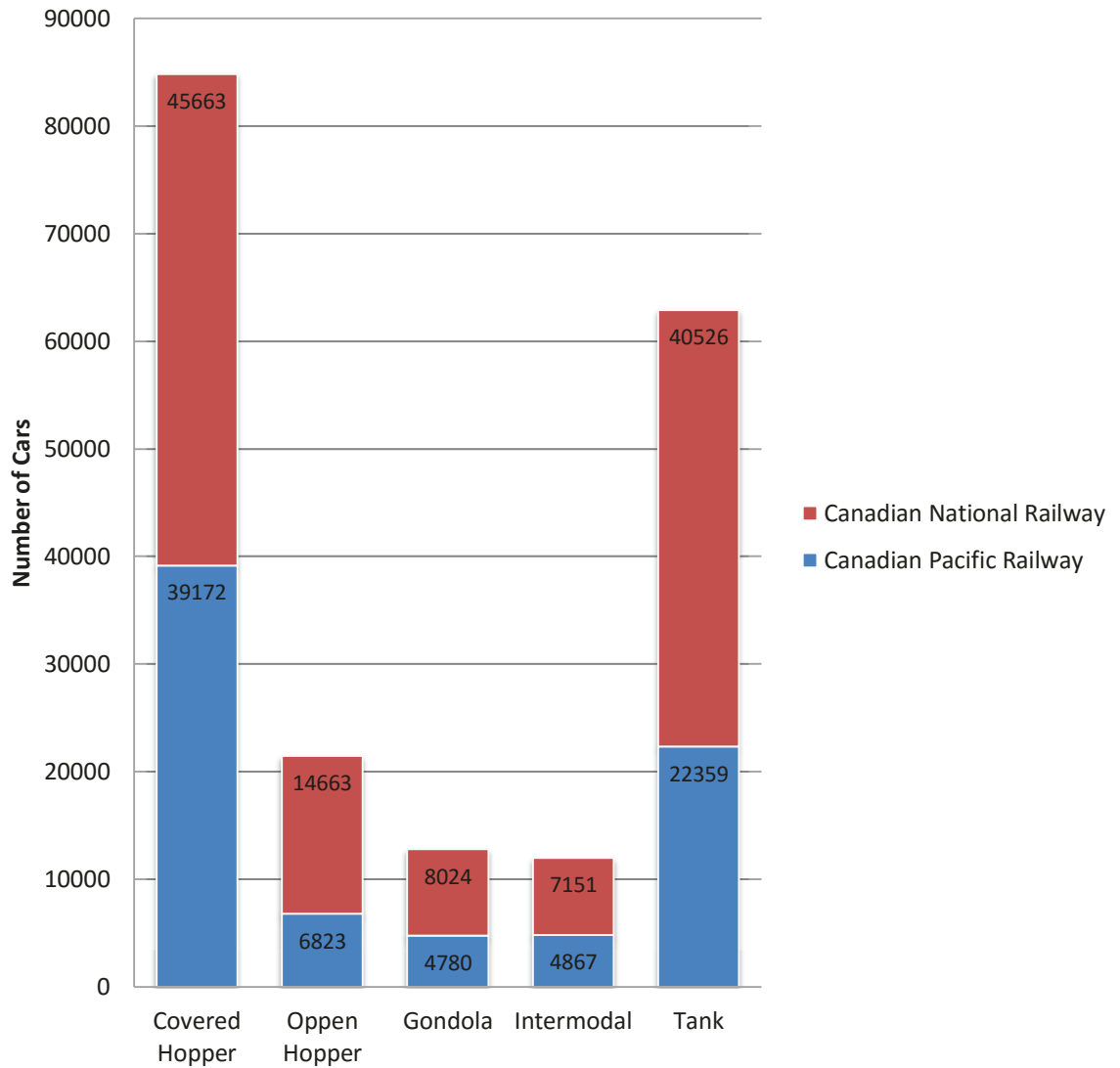


Figure 3: An average weekly number for each car type of Cars On Line for CP and CN Railways (for the weeks ending from 31 Jan 2014 to 24 Oct 2014) [8].

2.2.2 Carloads Weekly Trends

Similar to *Cars on Line*, the *Carload Weekly Reports* for CP and CN can be used to determine which carload type has the highest demand; definition of each category can be found in Appendix A. This parameter can also help in determining which load a car type should be designed to handle. The following figure summarizes the annual carloads originated by commodity grouping for the year 2013 [9]:

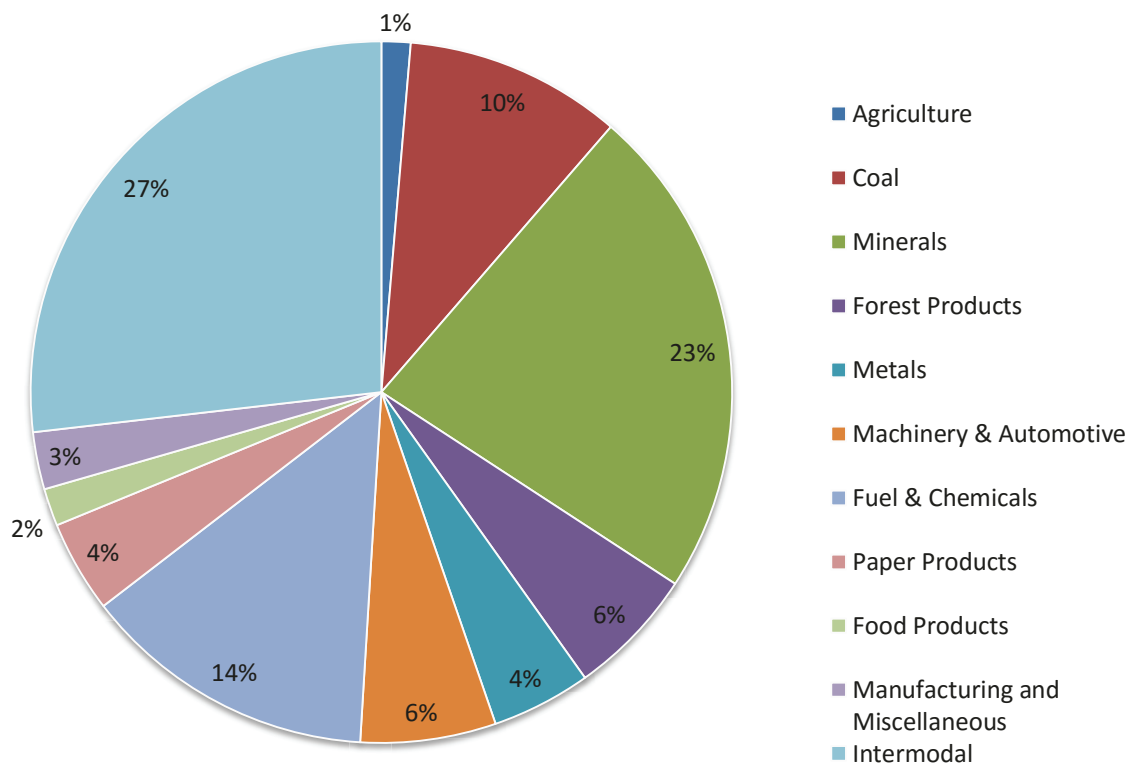


Figure 4: The total commodity grouping of shipped goods by CN and CP Railways for the year 2013 [9].

2.3 Carload and Accommodating Car Type

Some commodity carloads presented in Figure 3 and Figure 4 can be transported using multiple car types. For example: Coal, Coke, Farm Products, Grain, and Grain Mill Products can be grouped under Bulk Products; these products can be transferred using Open Hopper [10]. It is important to note that all, for example, Metals & Minerals can be shipped via any Hopper or Gondola car. In fact, it is the operator's choice to decide on the car type, based on availability.

Table 2: Typical cargo of railcars according to types, deduced from [11] and CN's main website:

	Forest Products	Petroleum & Chemicals	Metals & Minerals	Motor Vehicle & Equip	Coal	Grain
Covered Hopper	X		X			X
Open Hopper	X		X		X	
Gondola	X		X		X	
Tank		X				

2.4 Locomotive Emissions in Canada

Member companies of the Railway Association of Canada (RAC) are voluntarily committing to help Government of Canada meet its targets to reduce the nation's carbon footprint. These companies have been reporting emissions of criteria air contaminants (CAC) and GHGs produced by their locomotives during rail operations in Canada since 2006. This is part of a signed agreement between Transport Canada and RAC which is called the Memorandum of Understanding (MOU) as described in the next section.

2.4.1 Transport Canada-RAC Memorandum of Understanding

The MOU is a five-year voluntary agreement between Canadian rail operators, or member companies of RAC, and Transport Canada which started in 2006, and was renewed in 2011. The rail operators are grouped under three carrier classes: Class I Freight, Intercity Passenger, and Short Lines. The MOU aims to establish targets and actions to reduce the GHG and CAC emissions to protect the environment and health of all Canadians.

At the end of each year, an annual report of CO_{2eq}³ gases, fuel consumption, and further emission-related information is published by the Locomotive Emissions Monitoring (LEM) Program.

2.4.1.1 Action Plan

The Railroad Association of Canada has encouraged its Class I Freight members to reduce their railway operations emissions to 15.45 kg of CO_{2eq} per 1000 revenue tonne kilometers (RTK) by 2015, this is equivalent to a 6% reduction from 2010 [12]. In addition, RAC and Transport Canada will identify and support practices and technologies that reduce emissions to support the MOU.

2.4.1.2 Canadian Locomotive Emission Monitoring Program

The LEM Program publishes data annually in accordance with MOU. This annual document summarises CAC and GHG emissions produced by Canadian in-service locomotives operated on Canadian rail lines. In addition, the report contains information on fuel consumption, traffic, and inventory. Figure 5 below shows the emission intensity for CO_{2eq}, CO₂, CH₄, and N₂O in the years between 1990 and 2011, inclusively. The LEM data is especially useful to evaluate rail labour productivity for companies in the transport business; parameters such as RTK and gross tonne kilometers (GTK) measure productivity. For example: Class I GTK and RTK traffic are 644.75 billion and 337.0 billion respectively; this is equivalent to 93.5% and 93.9% of total GTK and RTK, in Canada [13].

³CO_{2eq}: the constituents of which for diesel combustion cycle are Carbon Dioxide, Methane, and Nitrous Oxide. These are considered the gases with global warming potential converted to CO₂ eq [69].

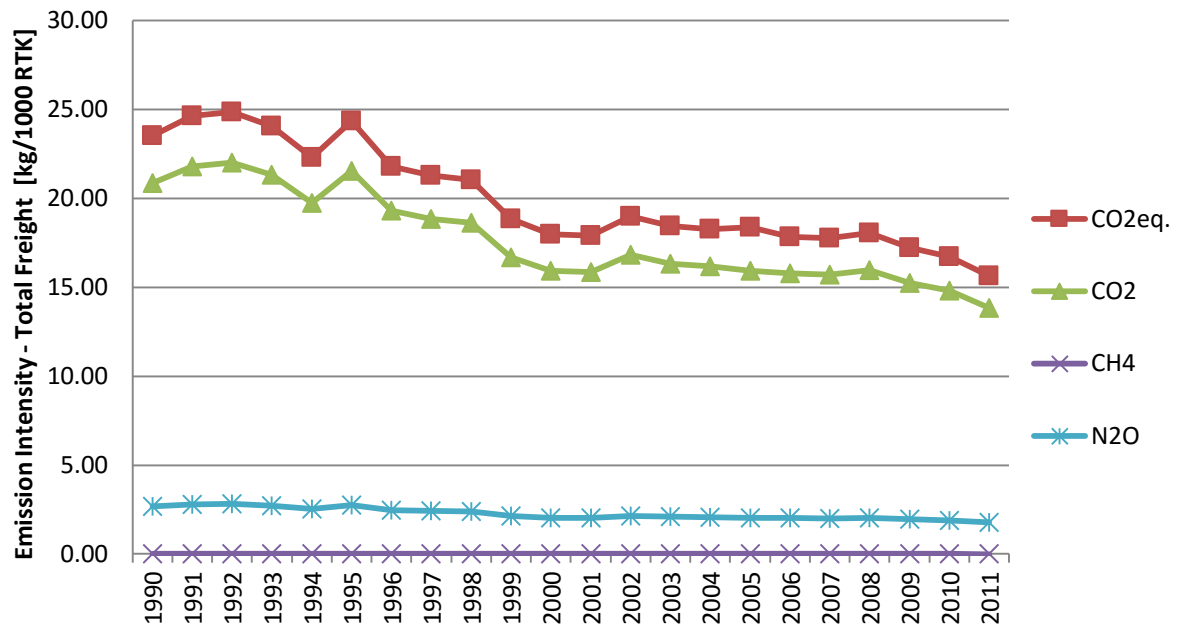


Figure 5: Plotted values of emission intensity, from the LEM reports, from 1990 to 2011 [14].

2.4.2 Emission Assessment

Freight trains are highly complex and interlinked railroad systems. It is very difficult to accurately estimate the energy consumption, direct fuel savings, or carbon emission savings caused by reduction in the structural weight of freight cars. The currently available literature does not quantify the CO₂ reduction potential achieved by mass reduction. Any saving estimate requires a complete understanding of the interactions between operators. In general, the energy consumption of freight trains is affected by, for example, the train length/total-weight, route characteristics, driving behaviour, and traction type [15]. The only reported correlation between energy savings and weight reduction was listed in [15], where they identified for exemplification a value of 5% energy saving for a 10% weight reduction which is independent of the total train weight; this corresponds to 6.1 tonne life-time CO₂ savings, assuming 180 kJ/gross t-km specific final energy consumption.

Weight reduction in freight cars has higher indirect energy saving - more than four times that of direct energy savings because freight cars are weight limited cargo [15]. A weight reduction in a weight-limited cargo can be used for an increased payload. Since both the mileage performance and the specific energy are constant in this case, the transport performance or load factor⁴ will be higher. A survey on American trains concluded that 100 kg weight reduction of a base-line train⁵ can have 386 GJ higher life-time transport performance [kg-km] [15]. Having higher transport performance is referred to as indirect energy saving.

2.5 Design Trends in Freight Cars

Companies like Standard Steel Company used to build all-steel hopper cars in the early 1900s. Then in 1934, Baltimore & Ohio built the first aluminium hopper car in conjunction with Alcoa (Aluminium Company of America) to reduce the structural weight of their railcars and increase freight capacity. This marked the first change in hopper car designs where the body and the underframe were entirely made from aluminium. The car was 6350 kg lighter than the same version of an all-steel car. However, the car never reached mass production [16]. In the period 1953-1960, companies in Canada, United States, France, and England produced over 700 welded covered hopper cars [17]. Car manufacturer soon reached the limit of reduction in weight and costs.

Composite materials were discovered around that time; fibreglass was not discovered until 1935 by Owens Corning [18]. This material had a high strength-to-

⁴ Load factor is payload of the railcar as a proportion of the total gross mass [16].

⁵ Base-line train has 100 railcars and 3,000 t, net weight of load and a fuel consumption of 178 kJ/gross kg-km [14].

weight ratio which attracted many global industries. Glasshopper Inc. was established in 1978 to make the first reinforced plastic covered hopper car, see Figure 6.



Figure 6: Glasshopper, the first reinforced plastic covered hopper (overall length: 16.15 m) [19].

The Glasshopper was constructed by a combination of steel and composite materials. 50% of the total empty weight of the railcar was made from fibre reinforced polymers, excluding the trucks [19]. The Glasshopper weighed 24,041 kg, 4,536 kg lighter than all-steel counterpart, and had a total capacity of 141 m³. There were only two Glasshopper cars built: the first was scrapped due to severe corrosion of its steel components, and the second was retired after 5 years in service [19].

More recently in 2014, the ApATeCh Group and its partners produced a composite hopper car body as shown in Figure 7. The body is a self-supported monocoque shell made from fibreglass and polyester mounted on a metal underframe [20]. This reduced the empty weight by 35-40% of a similar all-metal hopper. The

company announced they signed an agreement to produce and deliver 1,500 composite hopper cars [21] to an undisclosed country.



Figure 7: Composite hopper car body produced by vacuum infusion (overall length: 13.7 m) [21].

The main difference between Glasshopper and ApATech's cars was the fabrication process. Both were built using fibreglass: the former was produced by filament winding, and the later by vacuum infusion [19] [21].

Great Dane Trailers, commissioned by Walmart, built the first carbon-fibre truck trailer, see Figure 8. The roof and sidewalls are made out of one-piece of 16.15 meter carbon fibre panels and one-piece reinforced fibreglass floor panel, which reduced the overall weight of the trailer by 1,814 kg when compared to conventional designs [22].



Figure 8: Walmart's concept truck. Picture depicting the trailer (overall length: 16.15 m) [22].

Chapter 3

Design Requirements & General Hopper Design

Hopper freight cars must meet the standards and requirements set by Transport Canada, which in turn adheres to the Association of American Railroads standards to simplify safe cross-border movement of railcars. This chapter summarises the major AAR design requirements relevant to hopper railcar designs. In addition, the reader will be introduced to typical hopper railcar designs and components to insure familiarity.

3.1 Design of Typical Hopper Cars

In general, hopper cars are used to transfer dry bulk commodities, see Figure 9. These cars use the so-called gravity gates to discharge the lading. There are mainly two types of hopper railcars: covered and open. Their selection is dependent on the need to protect the transferred goods from exposure to the weather elements.



Figure 9: Common goods transported via a Hopper freight car [23].

A list of all available data on hopper car specifications from all North American railcar manufacturers can be found in Appendix B. From this summary, the average empty weight of a covered hopper car produced in North America is 19.5% of the total gross weight. In addition, two sidewall configurations were noticed from these data: cylindrical and flat as seen below.



Figure 10: Covered hopper railcar with cylindrical sidewalls [24].



Figure 11: Covered hopper railcar with flat sidewalls [25].

Both sidewall configurations are attached to two side sills: top and bottom. The flat sidewalls have externally mounted stiffeners/stakes. These structural components are labeled on Figure 12 and defined below [26]:

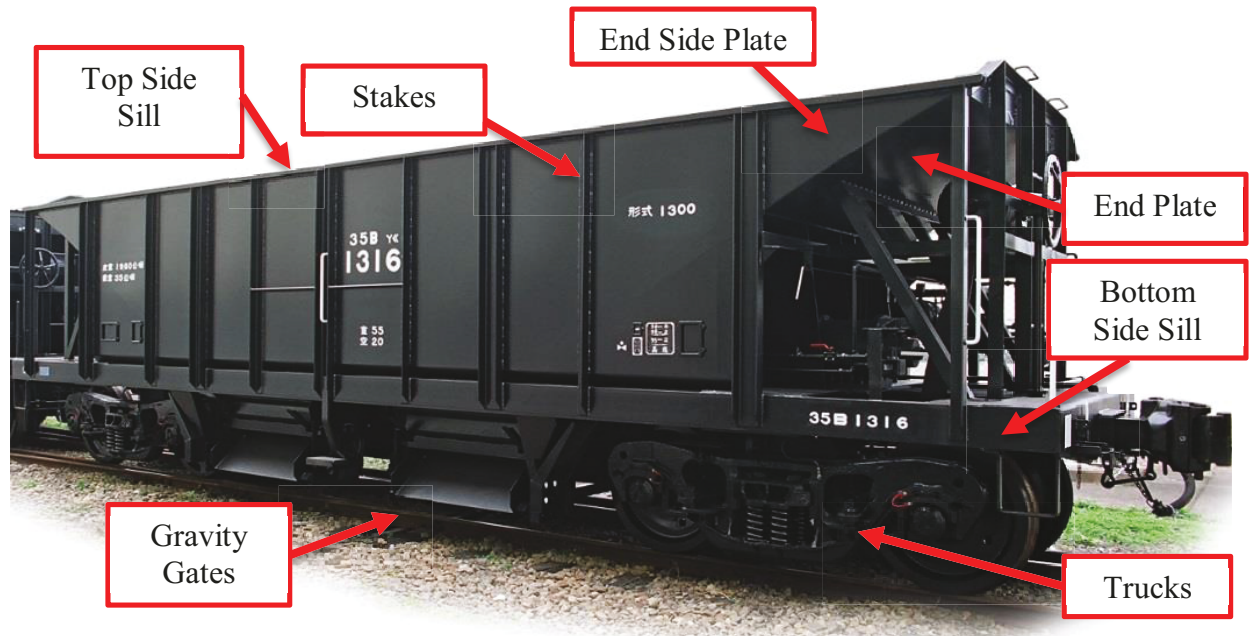


Figure 12: Hopper car with its main components labelled [27].

- Truck (bogie): railroad car wheel assembly usually having two or more axels. They rotate freely beneath railroad cars in order to allow them to navigate turns.
- Stakes: The side stiffening pieces used to hold the load in place on steel hopper and gondola cars.
- Sill: the main longitudinal timbers that are connected transversely by the end sills, body bolsters, and cross ties. Sills are divided into side sills, intermediate sills, and centre sills.
- Side sills: the outside longitudinal members of the underframe. In some designs of steel cars, the entire side of the car is designed as a deep plate girder to carry most of the load to the bolster

- Centre sills: The central main longitudinal members of the underframe of a car that are usually close together in the centre of the car. They form as it were the backbone of the underframe and transmit most of the buffing shocks from end to end of the car.

3.2 Design requirements

The AAR Manual of Standards and Recommended Practices (MSRP) identifies the design loads and forces acting on freight car structures, allowable stress, general details such as welds and connections, and more. These standards can be used in the design, analysis, and construction of freight cars. It is important to reiterate that the objective of this thesis is to investigate the replacement of current metals with fibre-reinforced polymer (FRP) in the sidewall structures of hopper railcars.

The manual covers in great detail all types of subjective loading experienced by all freight cars, and their respective components. Therefore, it was best to summarize the relevant standards.

In addition to the general requirements derived from AAR MSRP, there are factors unique to FRP and fabrication processes used for a given application not covered in the standards. Therefore, *Advisory Circular 20-107B on Composite Aircraft Structures*, published by the U.S. Department of Transportation Federal Aviation Administration (FAA) [28], was used as guidance information on design, manufacturing, and maintenance for new composite railcar structures given the similar design requirements between advanced aircraft structures and new railcars. The following requirements from AAR MSRP standards and 20-107B relevant to the present research are summarized below:

Table 3: List of critical design requirements.

No.	Requirements
1	Sidewalls must withstand the lateral pressure of granular, lump, or pulverized bulk material calculated using the Rankine formula shown in equation (1)
2	Centrifugal and/or lateral forces due to acceleration (0.3 G)
3	Load factor and allowable design stresses for lateral forces shall be 1.5 and 80% of ultimate
4	Demonstrate reproducibility through fabrication trials and tests
5	Withstand critical environmental exposures, such as temperature and humidity
6	Protection of structures against weathering, abrasion, ultraviolet radiation and chemical environment

$$P = \frac{1}{2} W h^2 \frac{1 - \sin \phi}{1 + \sin \phi} \quad (1)$$

[29]

Where P : Lateral force [N/m of length]

W : Specific weight of lading [N/m³]

h : Depth of lading [m]

ϕ : Static angle of repose [25°]

Chapter 4

Material and Fabrication Process Selection

The first step to improving the design of current sidewall structures was to gather information on the material used in current hopper railcars. This chapter presents the experimental tests performed on test coupons obtained from a decommissioned hopper railcar. These tests aimed to identify the mechanical properties of the steel, and hence the metal type used to establish a baseline for comparison. Different FRP materials were explored to determine a suitable substitute material to the identified metal that meet the requirements set by AAR. Next, a fabrication process was selected based on the cost and repeatability of manufacturing the sidewall panels. Finally, fabrication trials were conducted to identify specific challenges with the chosen fabrication process.

4.1 Typical Hopper Railcar

Current North American railcar manufacturers are using primarily steel in the construction of the sidewall structures of their various hopper railcar models as seen from Appendix B. However, there were no data published on the type of steel used nor the internal design configuration of any existent hopper railcar. Understanding the current design of hopper railcars, especially the sidewall construction, was deemed critical to aid in any design optimization and/or enhancement. Knowing the mechanical properties, for example, of the steel used in the sidewall structure was required so that a suitable FRP material candidate could be selected.

A piece, shown in Figure 13, was cut from a decommissioned steel hopper railcar at the request of the author to help determine the type and mechanical properties

of the steel used in the sidewalls of in-service hopper railcars. No information was available on the specifications of the steel piece from the manufacturer.

Tensile and hardness tests were conducted on multiple coupons from the steel panel to determine the Young's Modulus, yield strength, ultimate tensile strength, and percent elongation. In addition, metallographic tests were performed to determine the microstructural properties of the steel. The results and findings from these tests are summarized in the following sections.



Figure 13: A 1 m X 0.72 m steel plate cut from the sidewall of a decommissioned hopper car.

Figure 14 shows the location of the test specimens on the steel plate. It was important for all specimens to be located at a distance away from the edges to avoid the region affected by the heat produced by the plasma cutter. In addition, the specimens were machined using waterjet cutting to reduce the effect of stresses on the mechanical or physical properties of the specimens. This was especially important for the

specimens used in the optical microscopy tests, as the through-thickness microstructure of the steel was investigated.

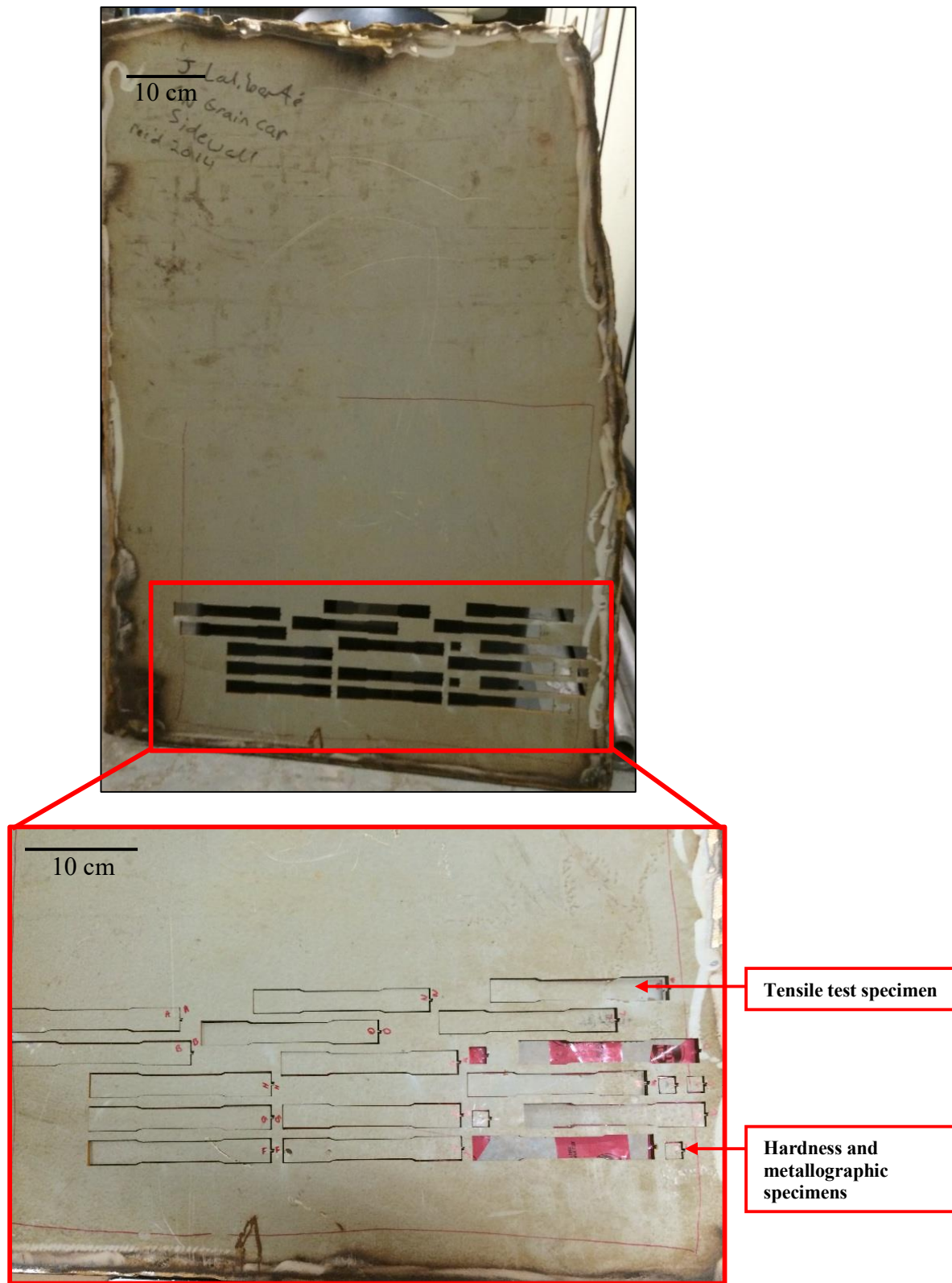


Figure 14: Location and orientation of the test specimens used in for the tensile, hardness, and metallography tests.

4.1.1 Hardness Testing of Steel Hopper Railcar Specimens

Hardness testing measures the material's resistance to localized plastic deformation using an indenter [30]. The most common form of hardness testing is called Rockwell hardness test [30, p. 191]. The Rockwell hardness test (HR) uses several different scales in combination with different indenters and loads to measure the hardness number. The hardness number was measured by determining the difference in depth of penetration caused by the application of an initial minor load of 10 kg followed by a larger major load of 60, 100, or 150 kg [30]. Two types of indenters are available for researchers at the Carleton University's Mechanical and Aerospace Engineering Department: diamond cone and 1/16th inch diameter steel ball. The diamond indenter, shown in Figure 15, requires the use of scale C and 150 kg as a major load (abbreviated by HRC). The 1/16th inch steel ball, shown in Figure 16, uses scale B and 100 kg as a major load (abbreviated by HRB). The diamond indenter and scale C (HRC) are generally used for materials with high tensile strengths, such as American Iron and Steel Institute (AISI) 3140 and AISI 1045 water-quenched. The steel ball indenter and scale B (HRB) is generally used for materials with low tensile strengths such as low-carbon steel AISI 1020 and AISI 1018 [30].



Figure 15: A Rockwell device with a diamond indenter.



Figure 16: Rockwell device with a 1/16th in steel ball.

The hardness tests were conducted on five specimens in accordance with the guidelines and procedures detailed in the American Society for Testing and Materials (ASTM) E18 (Standard Test Methods for Rockwell Hardness of Metallic Materials), [31]. After four trials, the hardness number obtained using the diamond indenter, i.e. HRC, were below zero on the scale. This was a clear indication that the material tested has low tensile strength. Therefore, HRB was used solely throughout the hardness tests. Table 4 below lists the hardness numbers obtained from the five different specimens.

Table 4: Hardness numbers obtained using 1/16th inch diameter steel ball, scale B, and 100kg major load.

Sample No	Measured hardness Number					Average Hardness Number	Standard Deviation
1	86	84	85	86	86	85	1
2	85	86	84	84	86	85	1
3	88	84	85	87	86	86	2
4	86	85	85	86	85	85	1
5	85	86	82	86	86	85	2

The hardness numbers determined from the HRB test were converted to Brinell hardness (HB) numbers using the conversion tables found in ASTM E140-12b (Standard Hardness Conversion Tables for Metals Relationship Among Brinell Hardness, Vickers Hardness, Rockwell Hardness, Superficial Hardness, Knoop Hardness, and Scleroscope Hardness), [32]. Table 5 summarizes the values of HRB and HB for the five steel specimens. In conclusion, the average Brinell hardness number for the unknown steel was found to be 165.8 ± 4.6 .

Table 5: conversion of the average HRB values to tensile strength of each sample in Table 4.

Sample No.	Average HRB	Converted using [32]	HB
1	85 ± 1	→	165 ± 3.5
2	85 ± 1		165 ± 3.5
3	86 ± 2		169 ± 5.5
4	85 ± 1		165 ± 3.5
5	85 ± 2		165 ± 5.2

4.1.2 Uniaxial Tensile Testing of Steel Hopper Railcar Specimens

The objective of the tensile tests was to provide information on the ductility and strength of the unknown steel under uniaxial tensile stresses. These properties include yield strength, tensile strength, elongation, and Poisson ratio.

The uniaxial tensile tests were conducted in accordance with the guidelines and procedures of the ASTM E8 (Standard Test Methods for Tension Testing of Metallic Materials), found in [33]. All the tensile specimens, as seen in Figure 14, were waterjet-cut to meet the tolerances specified in the ASTM E8 standard, shown in Figure 17. In total, four specimens were tensile tested. For each specimen, the initial gauge length (l_o) and the cross-sectional area (A_o) of the reduced section were measured three times before installation. Each sample was fitted with two strain gauges at right angles to each other to measure the longitudinal and transverse strain, and an extensometer to measure the strain in the axial directions for each specimen, as seen in Figure 18 and Figure 19.

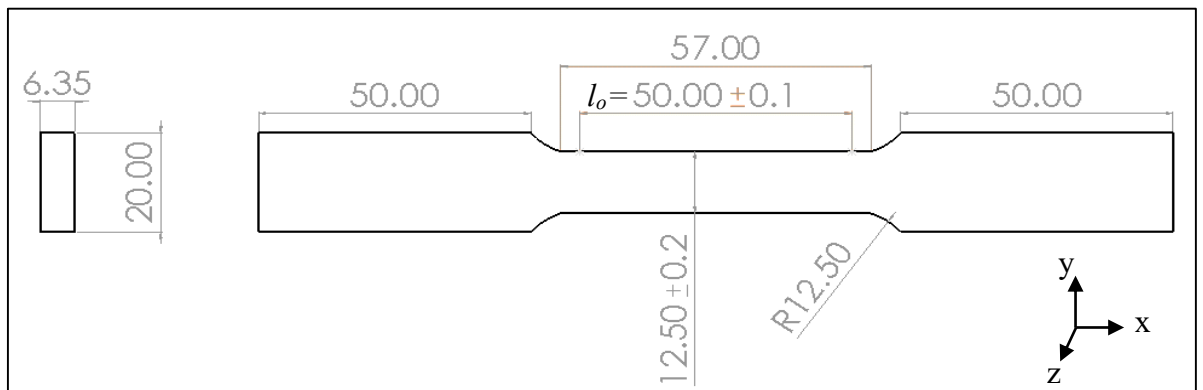


Figure 17: Test specimen geometry obtained from ASTM E8, all units are in millimetre.

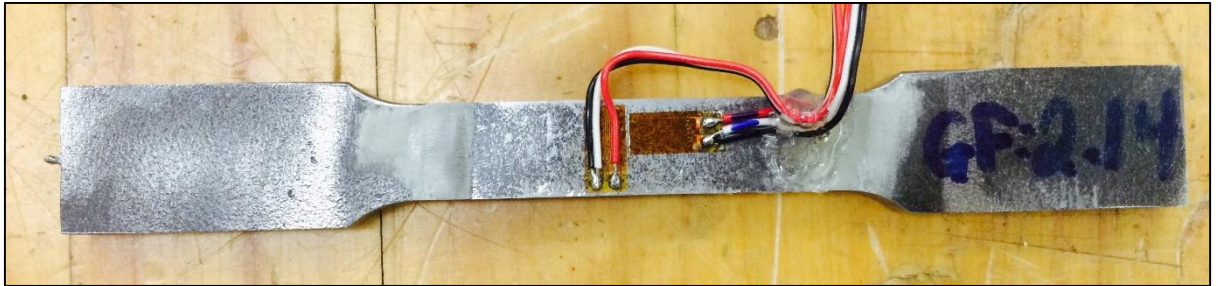


Figure 18: Test specimen showing the location of the two perpendicular strain gauges.

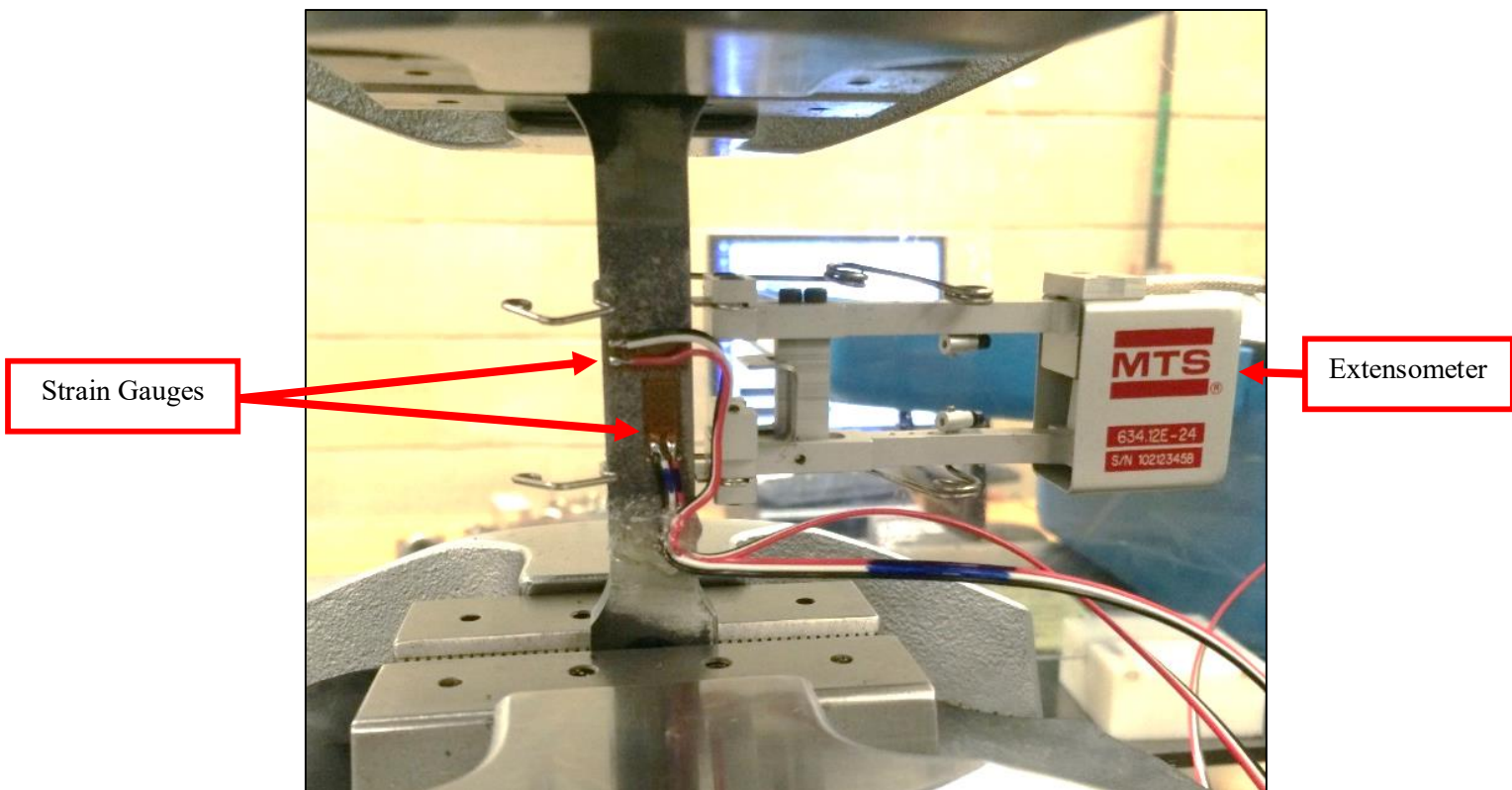


Figure 19: Final setup with the strain gauges and extensometer.

The tensile tests were carried out by applying a longitudinal load in crosshead speed control at a rate of 0.75 mm/min using the MTS 810 Material Test System servo-hydraulic test frame shown in Figure 20. The applied axial load and axial displacement were recorded during the test using a combination of MTS FlexTest Controller Software. The axial extensometer (Model 634.12E-24, serial number 102123458)

recorded the axial strain, while the Micro-Measurements P3 Strain Indicator and Recorder, shown in Figure 21, recorded the longitudinal and transverse strains.



Figure 20: MTS 810 Test System, 100 kN, used to conduct the tensile tests.

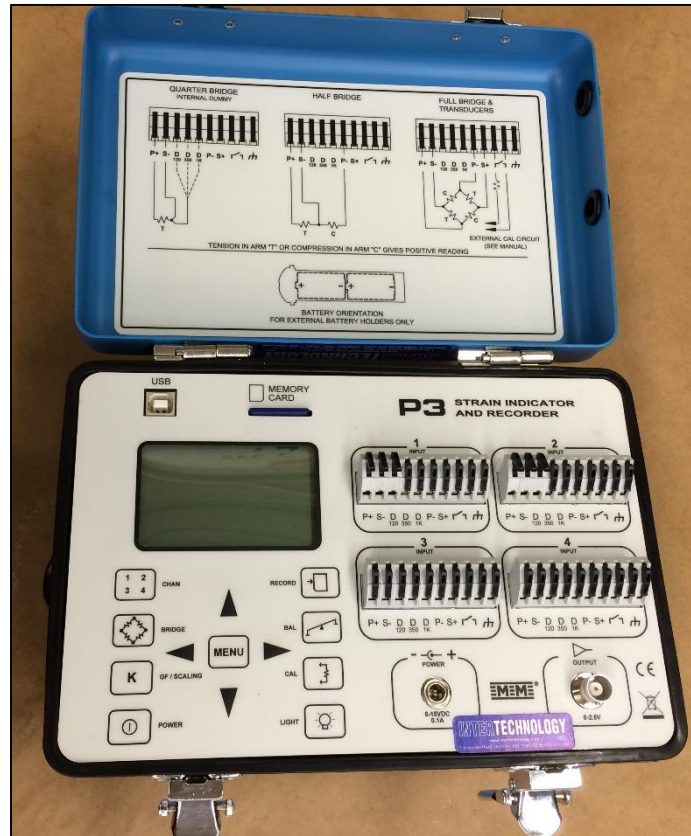


Figure 21: P3 Strain Indicator and Recorder used to collect readings from the strain gauges.

The data obtained from uniaxial tensile tests was used to determine the mechanical properties of the unknown steel using the following equations, obtained from [30]:

- **Engineering Stress (σ) [MPa]**

$$\sigma = F/A_o \quad (2)$$

Where F is the instantaneous axial load [N]

A_o is the original cross-sectional area before any load is applied [mm²]

- **Engineering Strain (ϵ) [mm/mm]**

$$\epsilon = \Delta l/l_o \quad (3)$$

where l_o is the original gauge length [mm]

Δl is change in length at some instant [mm]

- **Poisson's Ratio ν**

$$\nu = -\epsilon_y / \epsilon_x \quad (4)$$

Where ϵ_x and ϵ_y are the strain result in the x- and y-directions, respectively.

- **Modulus of Elasticity or Young's Modulus, (E) [GPa]**

$$\sigma = E * \epsilon \quad (5)$$

Note: Young's modulus can be obtained by calculating the slope from the linear elastic region in the stress-strain diagram.

- **Yield Strength (σ_y)**

The yield strength is the stress level at which plastic deformation begins. The tensile stress-strain behaviour of this steel exhibited a similar elastic-plastic transition to that shown in Figure 22. The method to determining the yield strength of such behaviour is by taking the average stress value at which continued deformation fluctuates slightly about some constant stress value, called the lower yield point [30].

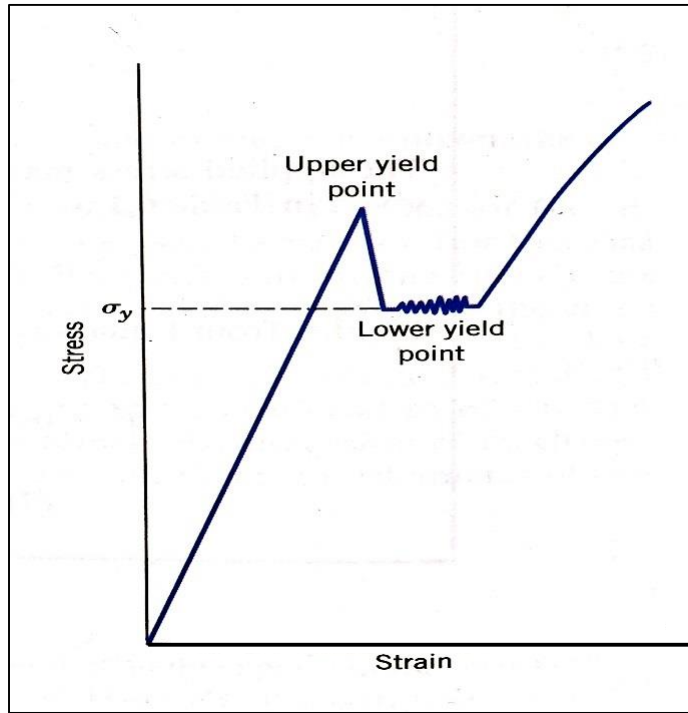


Figure 22: schematic representation of typical stress-strain behaviour found for some steels [30].

Figure 23 and Figure 24 illustrate the method of obtaining tensile strength, yield strength and modulus of elasticity for sample #1. Table 6 provides a summary of these mechanical properties for all four samples.

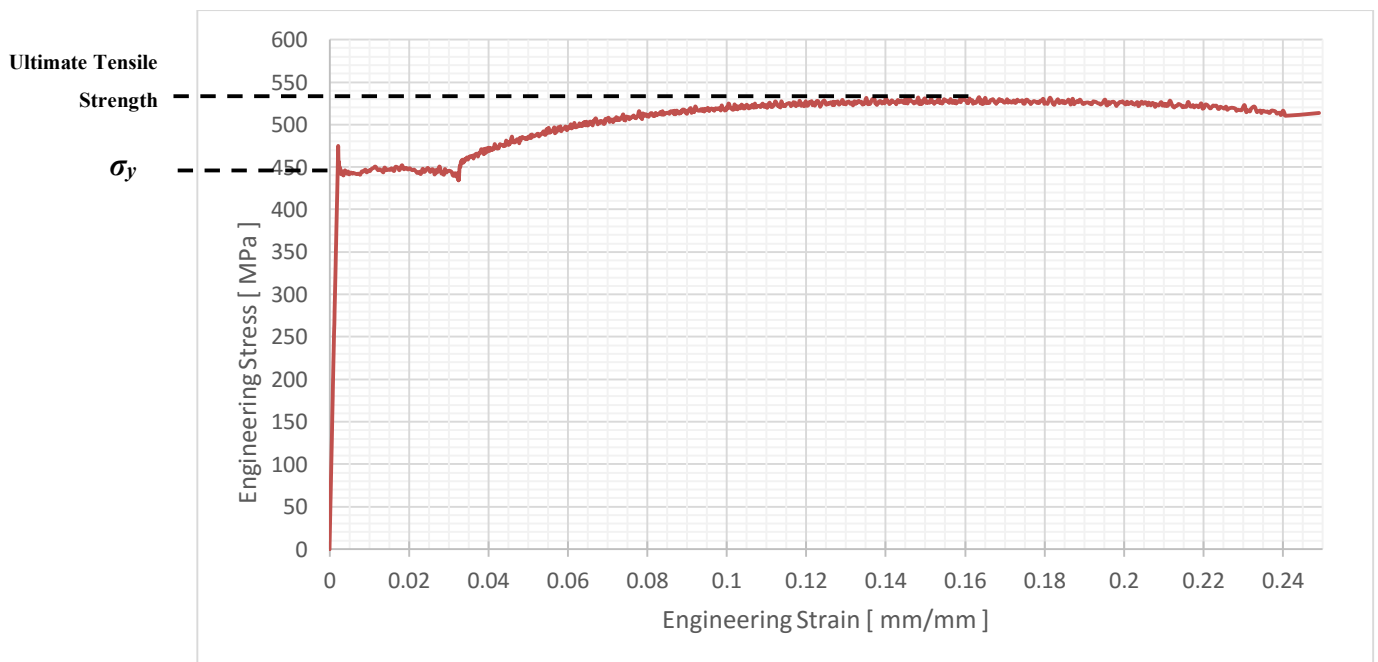


Figure 23: Plotted values for the engineering stress-strain curve of the unknown steel for sample #1.

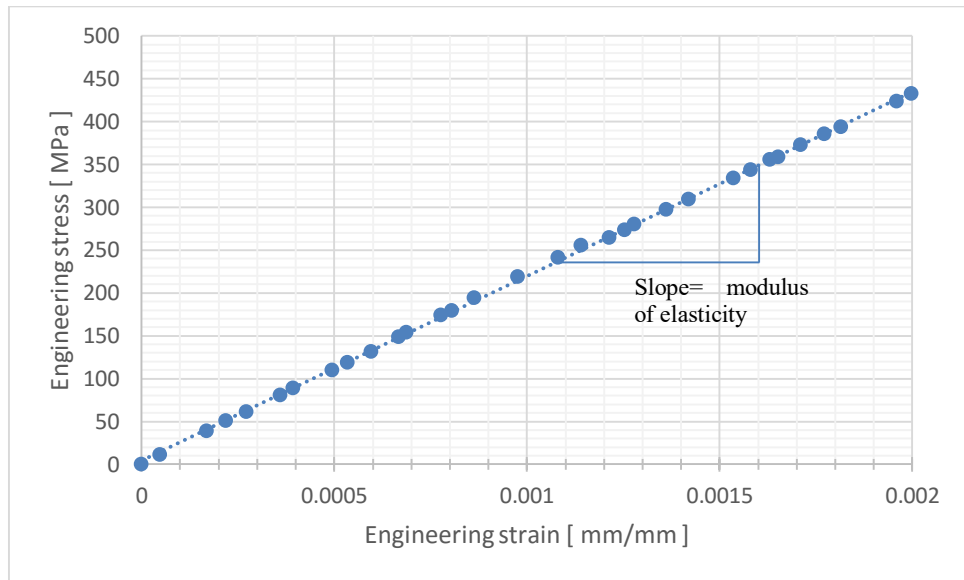


Figure 24: The linear (elastic region) from Figure 23.

Table 6: Summary of the key mechanical properties obtain from the uniaxial tensile testing.

	Sample #1	Sample #2	Sample #3	Sample #4	Average
Young's Modulus [GPa]	207	209	210	210	209 ± 1.4
Poisson's Ratio	0.27	0.27	0.28	0.28	0.28 ± 0.01
Tensile Strength [Mpa]	543	525	538	543	537 ± 8.5
Yield Point [Mpa]	449	437	448	457	448 ± 8.2
Percent Elongation	28	30	29	30	29 ± 1.0

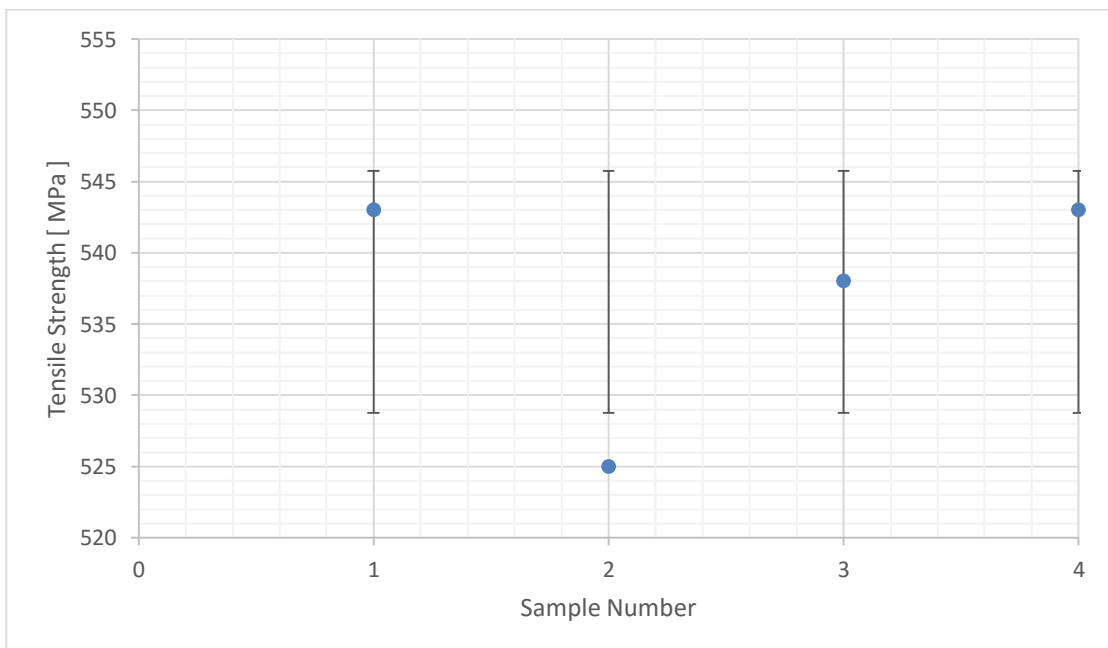


Figure 25: Data point corresponding to tensile strength values from Table 6; error bars indicate the degree of scatter corresponding to the average tensile strength value plus and minus the standard deviation.

4.1.3 Optical Microscopy

This type of testing was necessary to examine and characterize the microstructure, grain size and shape, of the unknown steel. In addition, the microscopic examination was important to determine whether the material had gone through any clear form of heat-treatment or strain hardening.

Three specimens were prepared and examined in accordance with the ASTM E3-01 (Standard Practice for Preparation of Metallographic Specimens), found in [34]. In combination, the three samples revealed the grain structure of the unknown steel plate from three different angles: the outside surface and two perpendicular through-thickness views (in the transverse and longitudinal directions). Sample 1, shown in Figure 26 (a), was compression mounted on the side, as shown in (d) to examine the through-thickness grain structure in the transverse direction of the plate. Sample 2, (b), was compression mounted on the side, as shown in (e), to examine the through-thickness grain structure in the longitudinal direction of the plate. Sample 3, (c), was mounted on the top surface, as shown in (f), to examine the surface grain structure of the plate.

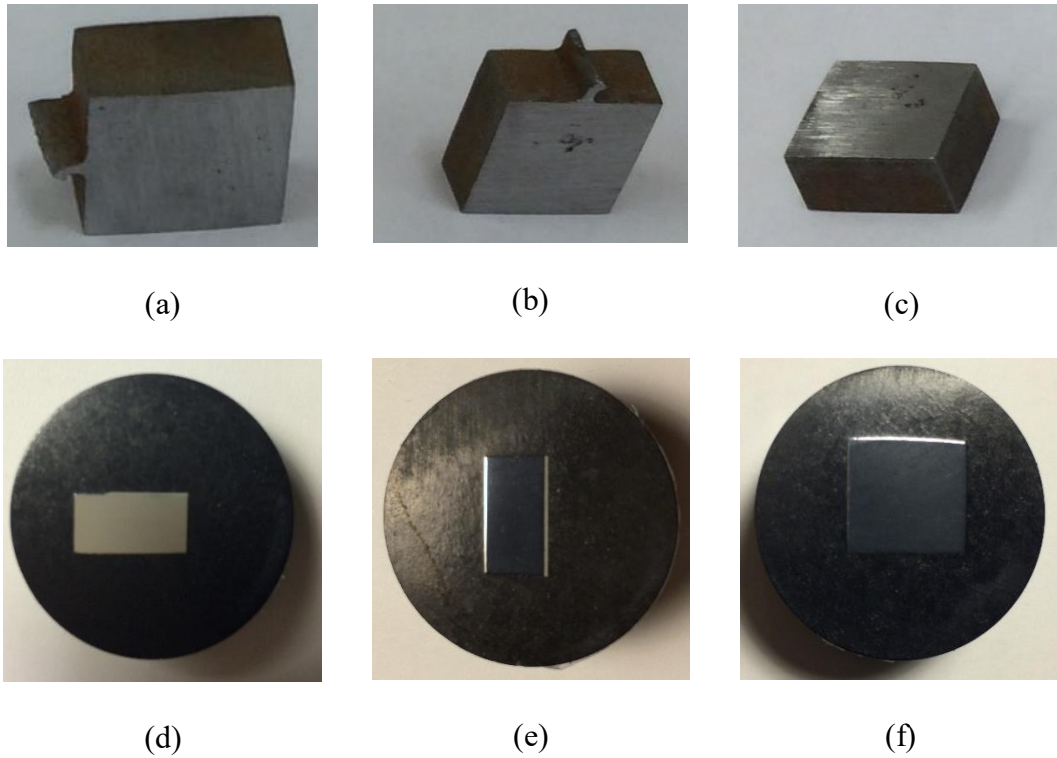


Figure 26: The initial and final stage of sample preparation for sample 1 (a,d), sample 2 (b,e), and sample 3 (c,f)

The produced microstructure images can be seen in Figure 28. The grain shape and size clearly indicate that the unknown steel did not undergo any strain hardening or quenching. This was concluded by comparing the grain structure of the unknown steel with grain structure of cold worked and quenched AISI 1020 and AISI 1045. In general, the dislocations density in a strain hardened or cold worked steel are large. This can be seen in the microstructural images as elongated grains, as shown in Figure 27.

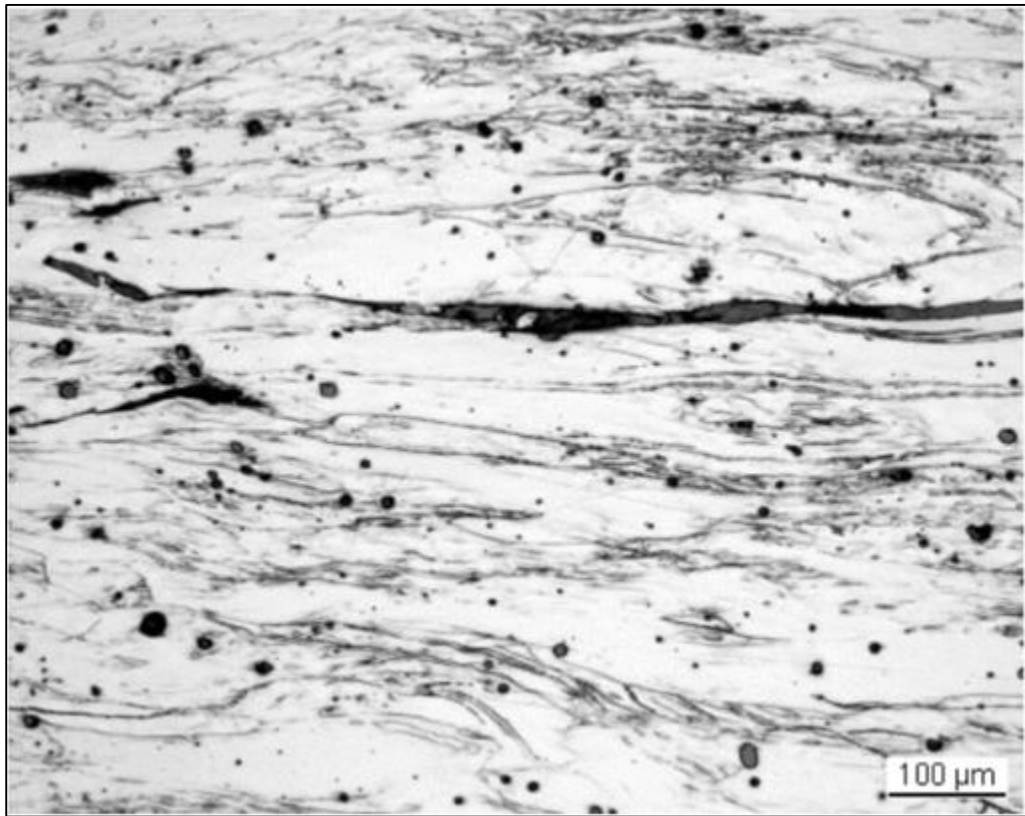


Figure 27: Microstructure graph of a cold worked metal sample with horizontally elongated grains [35].

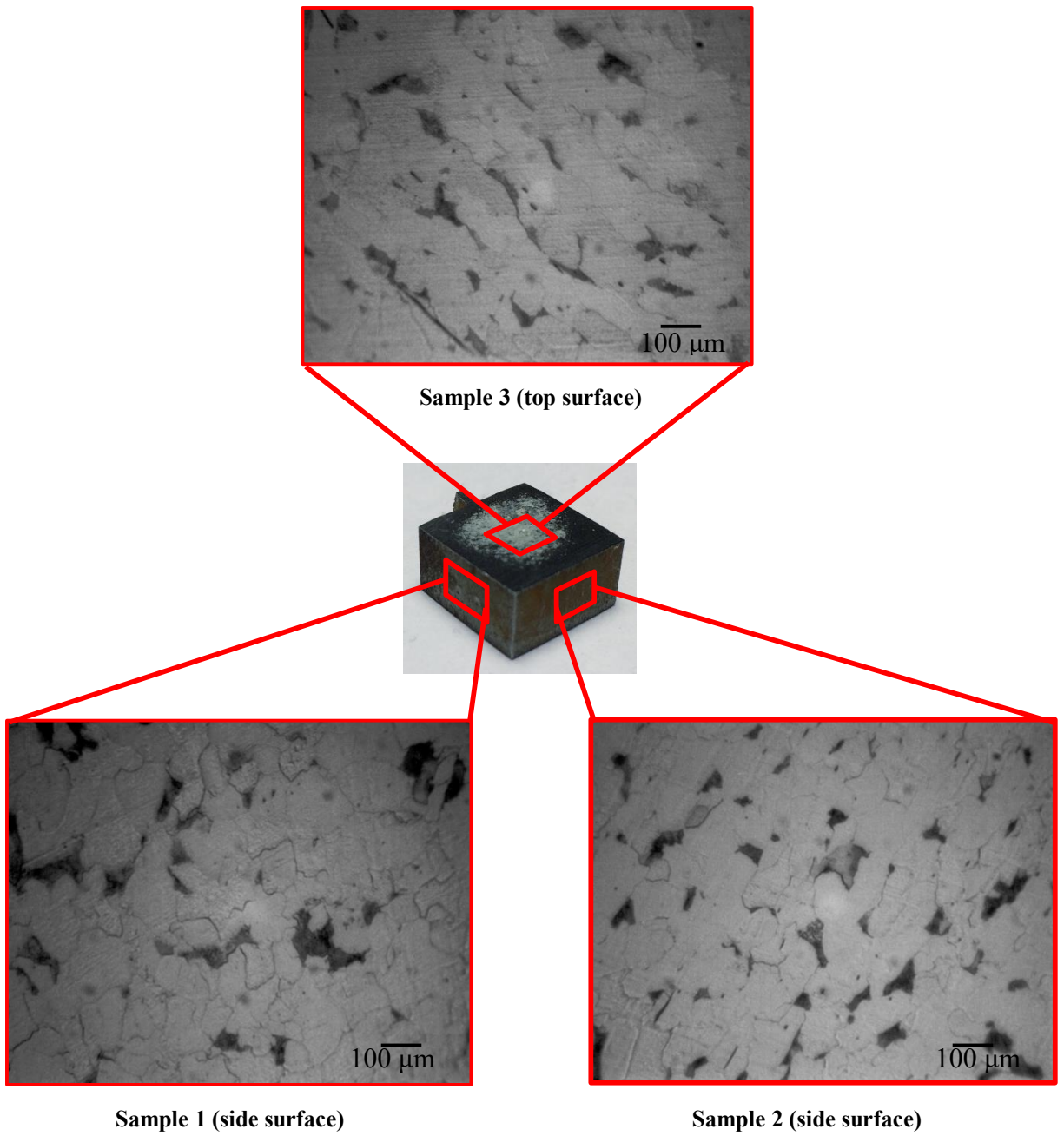


Figure 28: The microstructure images of each face from the three samples.

4.1.4 Results and Discussion

Table 7: Summary of the key mechanical properties obtained from hardness and tensile testing.

Tensile strength [MPa]	537 ± 8
Yield strength [MPa]	448 ± 8
Modulus of elasticity [GPa]	209 ± 1
Poisson's ratio	2.8
Percent elongation	29
Brinell Hardness	165.8 ± 4.6

Hardness and tensile tests produced sufficient information about the mechanical properties of the unknown steel. These values are summarised in Table 7. The microstructural images obtained from the three samples showed that the unknown steel was indeed a low-carbon steel. This was deduced by comparing the microstructure images of the unknown steel to those from AISI 1018, 1020, and 1045, shown in Figure 29. By comparing the hardness numbers and grain size and shapes of AISI 1018, 1020, and 1045 to the unknown steel, it was concluded that the unknown steel was a closer match to AISI 1020.

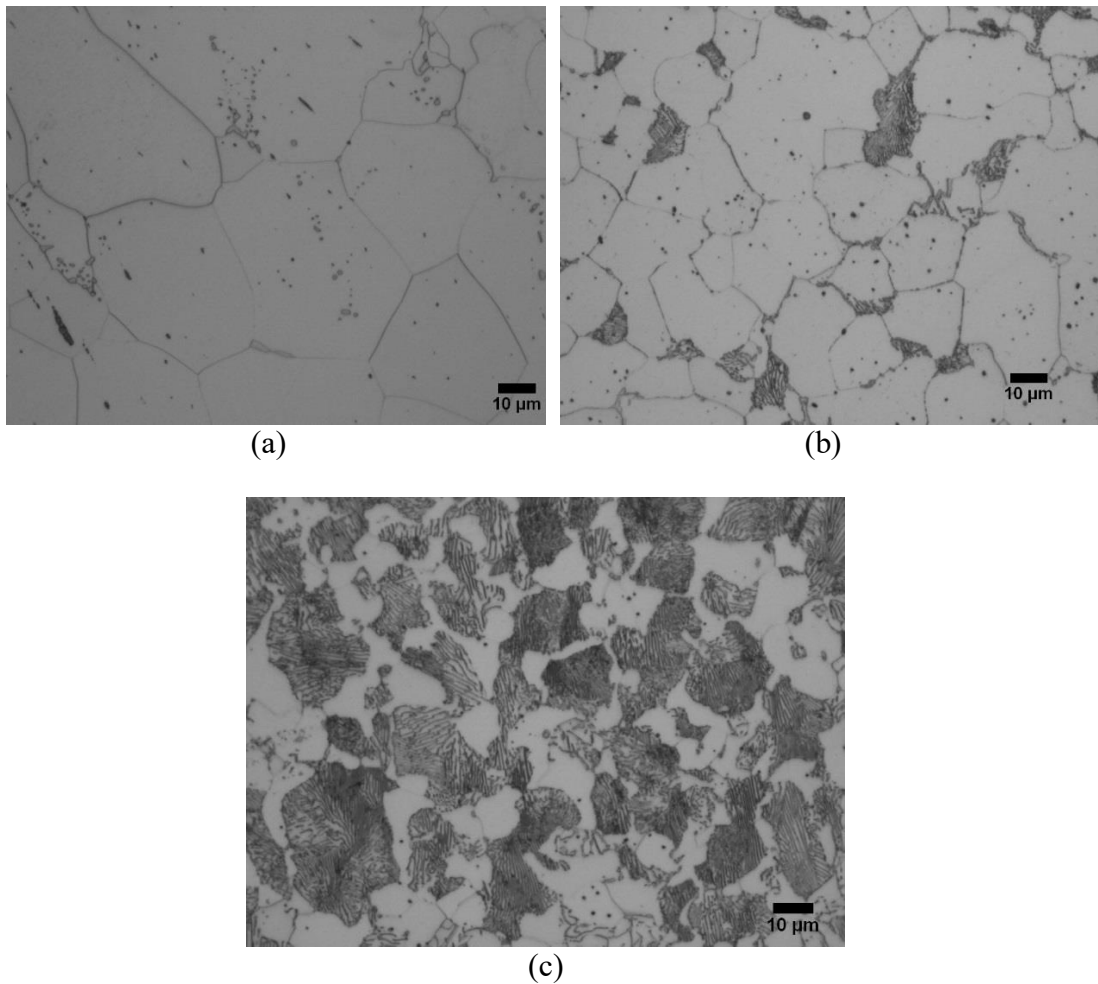


Figure 29: Microstructure images of a) AISI 1018 b) AISI 1020 and c) AISI 1045 [36].

4.2 Fibre Reinforced Polymer Options

The work described in the previous section focused on determining the mechanical properties of the steel used in sidewalls of hopper railcars to establish a baseline for comparison and weight reduction estimate. The next section will present the selection of the fibres and matrix materials to replace steel. The assessment of the resulting fibre reinforced polymer material was based on the mechanical properties, manufacturability, and cost.

The fibre selection focused on the strength and cost of the materials. Therefore, only high-performance materials were examined. Table 8 summarizes the mechanical properties of common high-performance fibre reinforcements.

Table 8: Common fibre material properties [37] [30].

Fibre Material		Density[g/cm ³]	Modulus of Elasticity [GPa]	Ultimate Strain [%]	Strength [GPa]	Maximum Operating Temperature [°C]	Cost (\$US/kg) ⁶
Glass	E-glass	2.58	73	4.3	3.5	350	1.55-2.65
	S-glass	2.6	89	4.5	4.7		1.65-3.3
Carbon	Standard Modulus (PAN precursor)	1.78	230	2	3.8-4.2	>2000	40-80
	Intermediate Modulus (PAN precursor)	1.78	285	1.8	4.7-6.4		60-130
	High Modulus (PAN precursor)	1.81	400	0.6	2.5-4.5		220-275
	Ultrahigh modulus (pitch precursor)	2.12-2.19	520 - 940	0.3-0.7	2.6-3.6		1750-2650
Aramid	Kevlar 49	1.44	131	2.8	3.6-4.1	250	35-100

Both fibreglass and aramid provide excellent toughness at a cheaper price, when compared to carbon fibres [30]. Fibreglass is commonly used in various equipment subjected to a range of environmental elements, such as marine application, sporting goods and bridges [37] [38]. In addition, fibreglass provides high strength, high elongation, and corrosion resistance at a low cost [30]. On the other hand, aramid fibres are known for their impact strength. Kevlar, a commercial name for aramid/epoxy, is commonly used in military and personal protection applications [30]. Carbon fibre is considered to be the most expensive option of the three. When carbon fibre is in contact

⁶ Pricing information was collected in January 2007 [31]

with steel or aluminium alloys, an insulating layer of glass/epoxy or Kevlar/epoxy is used to prevent galvanic corrosion on the metallic side of the joint [37]. This will add additional costs to prepare and surface-treat the steel contact joints in the hopper railcar. For these reasons, fibreglass and aramid were only considered as viable fibre material options.

There are two forms of matrix materials, or resins: thermosetting and thermoplastic. Thermosets provide good fibre wetting, hence adequate to adhere to most types of fibres, and resistance to creep. Thermosets are also feasible for liquid-resin manufacturing and formable into complex shapes at relatively low processing temperatures [37]. However, thermosets are prone to absorb moisture, up to 3% of its weight in some cases, which can negatively affect the matrix-dominated properties in the FRP laminates [37]. This can be alleviated by adding a coating layer to protect the exposed surfaces from direct contact with moisture.

On the other hand, thermoplastics absorb little moisture and unlike thermosets have high strain to failure properties and high fracture toughness [37]. However, thermoplastics are not a suitable candidate in general because thermoplastics are prone to creep and not well suited to conventional liquid resin manufacturing techniques [37]. In addition, thermoplastics have high fabrication costs due to high temperature and pressure involvement in the production phase [37]. Therefore, thermosets are deemed more suitable for this application than thermoplastics.

The most commonly used and accessible thermosetting resins are epoxy and polyester. Epoxy provides the ability to be formulated for optimum properties and fracture toughness [37]. Furthermore, epoxy is safe to use due to low volatiles production. Most importantly, epoxy has high bond strength and adhesion to fibres compared to polyester. However, epoxy has relatively high cost compared with

polyester and is moisture sensitive. Polyester has low viscosity compared with epoxy and provides excellent environmental durability. In addition, polyester allows for ease of wet-out of the fibres [37]. Epoxy was deemed more suitable for this application because it provides the ability to be formulated for optimum properties.

4.3 Fabrication Processes

There are numerous composite fabrication methods that vary in cost and final part quality. The methods relevant to this research area are categorized into three groups: wet layup, liquid resin moulding (LRM), and laminating. Figure 30 provides a summary of the research of the advantages and disadvantages of each method, further details can be found in many books and papers including [37] [39] [40]. Wet layup has the lowest tooling cost and finished part quality among all three. However, it lacks automation for large scale production and requires a high level of human experience to produce good final parts. Therefore, this method will not be further discussed in this thesis.

On the other end of the spectrum, laminating using preimpregnated fabrics in an autoclave produces the highest quality parts that meet the stringent requirements of the aircraft industry. This, of course, comes at the highest cost among the three fabrication methods. The high cost of this process is associated with the complex autoclave system and specialized materials used to make the parts [41].

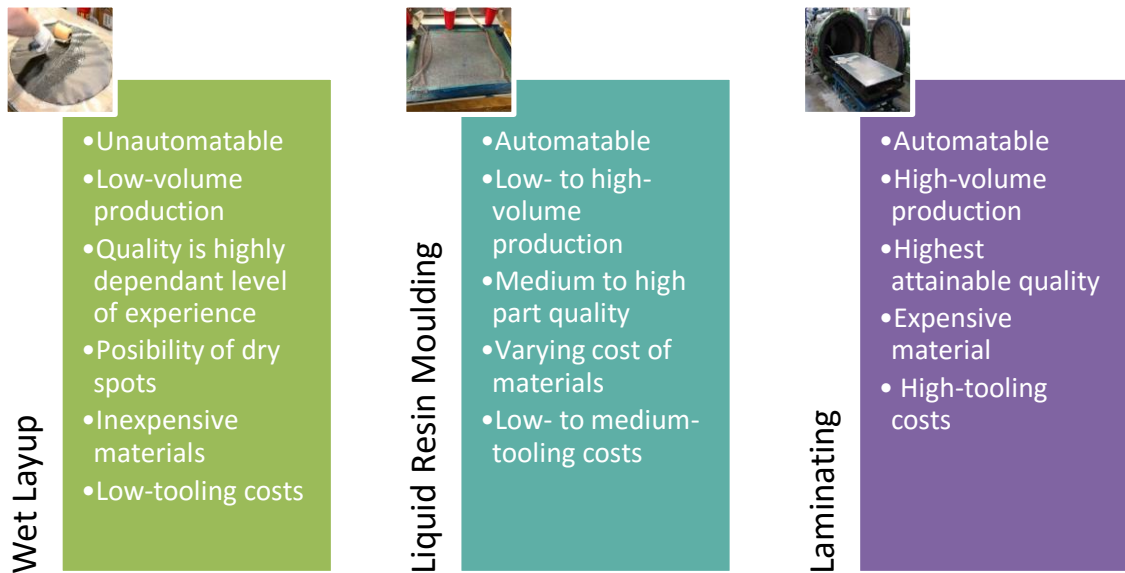


Figure 30: A short list of benefits and disadvantages of each of the relevant fabrication processes sorted ascendingly from left to right in terms of quality and cost.

Recent production trends showed that major aircraft manufacturers are constantly trying to reduce the costs associated with using autoclave fabrication process by improving current out of autoclave (OoA) manufacturing techniques for their FRP structural components, such as wings and fuselages. This had to be achieved without compromising the reliability and consistency of the processing method. In the recent years, autoclave processing was an indispensable equipment to manufacture high quality FRP aerospace structural components, for example the centre wing box for the Boeing 787 Dreamliner [42]. However, autoclaves are complex systems that are generally expensive to construct and operate, and the material used in that type of fabrication process, prepreg (composites consisting of dry fibres pre-impregnated with thermoset resin [37]), are the most expensive when compared to the other manufacturing techniques [37]. These factors were among the top driving factors for companies to invest in low-cost manufacturing (LCM) techniques. One technique that is currently gaining notable interest in the aircraft and wind turbine industries is resin

infusion (RI) and OoA curing [43], which as a process is part of LRM method. Figure 31 illustrates the differences between the two forming processes: autoclave and vacuum assisted resin transfer mould (VARTM), a type of LRM.

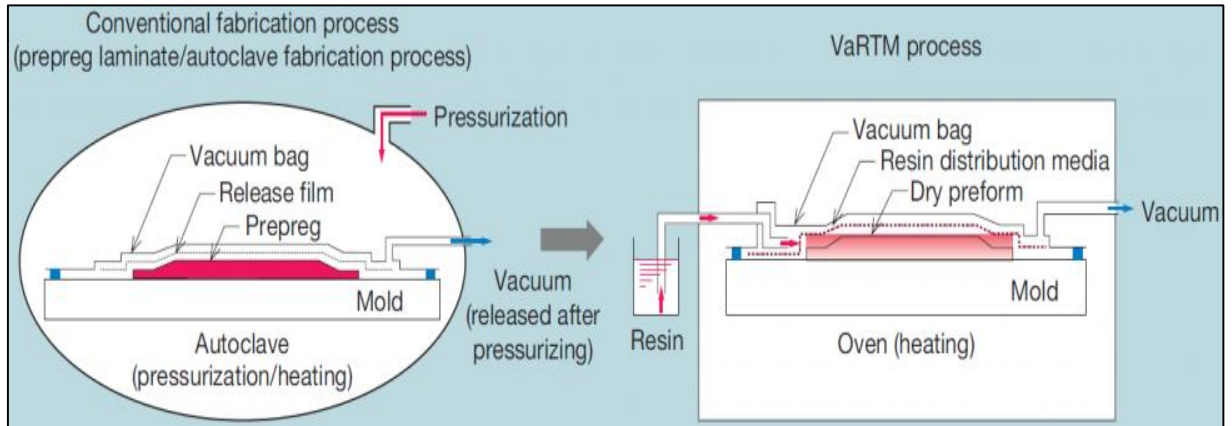


Figure 31: An illustrative comparison between Autoclave and VARTM manufacturing [44].

LRM processes are currently used in the manufacturing of the aft-pressure bulkhead of the A380 and the Boeing 787 [43]. Bombardier Aerospace is using Out of autoclave (OoA) resin infusion process in the production of the LearJet 85 wing box and the CSeries wings [45] [46]. NASA's Langley Research Center has developed an OoA wind turbine blade manufacturing method with quality close to those processed using autoclaves [47].

Findings from the Mitsubishi Regional Jet (MRJ) Program, found in [39] and [44], demonstrated the feasibility and ability to produce comparable mechanical properties to laminated structures using an advanced form of VARTM (A-VARTM) processes. Table 9 shows the result from strength tests using two full-scale vertical stabilizer box structures produced using the conventional autoclave process and an A-VARTM processes.

Cost reduction was another area at which VARTM has gained an edge over autoclaving. This was due to the removal of costs associated with autoclaves and

specialized prepreg materials. Findings from the MRJ Program indicated a noticeable reduction of production costs in the empennage structures using A-VARTM process as compared to autoclave fabrication, as shown in Figure 32. The production cost using A-VARTM process was estimated to be 20% more than the cost of the same part produced by aluminum.

Table 9: Comparison between the mechanical properties of Advanced Vacuum Assisted Resin Transfer Moulding and prepreg materials [44].

Test Items	Test Environment	Material Fabricated Using A-VARTM	Prepreg Material
0° Tensile Strength [MPa]	room temperature	2890	2960
0° Tensile Modulus [GPa]	room temperature	150	153
0° Compressive Strength [MPa]	room temperature	1570	1500
	82° C Wet	1250	1280
Open-hole Tension [MPa]	room temperature	519	500
	-59° C	473	448
Open-hole Compression [MPa]	room temperature	295	298
	82° C Wet	238	236

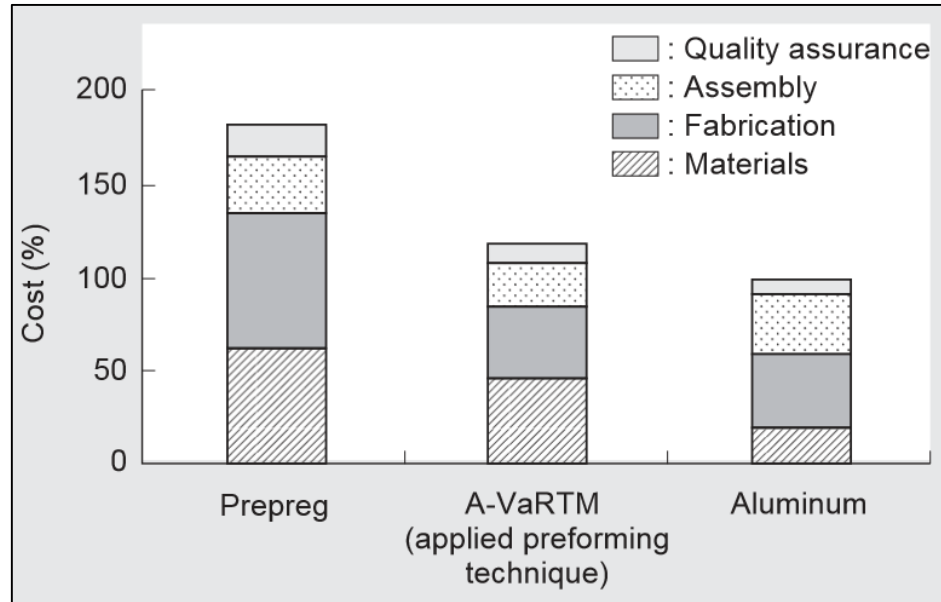


Figure 32: Cost comparison for MRJ empennage box structure [39].

Another very important finding that concerns large FRP structures was the coefficient of variation (CV) in fibre volume fraction, shown in equation (6) [44]. The CV value is a representation of the deviation of fibre volume fraction V_f , shown in equation (7) [44].

$$CV = \frac{\text{Standard Deviation}}{\text{Average}} * 100\% \quad (6)$$

$$\text{Fibre Volume Fraction} = \frac{\text{Volum of fibre}}{\text{Volum of object}} * 100 \quad (7)$$

CV of fibre volume fraction is a parameter that can be used to evaluate the quality of the final FRP structure [44]. After optimization of the VARTM process, the MRJ researchers were able to get a 2% CV value. Advanced forms of VARTM fabrication processes for FRP structures are also present in the ground-based and marine applications for the commercial and military industries, further information can be found in [48] [49] [50].

As the main focus of this research was to reduce the emissions of rail transportation, it was important to consider the processing method with the least energy consumption and CO_{2eq} emissions, without compromising the quality and integrity of the final component. A recent study applied a combined cost modelling and life-cycle assessment approach to compare the manufacturing process of a single panel design autoclaving to VARTM, referenced in [40]. In summary, the study provided quantitative data to locate the contribution to the total cost during each processing step, shown in Figure 33, and the contribution of the total CO_{2 eq} emissions by the energy used during each processing step, shown in Figure 34. The study also concluded that OoA processing achieved 50% CO_{2 eq} reduction versus autoclave usage.

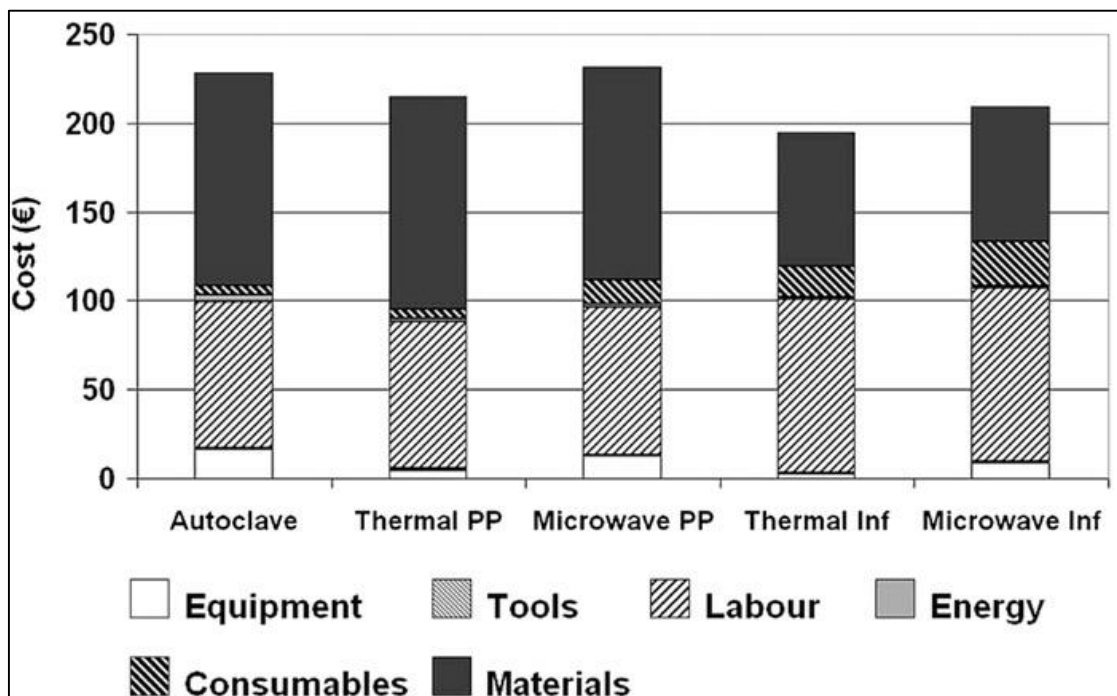


Figure 33: Cost per process showing contributions from equipment, tools, labours, energy, and consumables [40]

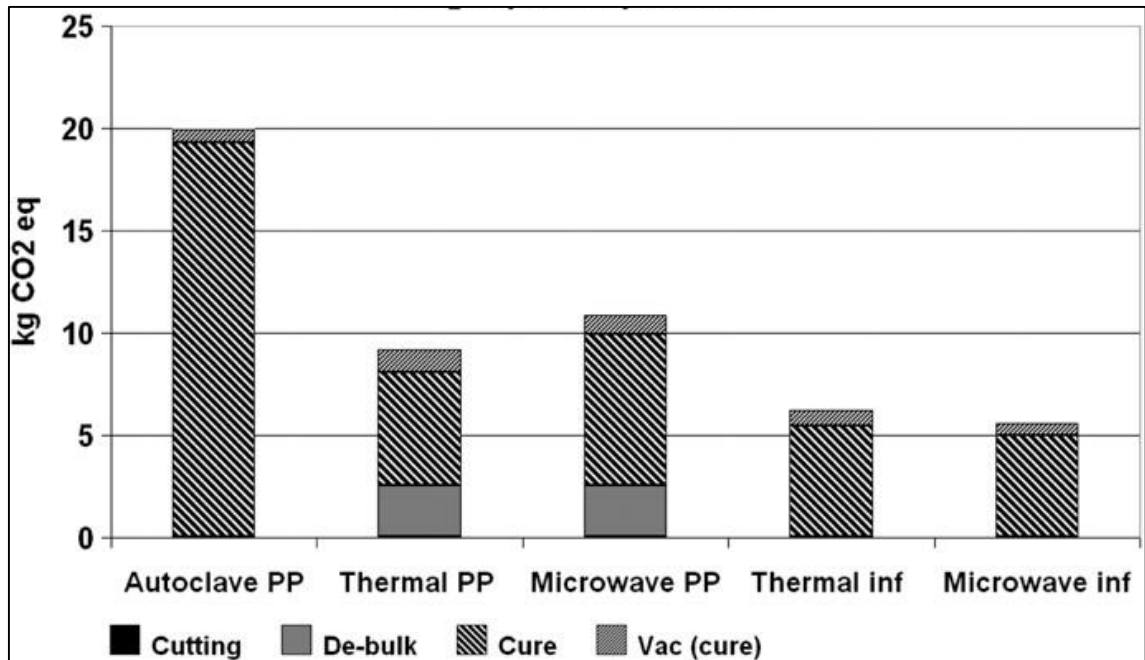


Figure 34: Total CO₂ eq emissions related to energy use during processing showing contributions from cutting, de-bulking, cure, and oven operation [40]

It is for these design trends and qualitative results from major industries, the thesis will focus on VARTM process as a viable candidate to manufacture the structural components of the hopper car.

4.3.1 VARTM Fabrication Processes

Vacuum assisted resin transfer moulding provides the ability to prepare the materials and perform the resin infusion at room temperature. It also provides a visual control of the filling stages through the transparent vacuum bag. VARTM, a subset of LRM, involves impregnation of resin into preformed dry fibres inside an air-tight bag. VARTM only needs one tool surface/mould, and the top surface has a bag finish. The resin can be cured at room temperature, hence cutting down on the costs associated with autoclaves and ovens. The disadvantages or limitations of VARTM are poor surface finish on the bagging side, time spent in material preparation, resin flow, and the need for post-infusion alteration to get to the net shape parts [37]. There are multiple

VARTM variants that rely on the resin flowing preferentially across the surface and simultaneously through the preform thickness enabling large parts to be fabricated, such as:

- Vacuum-assisted process (VAP) - patented by Premium Aerotec – used to produce the rear pressure bulkhead for the 787 Dreamliner [51];

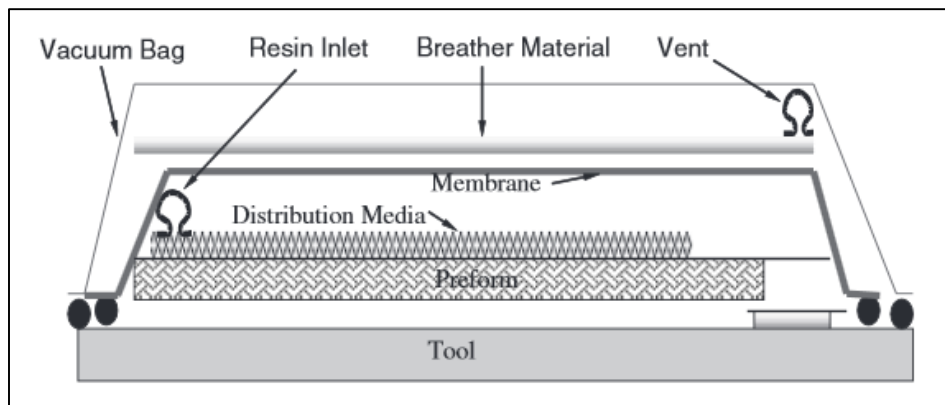


Figure 35: schematic diagram of a typical VAP setup [51].

- Controlled Atmospheric Pressure Resin Infusion (CAPRI) process – patented by Boeing Aerostructures – used to make the movable trailing edge control surfaces [52];

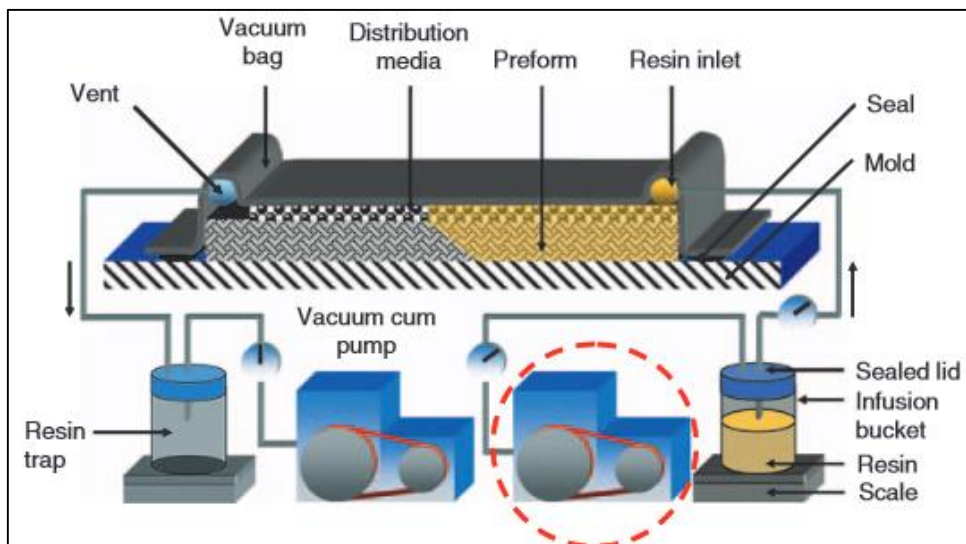


Figure 36: Schematic diagram of the CAPRI setup [52].

- Seeman Composites Resin Infusion Moulding Process (SCRIMP) used by TPI Composites in the manufacturing of wind blades [51]; and more.

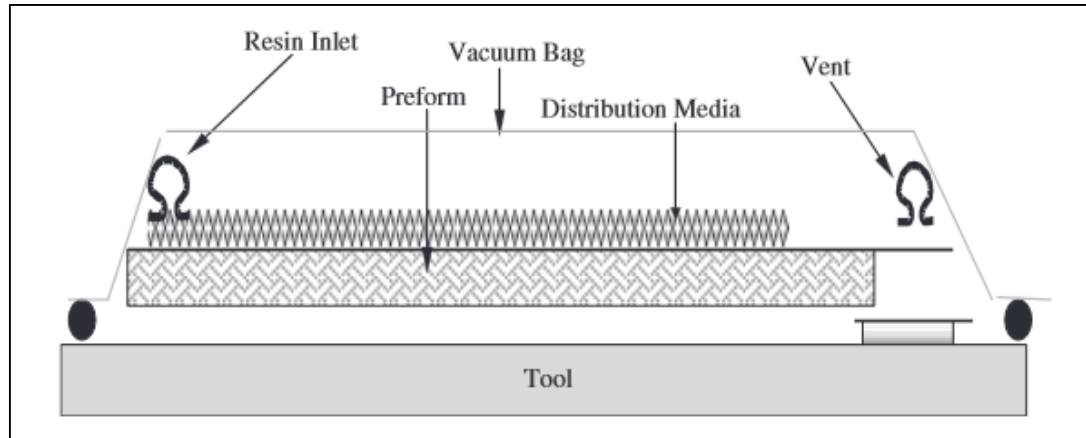


Figure 37: schematic diagram of SCRIMP setup [51].

4.3.2 Effects of Manufacturing On the Quality and Performance of the Final Product

Meeting the requirements defined in the previous chapter is highly dependent on the infusion process. Any alteration or variation in any of the manufacturing steps can have a direct effect on the quality and performance of the final product. The compaction and impregnation phases control the formation of defects such as voids and dry spots. In some cases, the compaction phase can cause misalignment in the fibres orientation or deformations in the preforms causing a buildup of residual stresses. The permeability of the preform can be controlled at this stage to ensure free flow of resin, which in turn has an effect on the impregnation phase. Bleeder materials and distribution channels are two possible solutions to avoid dry spots and formation of voids. Voids are one of many defects that can occur during the resin infusion process. Voids are considered to

be the most critical defect that can influence the mechanical properties of a composite laminate [53]. The presence of volatiles, water, or air bubbles can be identified as the main cause of voids. Voids can occur due to air entrapment in the mixture or resin reaction to water during cure [53]. A recent study, found in [54], examined the influence of voids on composite laminate strength and focused on automated resin infusion manufacturing process, particularly automatic tape laying of the fibre reinforcement. The study concluded that the strength properties decreased as shown in Table 10 in the range of 0 - 4% of void volume content. The void content or void volume fraction can be calculated using equations (8) and (9) [53]. Recently, Bombardier has been able to develop an OoA process with near 1% void content [45].

Table 10: material strength reduction in composite with void volume content in the range 0 - 4% [54].

Property	% Reduction in Property for Every % Increase in Void Content
Tensile strength, fibre direction	3.3
Shear strength	5.1
Transverse strength	12

$$\rho_c = \frac{1}{\left(\frac{w_f}{\rho_f}\right) + \left(\frac{w_m}{\rho_m}\right)} \quad (8)$$

$$V_v = \frac{\rho_c - \rho}{\rho_c} \quad (9)$$

Where

ρ_c = theoretical density

w_f and w_m = fibre weight fraction and matrix weight fraction, respectively

ρ_f and ρ_m = fibre density and matrix density, respectively

V_v = voids volume fraction

ρ = actual density measured experimentally

4.4 VARTM Fabrication Trials

4.4.1 VARTM Process Trial Methodology

A series of initial VARTM fabrication trials were carried out to identify specific challenges faced during the fabrication process, and observe any defects in the final part produced in the compaction and impregnation phases. Some of the observed defects were surface finish, dry spots, and void formations. Figure 38 is a schematic illustration of the stacking sequence in the VARTM setup used in the production the initial batch of flat panels. The fibres used in these trials were unidirectional fibreglass and unidirectional carbon fibre. A two-part infusion epoxy (Aeropoxy PR2032) was used as the resin system.

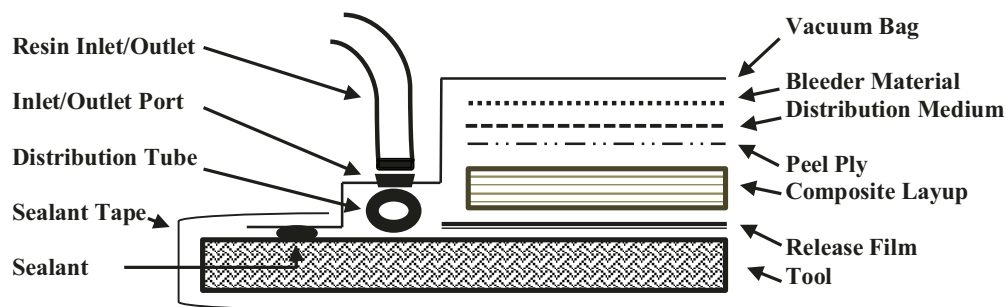


Figure 38: Schematic illustration of the setup of the VARTM process.

Figure 39 and Figure 40 show the final setup in the impregnation phase of the fibreglass and carbon fibre panels, respectively. Appendix C provides a step-by-step pictures of the material preparation.

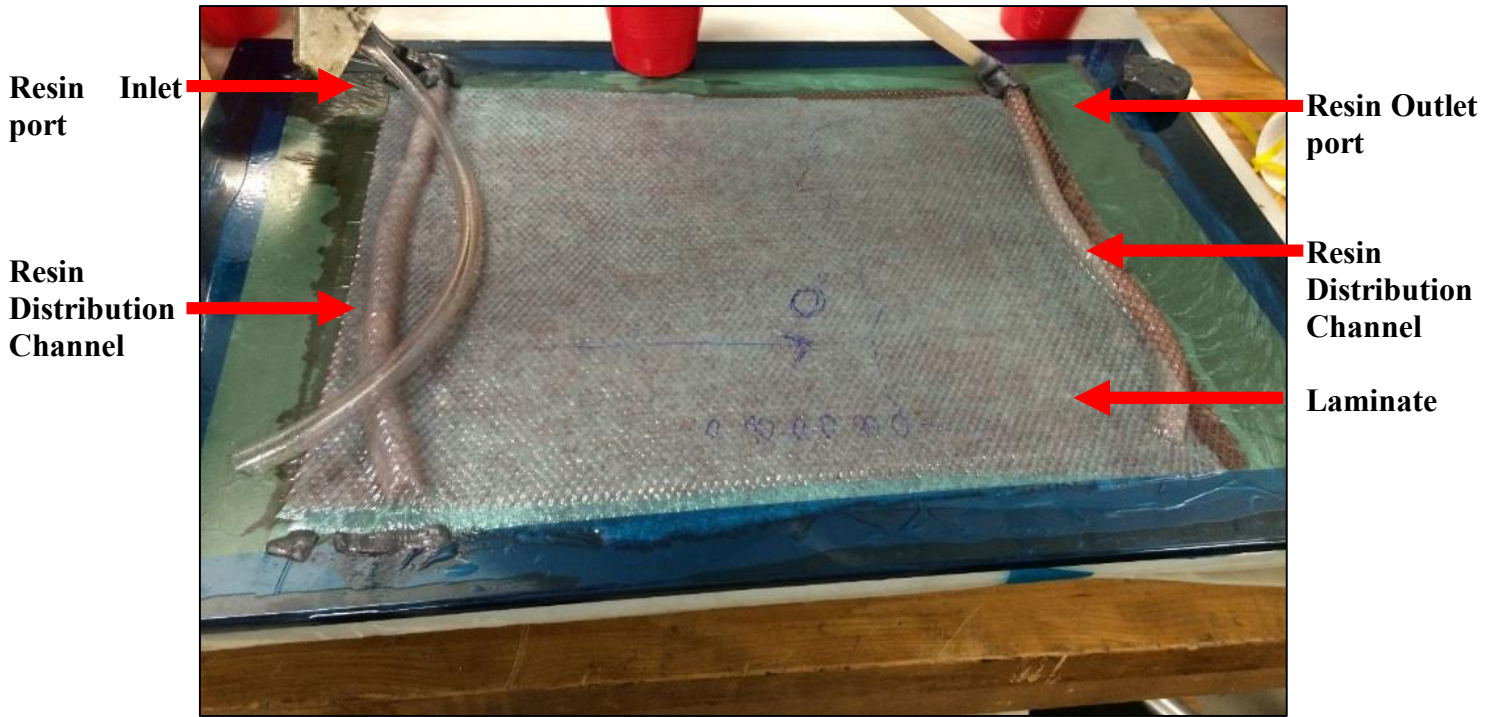


Figure 39: VARTM setup for a fibreglass panel, 0.33 m X 0.33 m.



Figure 40: VARTM setup for a carbon fibre panel, 0.15 m X 0.15 m.

4.4.2 VARTM Process Trial results and Discussion

The fibreglass panel was demoulded after sufficient time had elapsed for complete curing. Visual inspection of the panel revealed the presence of major defects that deemed the panel unacceptable. These defects are summarized in Figure 41.

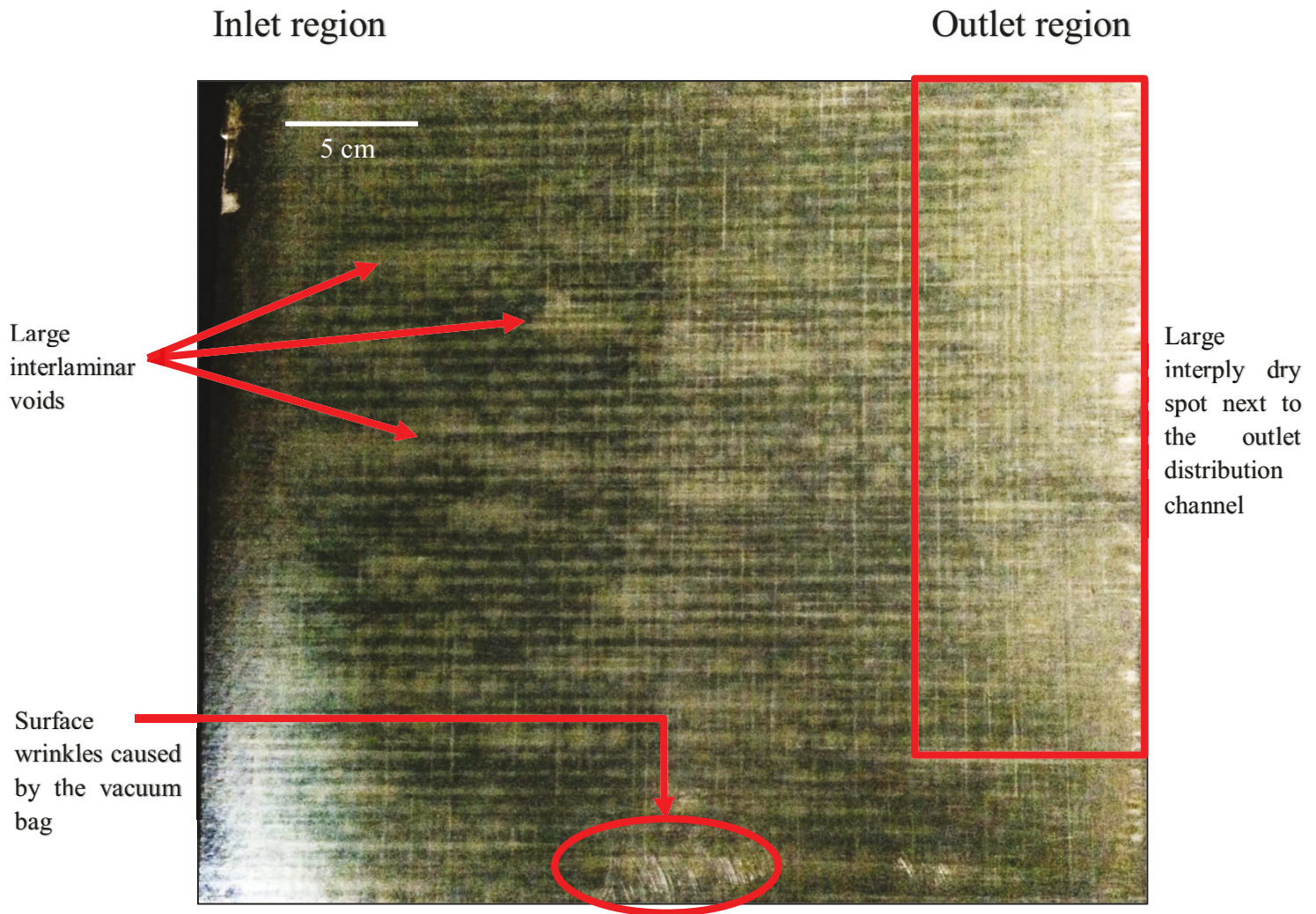


Figure 41: Fibreglass panel manufactured using VARTM showing major manufacturing defects

Figure 42 and Figure 43 show the surface finish on the both sides of the panel: facing the vacuum bag and facing the tool, respectively. The placement of the bagging material, such as distribution medium or breather cloth, left an imprint on the surface. The surface finish is important for surfaces that need to be coated or painted or require

a smooth finish for low aerodynamic drag. Therefore, the arrangement of bagging material, such as resin distribution mesh and breather cloth, has to be selected carefully to obtain a smooth surface.

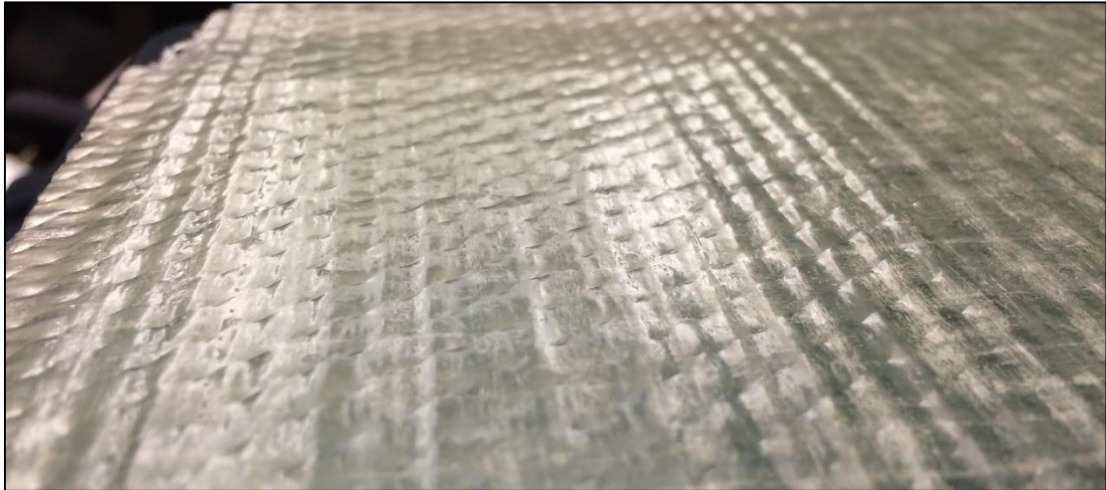


Figure 42: Top surface showing irregularities and roughness from contact with the distribution medium.



Figure 43: Bottom surface showing smoothness from contact with the tool.

The presence of dry spots on the bottom surface of the panels was another defect noticed in the final products. The dry spots were noticed to always be near the outlet distribution channel. The bright regions on the panels shown Figure 44 and Figure 45

provide a clear view of this major defect. The last panel produced, shown in Figure 45, was manufactured without a breather cloth. This was done as an attempt to force the resin to flow through the dry fibre. However, this had a negative impact on the resin flow path. It was noticed during the infusion phase that the resin started to follow the path of least resistance as soon as it reached the outlet distribution channel. This caused the resin to go through the distribution mesh without wetting out the fibres near the outlet.

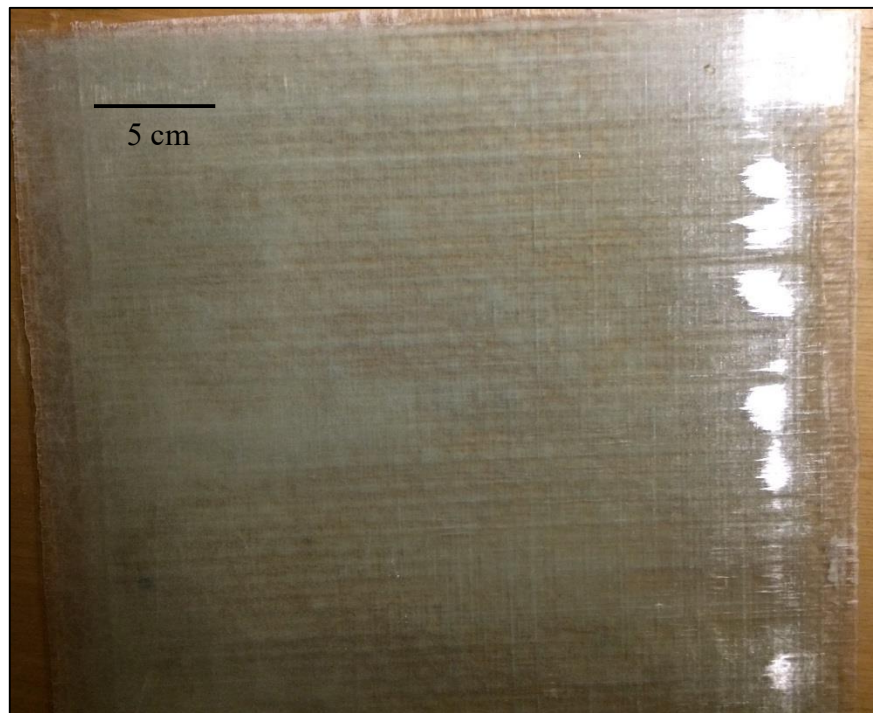


Figure 44: The bottom view of the first produced fibreglass panel showing the location of dry spots



Figure 45: The bottom view of the last produced fibreglass panel showing the location of dry spots.

These trials shed light on new manufacturing issues that were not considered before experiencing the fabrication process personally. The first encountered issue was the appearance of void growth inside the preform during the resin infusion stage. A leak in the bag seal was not found after extensive inspection that raised suspicion about the cause of void formation. Researching this phenomenon revealed a new problem faced by manufacturers during resin infusion: water vapour. Water is often considered to be the main cause of void formation in the preform [37]. Moisture or humidity in the surrounding environment can be entrapped in the preform, bagging materials, or transferred into the system during the compaction cycles. This entrapped moisture can cause voids to appear in the system. Void growth is directly influenced by the vacuum pressure. Void formation and growth will potentially occur when the volatile vapour pressure exceeds the hydrostatic liquid pressure. Liquids can vaporise into large volume of gas if high enough vacuum is applied on the system [55, p. 184]. In thermodynamics,

the phase diagrams show the relationship between the state of a substance at different pressure and temperature values. Therefore, it is possible for liquids to boil or convert into vapour under reduced temperatures when vacuum is applied, further explanation of the thermodynamic principles can be found in [56, pp. 91 - 142]. Therefore, the growth of voids gave a false appearance of leak in the setup.

The second issue encountered was the presence of dry spots in the laminates. This can be attributed to the low permeability of the chosen material or the location of the injection ports and distribution channels. Figure 46 shows a top-view picture of the setup for one of the fibreglass panels. During infusion, the resin was observed to flow through the bottom region of the panel where the distribution channel extended 1 cm further than the preform. It was clear that the resin followed the path of least resistance; hence, a direct flow path between the inlet and outlet distribution channels was established within 12 minutes of infusion.

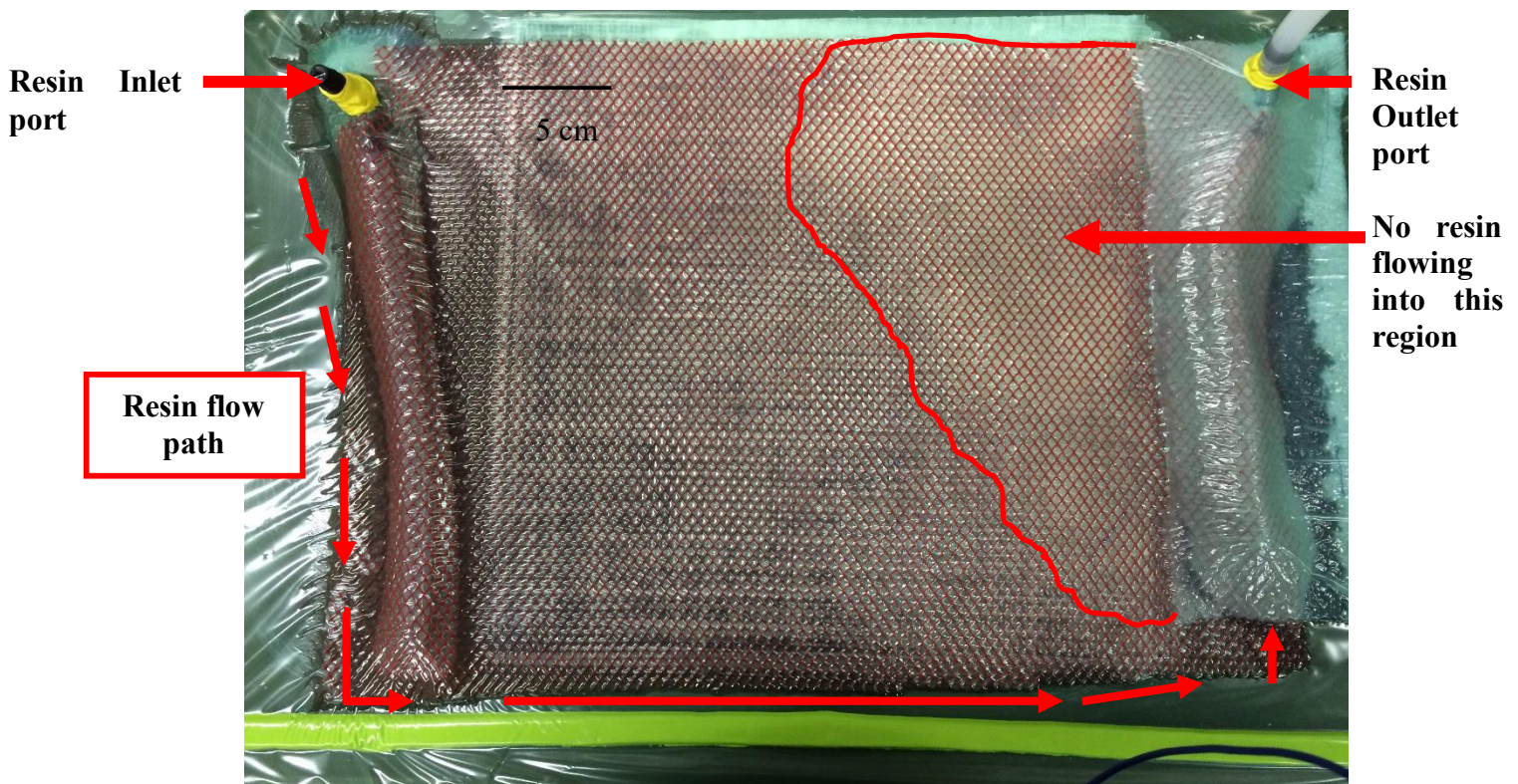


Figure 46: Inlet and distribution channel location caused the resin to flow straight to the outlet port.

Chapter 5

Structural Analysis of Improved Sidewall Design

This chapter describes the static analysis of an FRP sidewall structure in accordance with the design requirements presented in Chapter 3. The static analysis aims at computing the stress distribution and horizontal deflection of the sidewall panels due to the static load of the lading. In the following sections, the derivation of thin plate theory is presented and the set-up for finite element analysis using commercial software is described and the results of these analyses are discussed.

5.1 Thin Plate Theory and Comparison to Finite Element Analysis

Thin plate theory was used to achieve two objectives:

- To ensure that the FEA software was used correctly to model the sidewall panels by comparing the maximum stress and deflection values obtained using the FEA modeling software to values obtained independently using thin plate theory; and,
- To examine the effect of the boundary conditions on the sidewall panels to support joint selection described in 5.4.

The thin plate theory was first used to calculate the theoretical deflection and maximum stress values of a thin steel plate with a uniformly distributed load applied to its surface. The steel plate was 1.6 m long and 1 m wide with a thickness of 0.01 m.

Technical literature in classical plate theory provides derivations of the equations, as described in [57] [58] [59]. The classical thin plate theory has three assumptions according to [59]:

- 1- Transverse normal (straight lines perpendicular to the mid-surface) before deformation remain straight after deformation,
- 2- Transverse normal are inextensible (do not experience elongation)
- 3- Transverse normal rotate such that to remain normal to the mid-surface after deformation

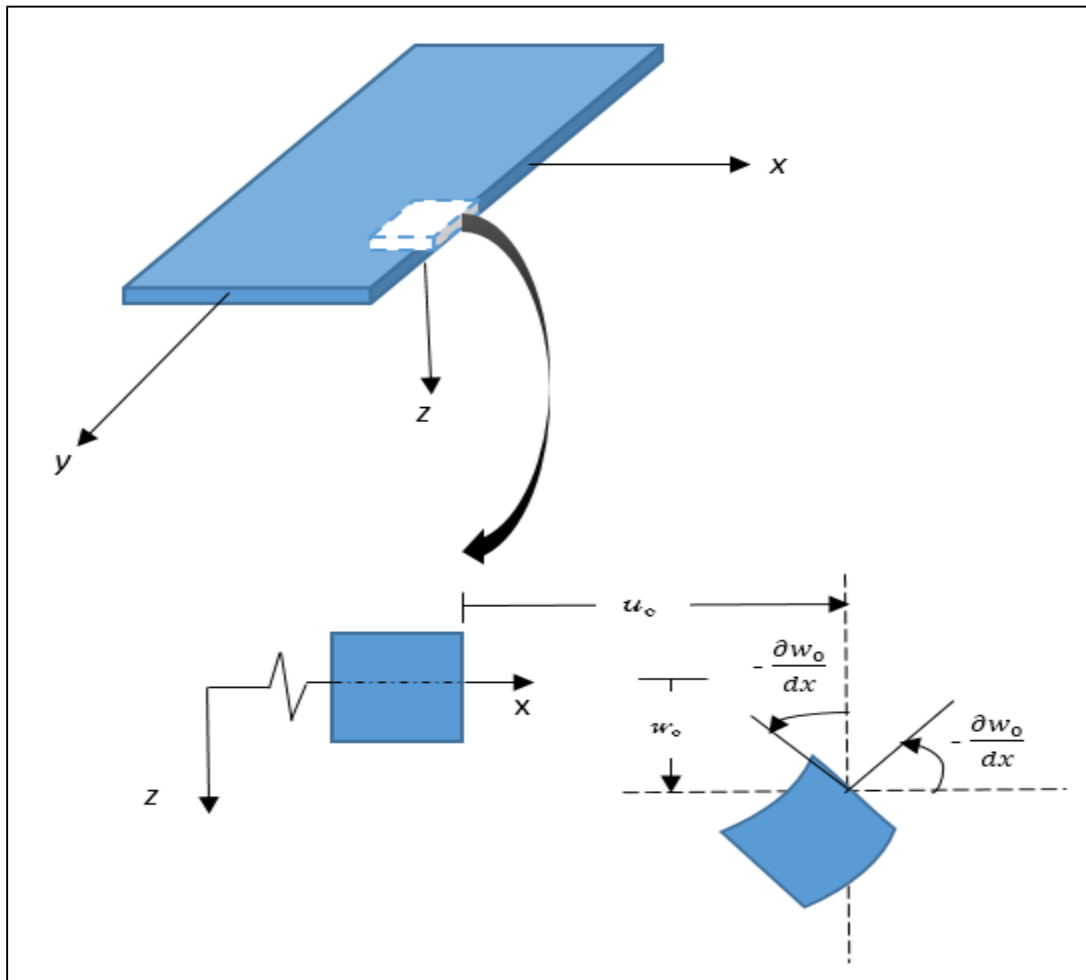


Figure 47: Schematic representation of the Kirchhoff assumptions for unreformed and deformed geometries edge of a plate [59].

Assumptions 1 and 2 imply that the through-thickness strain is zero [59]. This is mathematically represented in equation (10) [59]:

$$\varepsilon_{zz} = \frac{\partial w}{\partial z} = 0 \quad (10)$$

Assuming that (u, v, w) denote the total displacement of a point along the (x, y, z) coordinates, Equation (10) implies that the w is independent of z .

In addition, assumption 3 implies zero transverse shear strains. This is mathematically represented in equation (11) [59]:

$$\varepsilon_{xz} = \frac{\partial u}{\partial z} + \frac{\partial w}{\partial x} = 0, \quad \varepsilon_{yz} = \frac{\partial v}{\partial z} + \frac{\partial w}{\partial y} = 0 \quad (11)$$

As a result, the Kirchhoff hypothesis becomes a simplified version of the displacement in u , v , and w directions shown in the equations below [59]:

$$u(x, y, z, t) = u_o(x, y, t) - z \frac{\partial w_o}{\partial x} \quad (12)$$

$$v(x, y, z, t) = v_o(x, y, t) - z \frac{\partial w_o}{\partial y} \quad (13)$$

$$w(x, y, z, t) = w_o(x, y, t) \quad (14)$$

where (u_o, v_o, w_o) is the displacement of a material point at $(x, y, 0)$ in the (x, y, z) coordinate direction. It is assumed that the mid-surface remains unstrained after bending because the displacements of the plate are small. Therefore u_o, v_o are zero. In addition, knowing that strain can be written as [60]:

$$\varepsilon_x = \frac{\delta u}{\delta x}, \quad \varepsilon_y = \frac{\delta v}{\delta y}, \quad \varepsilon_z = \frac{\delta w}{\delta z} \quad (15)$$

Therefore, Equations (13), (14), and (15) can be written in the general form as:

$$\varepsilon_x = -z \frac{\delta^2 w}{\delta x^2}, \quad \varepsilon_y = -z \frac{\delta^2 w}{\delta y^2}, \quad \varepsilon_z = \frac{\delta w}{\delta z} \quad (16)$$

Using the constitutive equations shown in Equation (17) to relate stress components to strain components, stress components can be written equation (18) [60].

$$\sigma_x = \frac{E}{1 - \nu^2} (\varepsilon_x + \nu \varepsilon_y), \quad \sigma_y = \frac{E}{1 - \nu^2} (\varepsilon_y + \nu \varepsilon_x), \quad \tau_{xy} = G \gamma_{xy} \quad (17)$$

$$\begin{aligned}
\sigma_x &= -\frac{Ez}{1-\nu^2} \left(\frac{\partial^2 w}{\partial x^2} + \nu \frac{\partial^2 w}{\partial y^2} \right) \\
\sigma_y &= -\frac{Ez}{1-\nu^2} \left(\frac{\partial^2 w}{\partial y^2} + \nu \frac{\partial^2 w}{\partial x^2} \right) \\
\tau_{xy} &= -\frac{Ez}{1-\nu} \frac{\partial^2 w}{\partial x \partial y}
\end{aligned} \tag{18}$$

Equation (18) shows the law of variation of stresses through the thickness of the plate based on the Kirchhoff's assumptions. The total statically equivalent forces and moments, also known as stress resultants and stress couples, applied on to the middle surface can be introduced instead of the stress components at a point.

The stress resultant and stress couples can be defined as shear forces (per unit length) , Q_x and Q_y , and bending and twisting moments (per unit length) as M_x , M_y , and M_{xy} , respectively. $M_{xy} = M_{yx}$ because of the reciprocity law of shear stresses ($\tau_{xy} = \tau_{yx}$). These parameters can be seen acting on an element in Figure 48. Shear forces, bending and twisting moments can be written in terms of the stress components shown in equation (18) [60]:

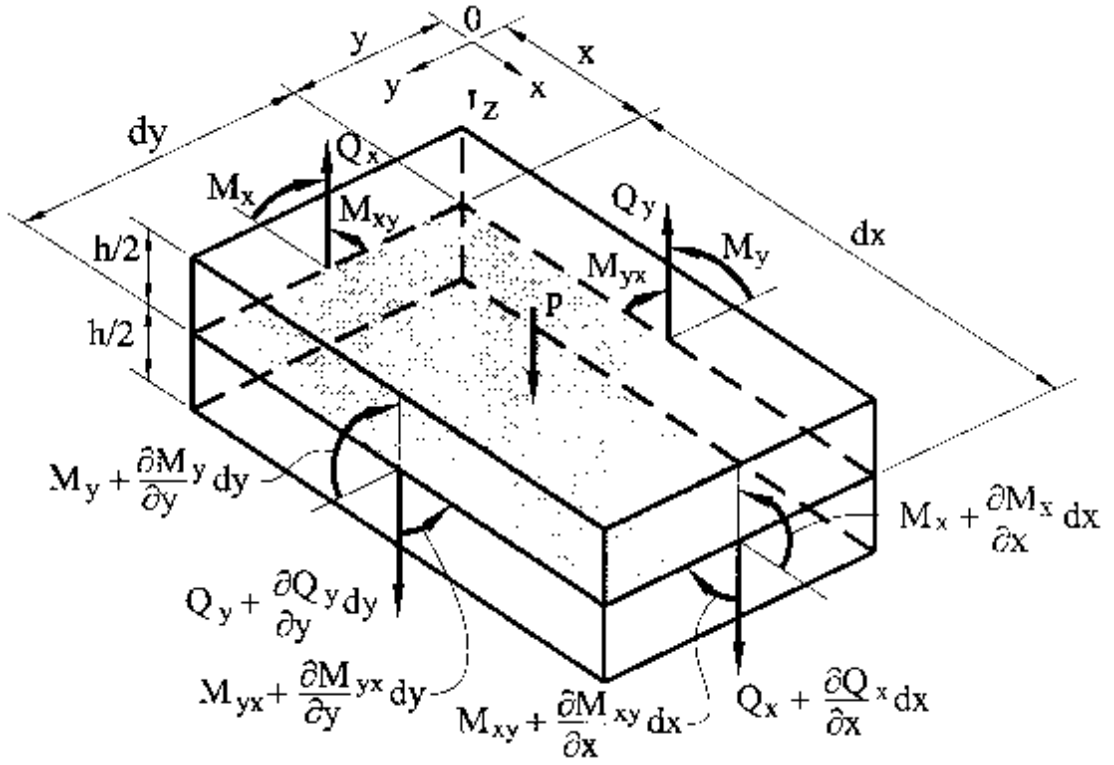


Figure 48: Positive shear forces and moments and distributed lateral load, q [N], shown on a plate element [60].

$$\begin{aligned} \begin{Bmatrix} M_x \\ M_y \\ M_{xy} \end{Bmatrix} &= \int_{-h/2}^{h/2} \begin{Bmatrix} \sigma_x \\ \sigma_y \\ \sigma_{xy} \end{Bmatrix} z dz \\ \begin{Bmatrix} Q_x \\ Q_y \end{Bmatrix} &= \int_{-h/2}^{h/2} \begin{Bmatrix} \tau_{xz} \\ \tau_{yz} \end{Bmatrix} dz \\ &= \int_{-h/2}^{h/2} \left\{ \begin{aligned} \int_{-h/2}^{h/2} \frac{E \left(z^2 - \frac{h^2}{4} \right)}{2(1-\nu^2)} \frac{\partial}{\partial x} \left(\frac{\partial^2 w}{\partial x^2} + \frac{\partial^2 w}{\partial y^2} \right) \\ \int_{-h/2}^{h/2} \frac{E \left(z^2 - \frac{h^2}{4} \right)}{2(1-\nu^2)} \frac{\partial}{\partial y} \left(\frac{\partial^2 w}{\partial x^2} + \frac{\partial^2 w}{\partial y^2} \right) \end{aligned} \right\} dz \end{aligned} \quad (19)$$

Substituting equation (19) into equation (18) and integrating over the thickness of the plate [60]:

$$M_x = -D \left(\frac{\partial^2 w}{\partial x^2} + \nu \frac{\partial^2 w}{\partial y^2} \right) \quad (20)$$

$$M_y = -D \left(\frac{\partial^2 w}{\partial y^2} + \nu \frac{\partial^2 w}{\partial x^2} \right)$$

$$M_{xy} = M_{yx} = -D(1 - \nu) \frac{\partial^2 w}{\partial x \partial y}$$

where $D = \frac{Eh^3}{12(1-\nu^2)}$

Substituting Equation (20) into Equation (18) [60] gives the following equation necessary to calculate the maximum stress values:

$$\sigma_x = \pm \frac{12M_x}{h^3} z, \sigma_y = \pm \frac{12M_y}{h^3} z, \tau_{xy} = \frac{12M_{xy}}{h^3} z \quad (21)$$

After multiple steps of derivations, that can be found in [60, pp. p. 24 - 25] , the governing differential equation for the deflections [60]:

$$\frac{\partial^4 w}{\partial x^4} + 2 \frac{\partial^4 w}{\partial^2 x \partial^2 y} + \frac{\partial^4 w}{\partial y^4} = \frac{p}{D} \quad (22)$$

where p is a vertical distribution load of intensity p(x,y) [N]

Solutions for equation (22) can be found in literature depending on the boundary conditions of the plate. There are various approaches to solve equation (22), such as: Levy solution, Ritz solution, and Navier solution. Each approach depends on the boundary conditions and applied load. The thin plate theory was used to calculate the maximum stress and deflection for the thin steel plate, described in the beginning of this section, under uniform load to ensure that the results predicted from the FEA model agreed with the analytical results. These results are summarized in Table 12 for the following boundary conditions:

- All sides simply supported (SSSS)
- long sides simply supported and short sides clamped (CCSS)

- short sides simply supported and long sides clamped (SSCC)
- all sides clamped (CCCC)

The same set-up was modelled using ABAQUS, a commercial FE analysis software. First, a mesh convergence analysis was performed on the steel plate for each boundary condition. Table 11 demonstrates a trial mesh convergence analysis performed on the plate with all sides pinned (SSSS). This was done to determine the element size required in the model to ensure that the results were not affected by changes in the mesh size. Once the element size was determined, the stress and deflection values were determined for each of the boundary conditions listed earlier. The stress distribution and deflection contour plots can be seen in Figure 50 and Figure 51 for the plate with all sides pinned. In addition, Figure 62 to Figure 65 in Appendix D show the stress distribution on the plate for each boundary condition scenario.

The results obtained from the model were compared to those obtained from the thin plate theory explained earlier. Table 12 summarizes the deflection and maximum stress values for each boundary condition obtained from the thin plate theory and FE analysis. Notice that the deflection values obtained from ABAQUS were in close agreement with the theoretical values, approximately 2% difference on average. On the other hand, the stress values obtained from ABAQUS had 10% average difference from the theoretical value.

Table 11: Mesh convergence for a simply supported plate under bending.

Number of Elements	Stress [Pa]	Percent Difference	Deflection [mm]	Percent Difference
40	10948114		0.0010866	
160	11909529	8.07265	0.0011525	5.718
198	11855686	0.45415	0.0011418	0.93712
260	11919109	0.53211	0.0011463	0.39257
322	11978340	0.49448	0.0011524	0.52933
459	11977706	0.00529	0.0011492	0.27845
640	12047058	0.57568	0.0011561	0.59683
1000	12050054	0.02486	0.0011546	0.12992
1749	12070565	0.16993	0.0011560	0.12111
4000	12101852	0.25853	0.0011590	0.25884
16000	12272057	1.38693	0.0011601	0.09482
19758	12224483	0.38917	0.0011601	0
25000	12117720	0.88105	0.0011602	0.00862
32747	12118652	0.00769	0.0011603	0.00862
44589	12119705	0.00869	0.0011604	0.00862

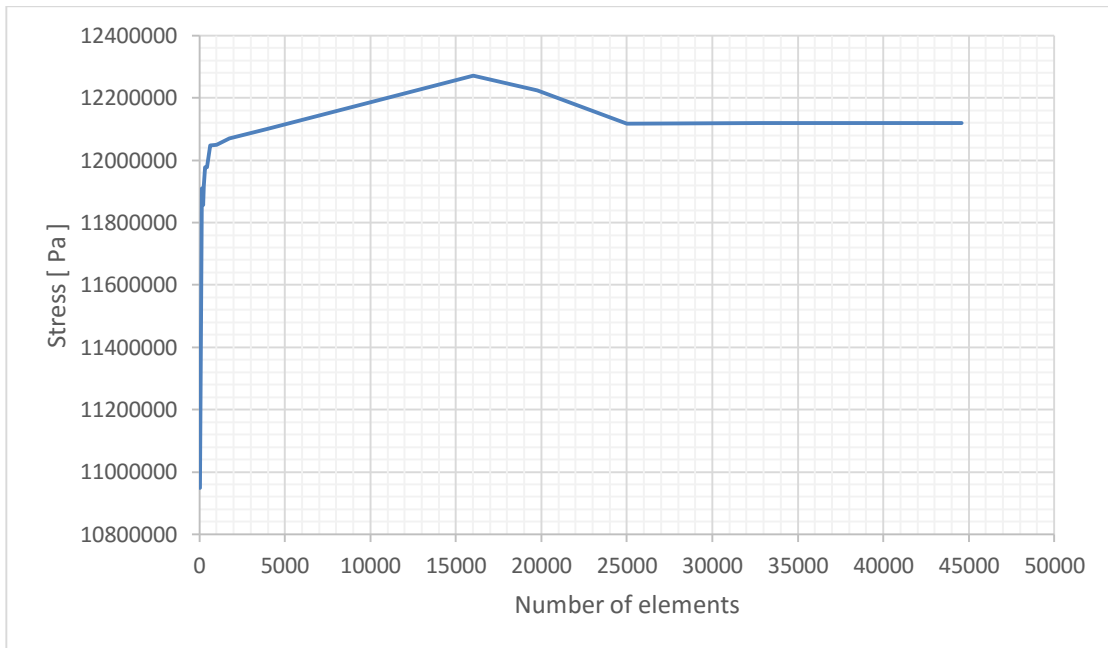


Figure 49: Convergence curve of stress based on the number of elements.

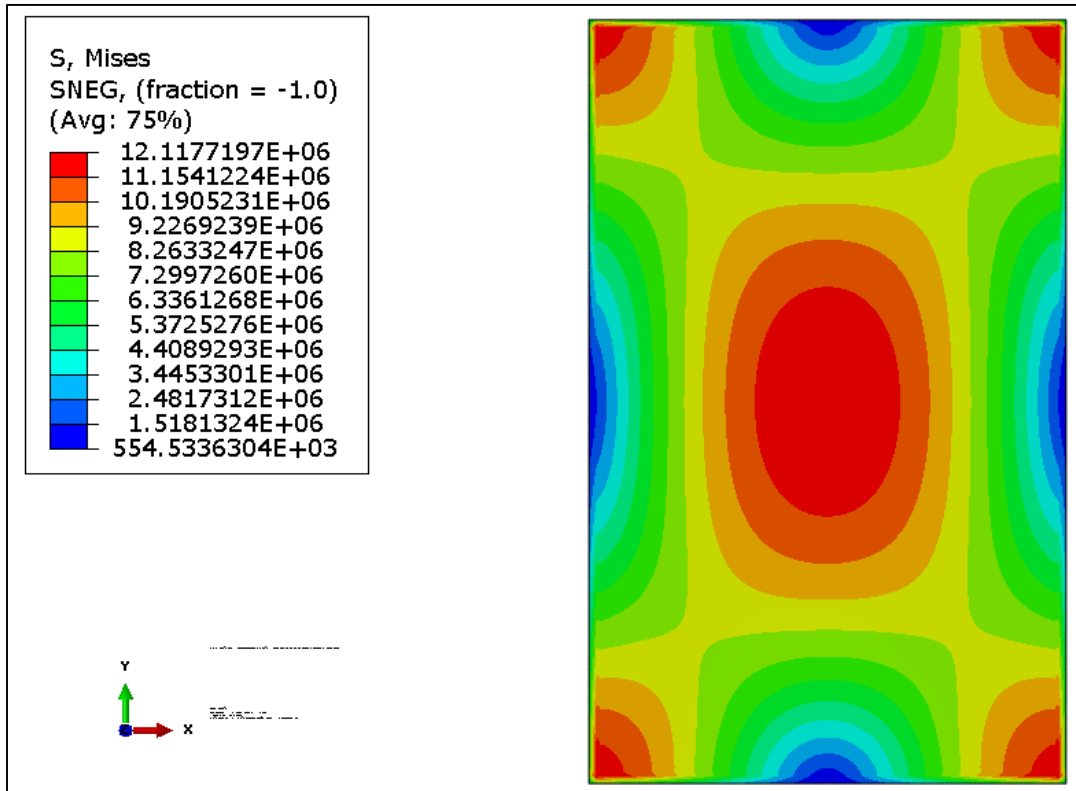


Figure 50: Stress distribution, in 2600 Pa, of a simply supported thin plate under 2600 Pa transverse pressure.

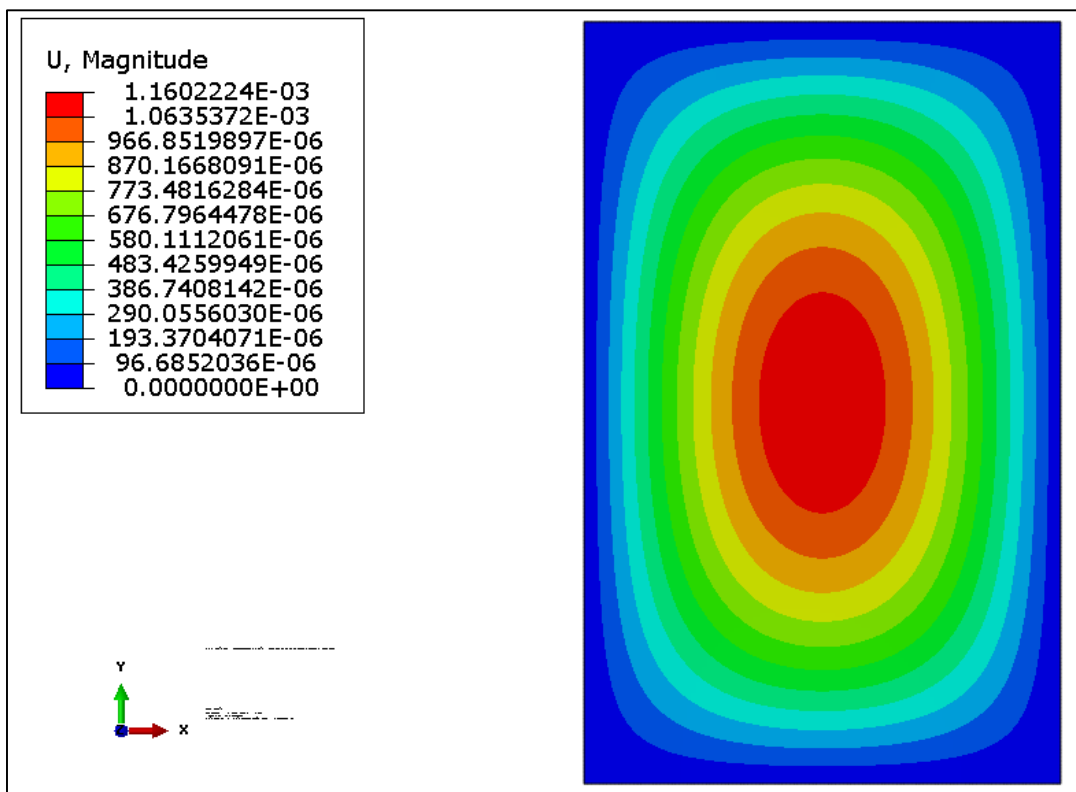


Figure 51: Deflection plot, in m, of a simply supported thin plate under 2600 Pa transverse pressure.

Table 12: Summary of the results obtained from ABAQUS and thin plate theory for different boundary condition at the same number of elements, 25000.

		All Sides Pinned	Long Sides pinned, short sides clamped	Short sides pinned, long sides clamped	All sides clamped
Stress [MPa]	ABAQUS	12.12	14.63	11.67	10.55
	Thin Plate Theory	13.47	17.00	13.00	12.17
Percent Difference		10	14	10	13
Deflection [m]	ABAQUS	1.1160e-3	8.51e-4	3.58e-4	3.267e-4
	Thin Plate Theory	1.1778e-3	8.55e-4	3.55e-4	3.263e-4
Percent Difference		5	0.5	1	0.1

5.2 FEA Setup and Assumptions

- The sidewalls of the proposed design have similar geometrical features of those found on the hopper car shown in Figure 11;
- The sidewall was assumed to be a long and continuous panel that extends horizontally from end to end;
- The sidewall was assumed to be flat and have stiffeners evenly spaced along its length, as shown in Figure 52; and,
- The sidewall was subjected to a lateral pressure distribution. The pressure distribution was calculated using equation (1), shown below.

$$P = \frac{1}{2}Wh^2 \frac{1 - \sin\theta}{1 + \sin\theta} \quad (23)$$

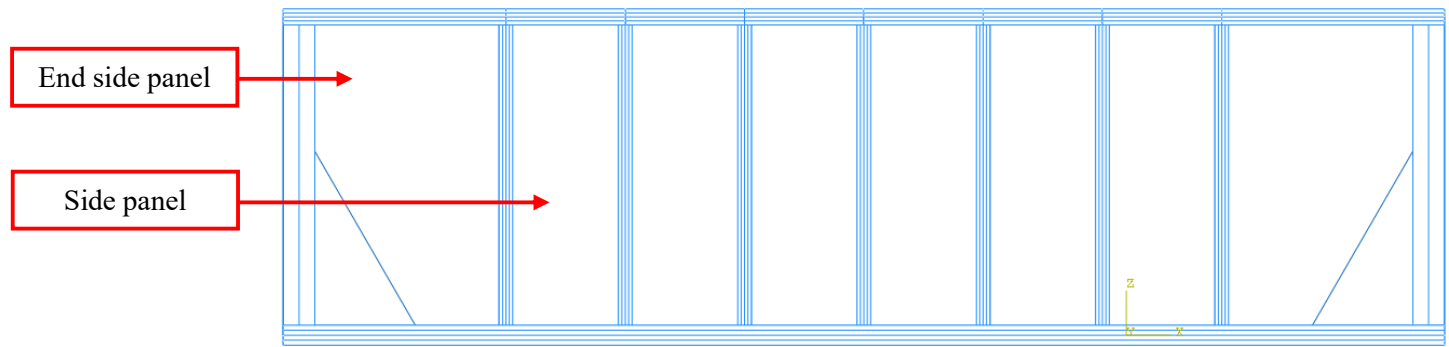


Figure 52: Front view of a complete sidewall built in ABAQUS.

The dimensions of the sidewall features were obtained from the Transverse Ultra Fast-Flow Coal car, produced by National Steel. The sidewall would be made up of a single and continuous panel that runs along the length of the train. However, the sidewall was divided into multiple side panels in the FE analysis that fit between adjacent stiffeners. The height and width of the side panel were 1.676 meters (66 inches) and 1.0668 meters (42 inches), respectively. The FRP panel was modelled using shell elements. This was mainly because the dimensions of thickness in comparison to the total length and width of the plate was in magnitudes of order smaller. This allowed for a faster computational time and simpler numerical analysis.

The numerical FE analysis was performed on a component level to study the effect of using FRP on the change of the structural weight of the panel(s). To simplify the analysis, a single panel between two stiffeners was analysed, and symmetry was placed on the vertical edges to. In addition, the side sills were assumed to be rigid beams with high stiffness. In addition, the stiffeners were assumed to have a high flexural rigidity, i.e. the beams can withstand the load of the lading without bending. It was assumed during the analyses that the sidewall serves the purpose of containing the bulk material inside the railcar. Finally, the side sills and stiffeners were assumed to react to the dynamic forces caused by movement of the railcar. Therefore, the side panels were

assumed to carry no shear force, as the beams will react to shear forces. These boundary conditions are illustrated in Figure 53.

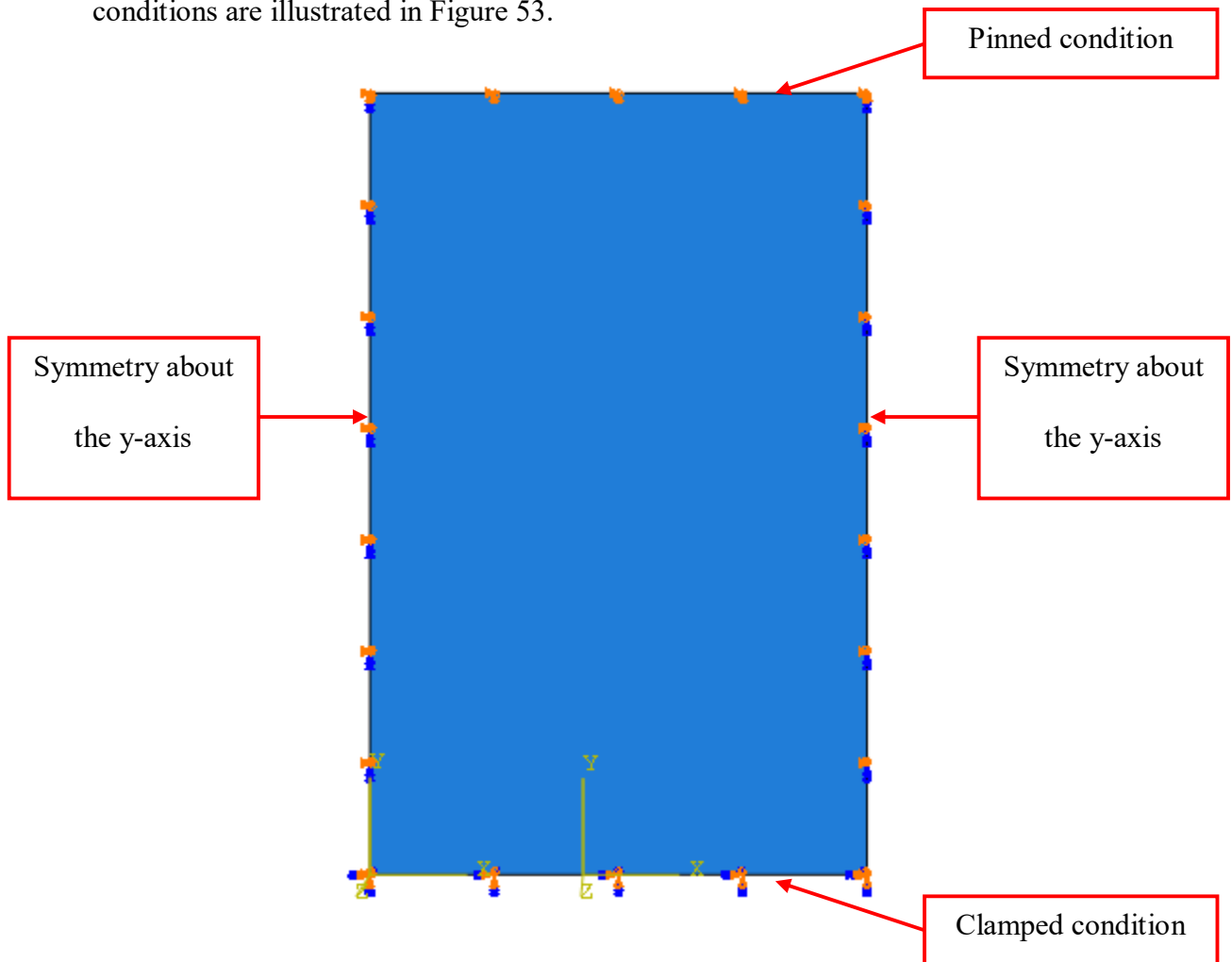


Figure 53: shell model of the steel plate with clamped condition at the bottom and simply supported everywhere else.

5.3 FE Analysis of Steel and FRP Side Panels

First, a steel panel structure was modeled using ABAQUS in accordance with the requirements of the AAR standards. The objective of modeling a steel panel structure was to determine the maximum stress, strain, and deflection values on a single panel between two stiffeners rather than modelling the entire sidewall, hence decreasing the time and computational power required to model an entire sidewall. The information gathered from this numerical FE analysis was used as a baseline for comparison and to create a specific FRP layup for each of the two selected fibre options: aramid and fibreglass.

During the FEA of FRP side panels, envelope plots (a contour plot of the highest or lowest value of a variable in a laminate, regardless of the ply in which it occurred [61]) were used to optimize the laminate design by determining highest stress and strain values in the longitudinal and transverse directions. This was later used to reduce the extreme values by reorienting existing plies and/or increase the number of plies in the laminate. Furthermore, through thickness plots were produced in the location of extreme values to examine the behaviour of the plies across the layup. To ensure the design does not fail, the maximum stress theory, found [37, p. 195], was used to directly compare the maximum stress experienced by the laminate with its strength. In addition, the maximum strain theory, found in [37, p. 199], was used to compare the highest and lowest strain levels in the laminate with the strain limits for the materials. The materials used in the FE analysis are shown in Table 13. In addition, the laminate layups were orthotropic cross-ply, symmetric, and balanced layups which can be seen in Figure 54. The driving factor to choosing the laminate layup was to match or come close to the original thickness of the cut out steel plate, which was 6.25 mm. Different stacking sequences were examined for maximum deflection and failure modes. The layup had to be symmetric to remove the bending-extension coupling in the FRP layup. This is very for fabrication because curing, and subsequently cooling, of FRP laminates induce thermal forces that can cause warping in the final FRP plates [37].

Table 13: Typical properties of unidirectional fibre reinforced composites [62] .

Properties	Glass/epoxy, E-glass	Aramid/epoxy, Kevlar 49
Density [kg/m ³]	1800	1360
Fibre volume fraction	0.45	0.7
<i>Strength properties</i>		
Longitudinal tension [MPa]	1062	1400
Longitudinal compression [MPa]	610	235
Transverse tension [MPa]	31	12
Transverse compression [MPa]	118	53
In-plane shear [MPa]	72	34

<i>Elastic constants</i>		
Longitudinal modulus [GPa]	38.6	76
Transverse modulus [GPa]	8.27	5.5
Shear modulus [GPa]	4.14	2.3
Major Poisson's ratio	0.26	0.34
<i>Failure strains (%)</i>		
Longitudinal tension	2.8	1.8
Longitudinal compression	1.6	0.31
Transverse tension	0.4	0.22
Transverse compression	1.4	0.96
In-plane shear	1.7	1.5

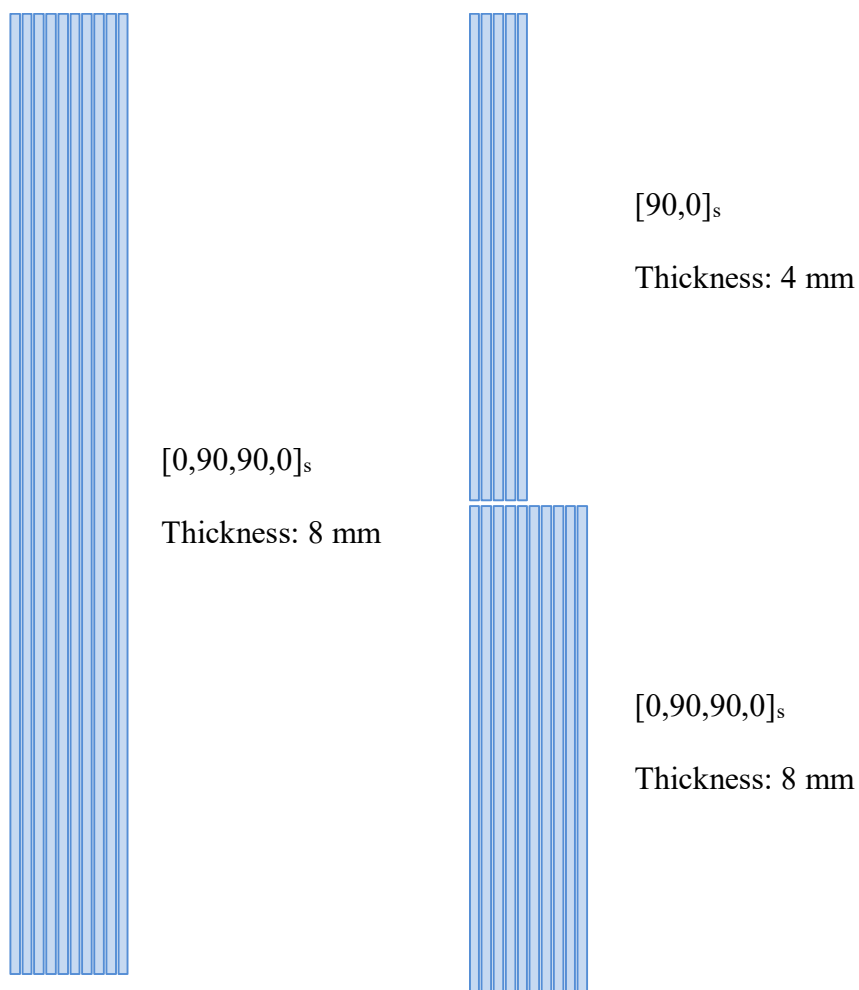


Figure 54: Proposed laminate stacking sequences for both FRP material options.

5.4 Structural Analysis Results and Discussion

Figure 55 and Figure 56 show the stress distribution and deflection of the steel panel when subjected to a lateral pressure calculated using equation (1). The top 0.5 m of the steel panel was observed to have the lowest stress levels. This was taken into account during the design of the FRP side panels. The information gathered from the FE analyses on a single FRP side panel was used to estimate the structural weight savings and panel deflection of a hopper railcar. Table 14 summarizes these values.

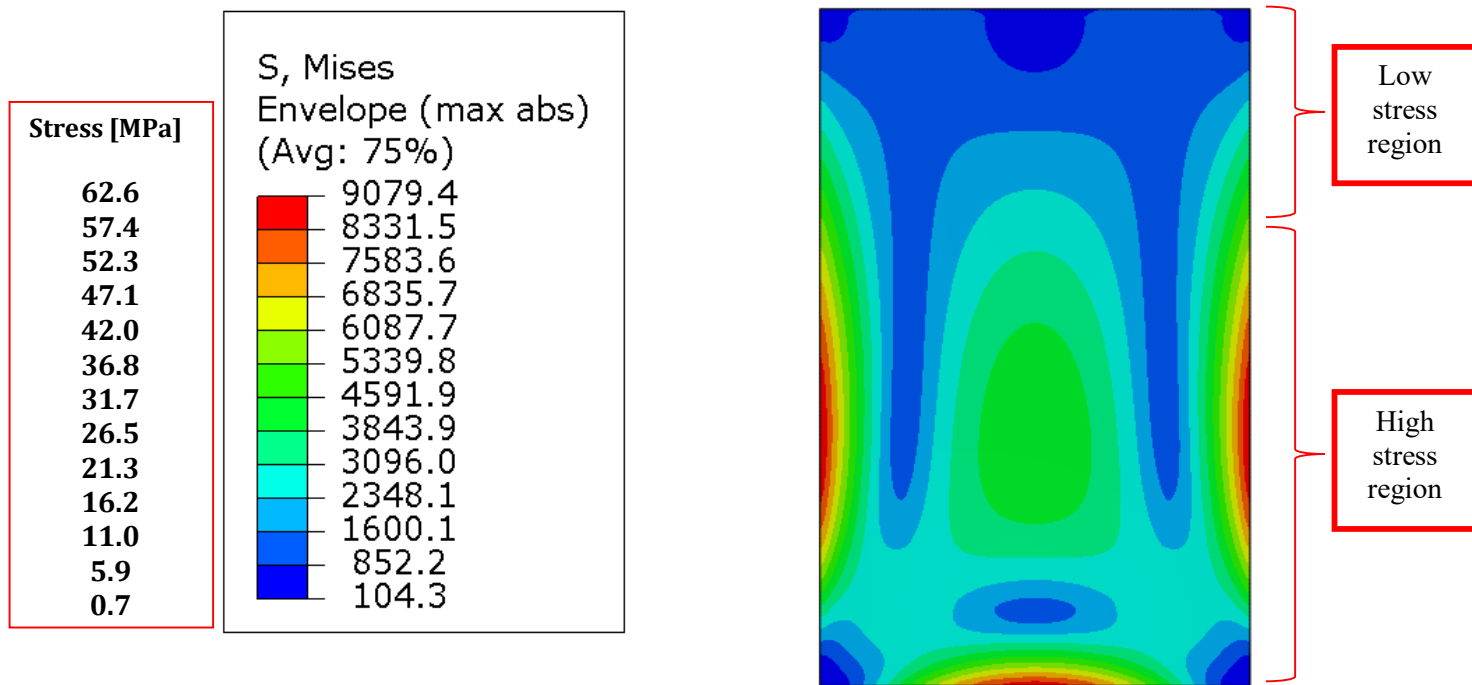


Figure 55: The stress distribution, in psi and MPa, shown on the front view of the steel panel

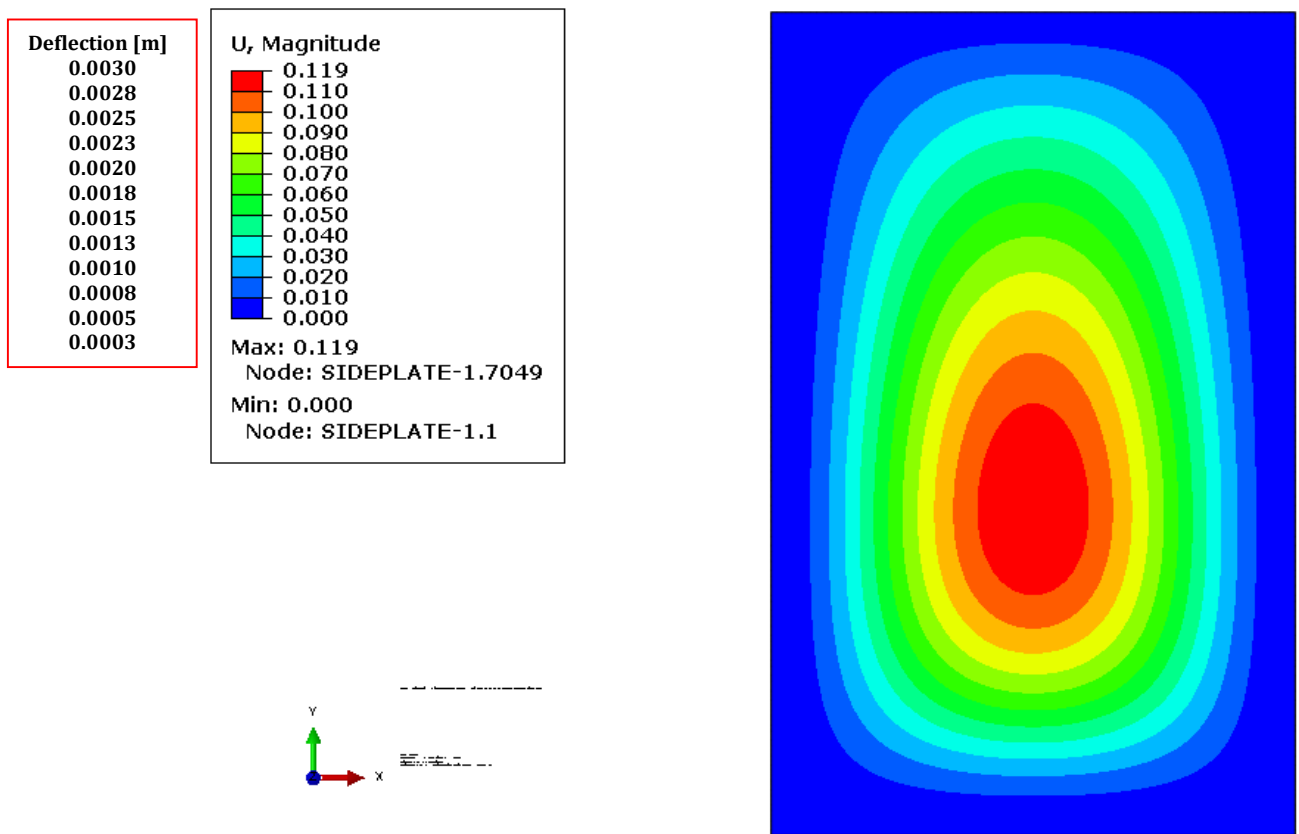


Figure 56: Deflection of the steel panel, in inches and m.

Table 14: Summary of key results obtained from FE analysis.

	Through-thickness Alteration	Out-plane Deflection [mm]	Estimated Percent Weight Reduction per Panel	Estimated Percent Weight Reduction per Railcar
E-glass/epoxy	Untailored	6.8	63	5
	Tailored	8.6	76	5.9
Aramid/epoxy	Untailored	5.4	72	5.7
	Tailored	6.7	81	6.4
Aluminium	Untailored	6.1	64	5.1

The AAR requirements mandate a maximum weight limit for any railcar type. Hence, the maximum lading to be carried by a hopper railcar is limited by the empty structural weight and total allowable weight of the railcar. To increase the maximum lading capacity, a reduction in the structural empty weight was achieved by substituting steel with FRP material in the sidewalls. Both materials showed significant weight

reduction. As an example, the untailed E-glass/epoxy had the lowest weight reduction per panel of 63% due to its higher density when compared to aramid/epoxy. This translates to 5% potential weight reduction from the total empty weight of a hopper railcar with flat sidewalls. Note that this value does not include potential reductions in the end side panel and end plates due to their geometrical complexities.

It is important to link the benefit of weight savings to the indirect energy savings mentioned early on in this thesis. The weight savings in the structural body of the hopper railcar would correspond to an increase in the weight of the cargo because these hopper railcars are limited only to a maximum weight on track. The increase in the cargo load would correspond to an increase in the internal pressure felt by the sidewalls. Therefore, the design and analysis of the hopper railcar should take this into consideration when the entirety of the sidewall is modelled in FEA software.

The FRP panels were then further modified to be thinner at the top than they are at the bottom to further reduce the weight. This was achieved by performing stress and strain failure analyses and by maintaining the stress levels in accordance with the requirements listed in Table 3. As a result, 13% further reduction per panel was achieved in the e-glass/epoxy panel. This also translates to 5.9% potential weight reduction from the total empty weight. On the other hand, the untailed and tailed aramid/epoxy panels offered 5.7% and 6.4% potential weight reduction from the total empty weight, respectively. Therefore, aramid/epoxy was a better option than e-glass/epoxy because it offered the maximum estimated weight reduction. The sidewall design was chosen to be tailored at the top to further reduce the weight.

From the literature review, no company described the alteration to the sidewall design relative to this concept except FreightCar America in their VersaFlood hybrid

railcar. From Figure 57, the top part of the sidewall was made with aluminium; while the bottom was made from steel [63].



Figure 57: Open hopper railcar with a hybrid steel and aluminium design [64].

Aluminium did offer significant potential weight reduction versus steel as well, as seen from Table 14. However, the Government of Canada had a negative previous experience with aluminium hopper railcars in the past. In 2009, the Government of Canada had ordered the removal of all remaining aluminium hopper railcars in the fleet due to structural defects that raised serious safety concerns [65]. The report does not discuss these safety concerns nor the specific structural defects that lead to the removal of the cars from service. However, it is possible to predict some of these structural defects. Aluminium is very sensitive to bending and has lower fatigue index than steel. Therefore, it is possible that crack propagations exceeded their critical limits and deemed the structures, be it the sidewalls or frame, unsafe. It was reported in [66] that most of the cars had a service life of 30 to 32 years, whilst they were designed to have a useful life of 40 years.

Ideally, the FRP panels and stiffeners would be combined into a single unified structure without mechanical joints or fasteners. In this case, the FRP panels can be

connected to the frame using mechanical fasteners, i.e. bolted joints. The side sill and stiffeners will be mounted on the outside surface of the sidewall.

Bolted joints or mechanically fastened joints offer simple joint configuration that is not environmentally sensitive [37]. Bolted joints, if not designed carefully, can cause bearing failures due to the low bearing and transverse strength of FRP [37]. Figure 58 illustrates the failure modes of a FRP joint. Failure type depends on the ratio of the edge distance to diameter of the fastener hole (e/d), and the ratio of the effective width to diameter (w/d). In theory, the joints in quasi-isotropic laminate fail in bearing as the values of w/d and e/d increase. Usually, the desired failure modes are bearing or net tension/compression [37].

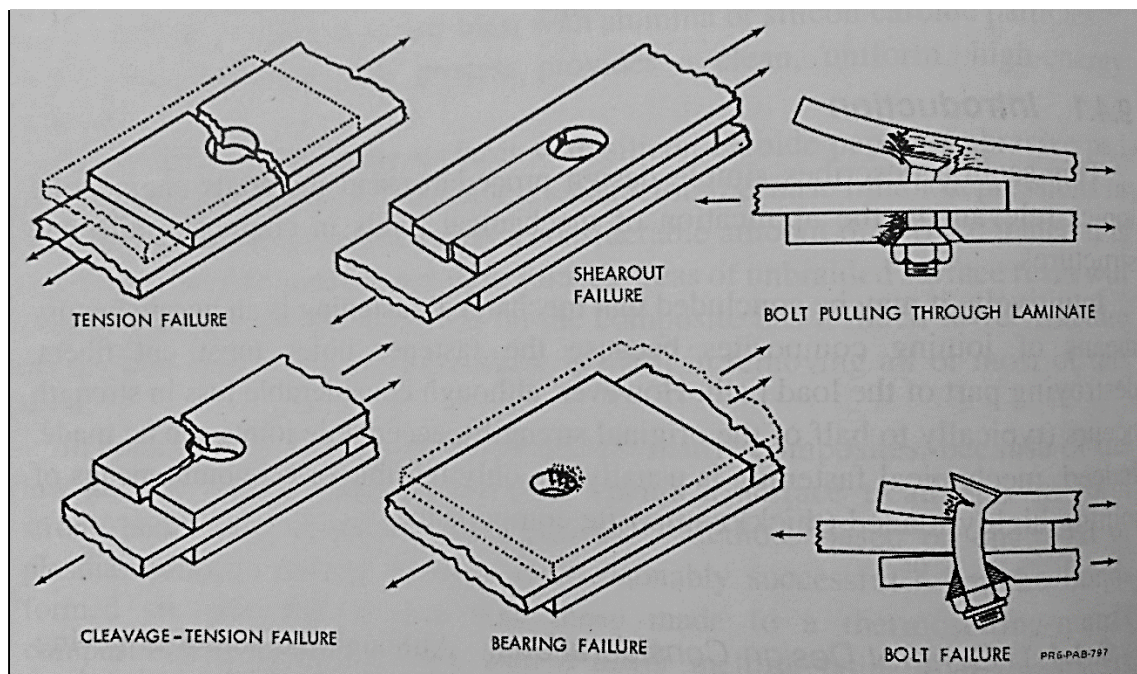


Figure 58: schematic illustration of the main failure modes in bolted joints of FRP [37].

Chapter 6

Conclusions

This chapter summarizes several significant conclusions established from this research, and provides key recommendations for future work.

6.1 Conclusions

Conclusions drawn from this preliminary study on the use of fibre reinforced polymers in structural components of hopper railcars are as follows:

- Weight reduction in freight railcars has higher indirect energy savings - more than four times that of direct energy savings because freight railcars are weight limited cargo. A 10% weight reduction per freight railcar corresponds to 5% energy saving, assuming 180 kJ/gross t-km.
- The selection of a specific railcar type to improve depended on the usage frequency and number of cars used by CP and CN. A railway performance study proved quantitatively that hopper railcars accounted for the greatest portion of *cars on line*.
- A piece cut from the sidewall of a decommissioned steel hopper car was used as a baseline for comparison. The mechanical properties and type of steel was determined through a series of metallographic, tensile, and hardness tests to be AISI 1020 steel.

- VARTM process, a low-cost and out-of-autoclave manufacturing technique, was selected as a suitable manufacturing method to fabricate the sidewall panels.
- Fabrication trials using VARTM process unfolded few technical challenges with the resin infusion process. Dry spots and high void content were the main defects detected in the designed panels. Resin flow simulation software was recommended to be integrated with the manufacturing process to increase the cost-effectiveness of VARTM process by providing a way to virtually verify and optimize the mould configuration.
- Using aramid/epoxy in the structure of the sidewalls resulted in a potential weight reduction of 6.4% from the total empty weight of a hopper railcar with flat sidewalls. The new sidewall design was tailored to be thinner at the top to further reduce the weight of FRP panel, whilst meeting the design requirements listed in the AAR standards.

6.2 Recommendations

The methods employed were considered an initial stage in developing a FRP sidewall structure in a hopper railcar. The following areas should be further investigated:

- The environmental effects on the outside surface of the composite railcars needs to be experimentally studied. Moisture absorption and UV degradation of the surface matrix depends on the FRP material used and operating conditions [37]. Depending on the operating conditions, diffusion of moisture will eventually saturate the material to an equilibrium concentration [37]. By knowing the

moisture-content level, mechanical tests can be reproduced in the lab to determine the long-term effect of moisture on the performance of the material.

- The inside surface of the sidewall has to be experimentally studied against wear and abrasion using one of the major abrasion tests: ball milling, pin-on-disk wear test, and abrasive wear test. As seen from the fabrication trial, VARTM process produces low quality surface finish on one of the surfaces. surface preparation or surface coating can be necessary to reduce the effect of abrasion and wear on the inside surface. The addition of ceramic powder coating, such as silicon carbide or alumina powders, can be used to improve the wear resistance of the FRP panels.
- The analysis of the new FRP sidewall design needs to include fatigue testing due to: loading and unloading of the cars and the dynamic movement of the hopper railcars. In addition, the sidewalls will experience impact forces due to the loading of granular material as they spread out inside the hopper railcar. Therefore, the analysis of the design should also incorporate this to verify the stacking sequence.
- This thesis aimed at the substitution of steel with RFP materials in the side panels. Similar FE analyses can be performed to include the side end panels and the end plates for a more comprehensive design for a hopper railcar.
- The challenges faced in the VARTM manufacturing trials can be minimized by using software that models resin infusion. Software such as Liquid Injection Molding Simulation (LIMS) and PAM-RTM[®] can simulate mould filling in VARTM processes. LIMS and PAM-RTM have the capability to perform three-dimensional mould filling simulations of various thermoset resin transfers [67] [68]. LIMS enables the user to virtually model and predict the flow behaviour

of the resin in the infusion stage [67]. In addition, LIMS has the capability to incorporate multiple injection gates, vents in the mould. The gates and vents can be modified to open/close sequentially during the simulation, allowing for the user to interrogate the state of mould filling [67]. One key feature offered by LIMS is the ability to monitor the infusion process in real time to compare the real life infusion process to the simulated process [67]. On the other hand, PAM-RTM has the capability to estimate the optimal injection locations and sequential opening/closing of the gates [68]. In addition, PAM-RTM is capable of predicting the porosity level and risk of dry spot-appearance [68]. Either LIMS or PAM-RTM can be utilized to model the large sidewall panels. Similar to FEA software, these programs can increase the cost-effectiveness of VARTM fabrication process by providing a way to virtually verify and optimize mould design. Hence, having an optimal mould design allows for a high-quality repeatability for consistent parts that does not solely depend on the human experience.

- The clamped condition of the sidewall was later discovered to be an unattainable condition in real life given the railcar configuration. Future work on this setup should focus on a partially clamped or bonded joint conditions with the bottom side sills.

References

- [1] “Rail Facts,” Railway Association of Canada, [Online]. Available: <http://www.railcan.ca/education/facts>. [Accessed 13 Oct 2014].
- [2] E. Canada, “Canada's Emission Trends 2012,” 2012.
- [3] “National Inventory Report 1990-2013: Greenhouse Gas Sources and Sinks in Canada - Executive Summary,” Environment Canada, 17 April 2015. [Online]. Available: <http://ec.gc.ca/ges-ghg/default.asp?lang=En&n=5B59470C-1&offset=2&toc=show>. [Accessed 5 December 2015].
- [4] *Canada Gazette, Part I*, vol. 140, p. 42, 21 Oct 2006.
- [5] W. D. Keith Bush, “Flow Through Rail Road Freight Car”. US Patent US 7536957 B2, 26 May 2009.
- [6] Railway Association of Canada , “Submission to Transport Canada, Environmental Policy : Response to the Public Consultati,” 2011.
- [7] “2013 Investor Fact Book, Balancing Operational and Service Excellence,” Canadian National Railway, 2013.
- [8] “Railroad Performance Measures,” [Online]. Available: www.railroadpm.org. [Accessed 28 Oct 2014].
- [9] “2013 Rail Trends,” Railway Association of Canada, 2013.
- [10] “Railroad Equipment,” CSX, [Online]. Available: http://www.csx.com/index.cfm/customers/equipment/railroad-equipment/#boxcar_specs. [Accessed 19 Oct 2014].
- [11] Canadian Pacific, “2008 Corporate Profile + Fact Book,” 2008.

- [12] “Locomotive Emissions Monitoring Program 2011 – 2015, Action Plan for Reducing GHG Emissions,” Railway Association of Canada.
- [13] R. A. o. Canada, “2012 Rail Trends,” 2012.
- [14] “Emission data for years 1990-2011 (Tables),” Railway Association of Canada, [Online]. Available: www.railcan.ca. [Accessed 26 Oct 2014].
- [15] H. Helms, U. Lambrecht and U. Hopfner, “Energy savings by light-weighting,” Institute for Energy and Environmental Research, , 2003.
- [16] B. Solomon and P. Yough, “Coal Trains, The History of Railroading and Coal in the United States,” Voyageur Press, Minneapolis, USA, 2009.
- [17] Alcan International Limited, “Design and Testing of a Self Supporting Aluminum Covered Hopper Car,” 1962.
- [18] T. Johnson, “History of Composites, The evolution of Lightweight Composite Materials,” About Money, [Online]. Available: <http://composite.about.com/od/aboutcompositesplastics/a/HistoryofComposites.htm>. [Accessed 18 Oct 2014].
- [19] D. Ruhmann, “The Design, Fabrication and Testing of the Glasshopper Prototype Covered Hopper Rail Cars,” *Composite Structures*, vol. 27, pp. 207 - 213, 1994.
- [20] M. Labordus, *RE: Weight Saving*, 2014.
- [21] J. Snodgrass, “Composite on Road, Rail, Air and Sea,” Plastic News Europe, 20 Oct 2014. [Online]. Available: <http://www.europeanplasticsnews.com/subscriber/headlines2.html?id=5095>. [Accessed 26 Oct 2014].
- [22] K. Louisville, “Walmart Debuts Futuristic Truck, Walmart Advanced Vehicle Experience Showcases Cutting Edge Innovations,” Walmart, 26 March 2014.

- [Online]. Available: <http://news.walmart.com/news-archive/2014/03/26/walmart-debuts-futuristic-truck>. [Accessed 5 Nov 2014].
- [23] Railway Association of Canada, “Interchange Magazine - Fall 2013”.
- [24] “Hopper Cars,” American Railcar Leasing, [Online]. Available: <http://www.arleasing.com/Pages/Products/Hoppers.aspx>. [Accessed 14 July 2015].
- [25] Midwest Railcar Corporation, “Covered Hopper - 4750 Cubic Feet,” [Online]. Available: <http://www.midwestrailcar.com/equipHopper4750.html>. [Accessed 15 July 2015].
- [26] R. V. Wright and C. N. Winter, Car Builders' Cyclopedia of American Practice, 9th edition., New York: Simmons-Boardman, 1919.
- [27] “35ton ballast hopper car,” Wikimedia Commons, 2006. [Online]. Available: http://commons.wikimedia.org/wiki/File:35ton_ballast_hopper_car.jpg. [Accessed 10 June 2015].
- [28] Dederail Aviation Administration, “Composite Aircraft Strucutes, AC 20-107B,” U.S. Department of Transportation, 2009.
- [29] “Manual of Standards and Recommended Practices, Section C - Part II: Design,, Fabrication, and Constuction of Freight Cars,” Association of American Railroads, USA, 2011.
- [30] D. G. Rethwisch and W. D. C. Callister , Materials Science and Engineering: an Introduction, 9th ed., Hoboken, NJ: John Wiley & Sons, Inc., 2014.
- [31] ASTM International, *ASTM E18-15, Standard Test Methods for Rockwell Hardness of Metallic Materials*, West Conshohocken, PA: www.astm.org, 2015.

- [32] ASTM International, *ASTM E140-12be1, Standard Hardness Conversion Tables for Metals Relationship Among Brinell Hardness, Vickers Hardness, Rockwell Hardness, Superficial Hardness, Knoop Hardness, Scleroscope Hardness, and Leeb Hardness*, West Conshohocken, PA: www.astm.org, 2012.
- [33] ASTM International, *ASTM E8 / E8M-15a, Standard Test Methods for Tension Testing of Metallic Materials*, West Conshohocken, PA: www.astm.org, 2015.
- [34] ASTM International, *ASTM E3-01, Standard Practice for Preparation of Metallographic Specimens*, West Conshohocken, PA: www.astm.org, 2001.
- [35] M. Senn and C. Degringy, “FN 655.13.01 - Fe Alloy - Modern Times - Switzerland,” Micorr, [Online]. Available: <http://micorr.org/artefacts/67/>. [Accessed 5 January 2016].
- [36] G. F. Vander Voort, *ASM Handbook Volume 9: Metallography and Microstructures*, ASM International, 2004.
- [37] A. Baker, S. Dutton and D. Kelly, *Composite Materials for Aircraft Structures*, Reston, Virginia: American Institute of Aeronautics and Astronautics, Inc., 2004.
- [38] Illinois Department of transportation, “Fiberglass Reinforced Polymer Composite Bridge Deck Construction in Illinois, Construction report, Physical Research Report No. 145,” Bureau of Materials and Physical Research, Springfield, Illinois, 2002.
- [39] F. Takeda, K. Hayashi, Y. Suga, S. Nishiyama, Y. Komori and N. Asahara, “Research in the Application of the VaRTM Technique to the Fabrication of Primary Aircraft Composite Structures,” *Mitsubishi Heavy Industries, Ltd.*, vol. 42, p. 5, 2005.

- [40] R. A. Witik, F. Gaille, R. Teuscher, H. Ringwald, V. Michaud and J.-A. E. Manson, "Economic and environmental assessment of alternative production methods for composite aircraft components," *Journal of Cleaner Production*, Vols. 29-30, pp. 91 - 102, 2012.
- [41] A. R. Upadhya, G. N. Dayananda, G. M. Kamalakannan, J. Ramaswamy Setty and J. Christopher Daniel, "Autoclaves for Aerospace Applications: Issues and Challenges," *International Journal of Aerospace Engineering*, vol. 2011, pp. 1-11, 2011.
- [42] G. Gardiner, "Inside Manufacturing: An Autoclave for the 787 Center Wing Box," *Composite World*, 3 January 2007. [Online]. Available: <http://www.compositesworld.com/articles/inside-manufacturing-an-autoclave-for-the-787-center-wing-box>. [Accessed 3 October 2015].
- [43] Dry Composite, "Resin Infusion Techniques in the Aerospace Industry," [Online]. Available: <http://www.drycomposites.com/resin-infusion-techniques-in-the-aerospace-industry/#respond>. [Accessed 2 October 2015].
- [44] T. Sakagawa, M. Yamashita, F. Kimata, Y. Komori and F. Takeda, "Development of Advanced Vacuum-assisted Resin Transfer Molding Technology for Use in an MRJ Empennage Box Structure," *Technical Review*, vol. 45, p. 4, 2008.
- [45] "Bombardier Learjet 85- OoA prepreg and infusion process," Dry Composites, [Online]. Available: <http://www.drycomposites.com/bombardier-learjet-85-ooa-prepreg-and-infusion-process/>. [Accessed 4 October 2015].
- [46] G. Gardiner, "C Series composite wing," *Composites World*, 14 October 2013. [Online]. Available: <http://www.compositesworld.com/blog/post/cseries-composite-wing>. [Accessed 3 October 2015].

- [47] L. Catella, "Support assembly for composite laminate materials during roll press processing". USA Patent US 7871682B2, 18 Jan 2011.
- [48] E. J. Rigas, T. J. Mulkern, S. P. Nguyen and S. M. Walsh, "Affordable Thick Composite Processing for Army Applications," in *American Society of Composites, Fourteenth International Conference Proceedings*, Fairborn, Ohio, 1999.
- [49] B. P. Burns, . C. P. R. Hopple, . J. Newill, L. W. Burton, . J. T. Tzeng and . W. Drysdale, "Army Perspective on Composite Materials," in *American Society of Composites, Fourteenth International Conference Proceedings*, Fairborn, Ohio, 1999.
- [50] T. G. Gutowski, *Advanced Composites Manufacturing*, New York: John Wiley and Sons, 1997.
- [51] J. W. Gillespie, D. Heider, W. Li, M. Endrulat, K. Hochrein, M. G. Dunham and C. J. Dubois, "Process and Performance Evaluation of the Vacuum-Assisted Process," *Journal of Composite Materials*, vol. 38, no. 20, pp. 1803 - 1814, 2004.
- [52] Y. S. Song, J. W. Gillespie, D. Heider and C. Niggemann, "Experimental Investigation of the Controlled Atmospheric Pressure Resin Infusion (CAPRI) Process," *Journal of Composite Materials*, vol. 42, no. 11, pp. 1049 - 1061, 2008.
- [53] P. K. Mallick, *Fiber-Reinforced Composites (Materials, Manufacturing, and Design)*, 3rd edition, Boca Raton, Florida: Taylor & Francis Group, LLC., 2008.
- [54] B. N. Fedulov, F. K. Antonov , A. A. Safonov, A. E. Ushakov and S. V. Lomov, "Influence of fibre misalignment and voids on composite laminate strength," *Journal of Composite Materials*, vol. 49, no. 23, pp. 2887 - 2896, 2015.

- [55] F. C. Campbell, Manufacturing Processes for Advanced Composites, Oxford, UK: Elsevier Advanced Technology, 2003.
- [56] M. J. M. a. N. Shapiro, Fundamentals of Engineering Thermodynamics, USA: John Wiley & Sons, Inc, 2011.
- [57] C. P. Heins, Applied plate theory for the engineer, Lexington, Massachusetts: Lexington Books, 1976.
- [58] H. Reissmann, Elastic plates: theory and application, New York: Wiley, 1988.
- [59] J. N. Reddy, Theory and Analysis of Elastic Plates and Shells, 2nd edition, Boca Raton, FL: Taylor & Francis Group, LLC, 2007.
- [60] T. K. Eduard Ventsel, Thin Plates and Shells Theory: Analysis, and Applications, University Park, Pennsylvania: Marcel Dekker, Inc, 2001.
- [61] Dassault Systèmes, “21.5.6 Viewing a composite layup, Abaqus/CAE User's Manual, version 6.7,,” 2007.
- [62] A. A. Bakers, S. Dutton and D. Kelly, Composites Materials for Aircraft Structures, 2nd ed., American Institute of Aeronautics and Astronautics, 2004.
- [63] “Versaflood Hybrid Steel And Aluminum Aggregate Car,” HelloTrade, [Online]. Available: <http://www.hellotrade.com/freightcar-america-johnston/versaflood-hybrid-steel-and-aluminum-aggregate-car.html>. [Accessed 6 January 2016].
- [64] FreightCar America, Inc, “manufacturing,” [Online]. Available: <http://www.freightcaramerica.com/wordpress/index.php/manufacturing/>. [Accessed 24 December 2015].
- [65] Transport Canada, “Government of Canada Hopper Car Fleet 2011 Annual Report,” 2011.

- [66] A. Ewins, "Days numbered for hopper cars," The Western Producers, 17 April 2008. [Online]. Available: <http://www.producer.com/2008/04/days-numbered-for-hopper-cars/>. [Accessed 6 January 2016].
- [67] S. G. Advani, "LIMS," University of Delaware , 2015. [Online]. Available: <http://sites.udel.edu/advani/software/lims/>. [Accessed 24 December 2015].
- [68] Get it Right, "PAM-RTM," [Online]. Available: <https://www.esi-group.com/software-services/virtual-manufacturing/composites/pam-rtm>. [Accessed 24 December 2015].
- [69] E. Canada, "Criteria Air Contaminants and Related Pollutants," 24 April 2013. [Online]. Available: <http://www.ec.gc.ca/air/default.asp?lang=En&n=7C43740B-1>. [Accessed 3 Oct 2014].
- [70] NASA , "Out of Autoclave Wind Turbine Blade Manufacturing Method," [Online]. Available: <http://technology.nasa.gov/t2media/tops/pdf/LAR-TOPS-37.pdf>. [Accessed 18 October 2015].
- [71] N. Nu, "Composites and Their Properties," in *Advanced Composite Materials by Resin Transfer Molding for Aerospace Applications*, InTech, 2012.
- [72] C. S. Y. G. J. & H. D. Niggemann, "Experimental Investigation of the Controlled Atmospheric Pressure Resin Infusion (CAPRI) Process," *Journal of composite materials*, vol. 42, no. 11, pp. 1049 - 1061, 2008.
- [73] Transport Canada, "Government of Canada Hopper Car Fleet 2011 Annual Report," 2011.

APPENDICES

A - Weekly Railroad Traffic Carload and Intermodal

Traffic Category Definitions

NO.	Category	Description of Traffic Included	CN Supplemental Description
1.	Grain	Grains (wheat, corn, sorghum, barley, oats, <i>etc.</i>) and oilseeds (soybeans, <i>etc.</i>).	Grain - whole grains - includes wheat, barley, corn and soybeans.
2.	Farm Products, Ex. Grain	All farm products except grains and oilseeds (Category No. 1).	Farm Products - includes oilseeds, Peas and Lentils.
3.	Metallic Ores	All metallic ores (iron, bauxite or aluminum, copper, <i>etc.</i>).	
4.	Coal	Bituminous, anthracite, and lignite coal.	
5.	Crushed Stone, Sand and Gravel	Crushed or broken stone, sand, and gravel.	
6.	Non-metallic Minerals	Non-metallic minerals except crushed stone, sand and gravel (phosphate rock, rock salt, sulphur, clay, <i>etc.</i>).	
7.	Grain Mill Products	Flour, prepared feed, cereal preparations, milled rice, wet corn milling products, distillers dried grains with soluble (DDGS), soybean cake, and other milled grains.	Grain Mill Products - includes DDG's and Soymeal (note: excludes Ethanol).
8.	Food and Kindred Products	All food and feed products, except Grain Mill Products (Category No. 7).	Food and Kindred - includes Canola Meal, Malt and Soy/Canola Oil.
9.	Primary Forest Products	Pulpwood logs, pulpwood and other wood chips.	

10.	Lumber and Wood Products	All lumber and wood products (excluding furniture) except Primary Forest Products (Category No. 9).	
11.	Pulp, Paper, and Allied Products	Paper, pulp mill products, paperboard or fibreboard, and containers or boxes.	
12.	Chemicals	Industrial chemicals and gases, alcohols (including ethanol), plastics and resins, fertilizer, and hazardous materials for which the non-hazmat STCC is not known.	
13.	Petroleum Products	Crude petroleum and natural gasoline, and all products of petroleum refining (gasoline, jet or high volatile fuels; distillate fuel oil; lubricating oils; asphalt and tar; liquefied gases; <i>etc.</i>).	
14.	Stone, Clay and Glass Products	All types of glass products; hydraulic cement; structural clay products; concrete, gypsum or plaster products; and abrasives or asbestos products.	
15.	Coke	Coal or coke briquettes, petroleum coke, and coke produced from coal.	
16.	Metals and Products	Primary metal products (iron and steel, aluminum, copper, brass, <i>etc.</i>), and fabricated metal products (hand tools, cutlery and hardware; structural metal products; metal stampings, <i>etc.</i>)	

17.	Motor Vehicles and Equipment	Motor vehicles, passenger car bodies, bus or truck bodies, motor vehicle parts and accessories, and used vehicles.	
18.	Iron and Steel Scrap	Iron and steel scrap and waste	
19.	Waste and Other Scrap	All other waste and scrap materials (<i>i.e.</i> , except iron and steel scrap), and hazardous wastes.	

B - Specifications of All Published North American Existing Hopper Cars

Model	Lading	Empty Weight [kg]	Gross Rail Load [kg]	Load Limit [kg]	Capacity [Cm]	Centre/Stub Sill
Aluminium Quad Hopper Car	Coal and rocks	23,541	129,727	106,186	118	C
VersaFlood hybrid steel and aluminium aggregate car	Sand, rock or minerals	25,583	129,727	104,145	79	C
Aggregate (steel)	Sand, rock or minerals	27,079	129,727	102,648	75	C
AutoFlood II (Aluminium)	Coal and Coke	22,725	129,727	107,002	133	C
T3250 Covered Hopper (steel)	Cement	24,948	129,727	104,780	92	C

4250 Covered Hopper (steel)	soda ash and potash	25,855	129,727	103,873	120	C
5188 Covered Hopper (steel)		28,123	129,727	101,831	147	C
National Steel Car (Steel)	Cement, roof granular, or sand	24,948	129,727	104,780	177	C

C – Setup for VARTM manufacturing

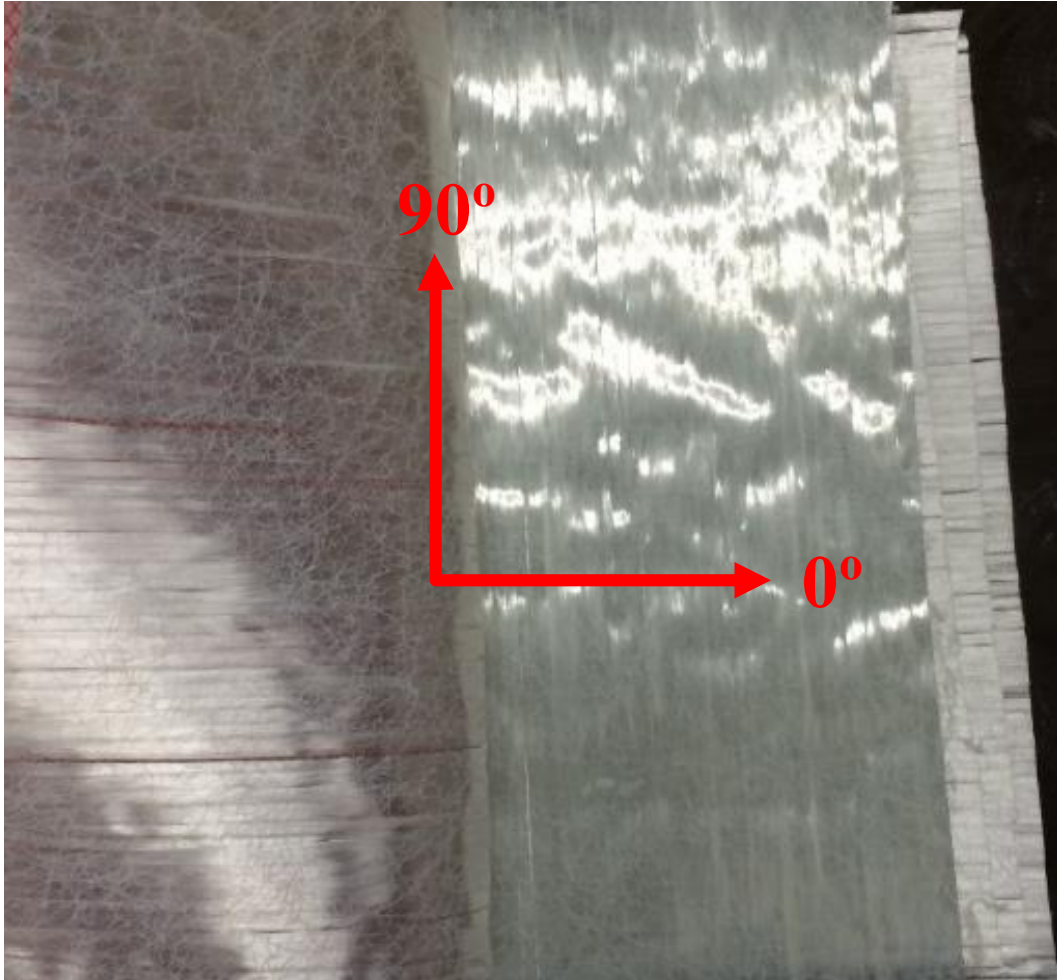


Figure 59: [0/90/0/0/90/0] stacking sequence of the fibreglass preform.



Figure 60: Placement of Peel Ply (green film) under the Distribution Medium (red mesh) and the breather cloth (white fabric).



Figure 61: Placement of the resin distribution channel to the left side for the inlet under the peel ply.

D – FE Analysis of a Thin Plate Model Using ABAQUS

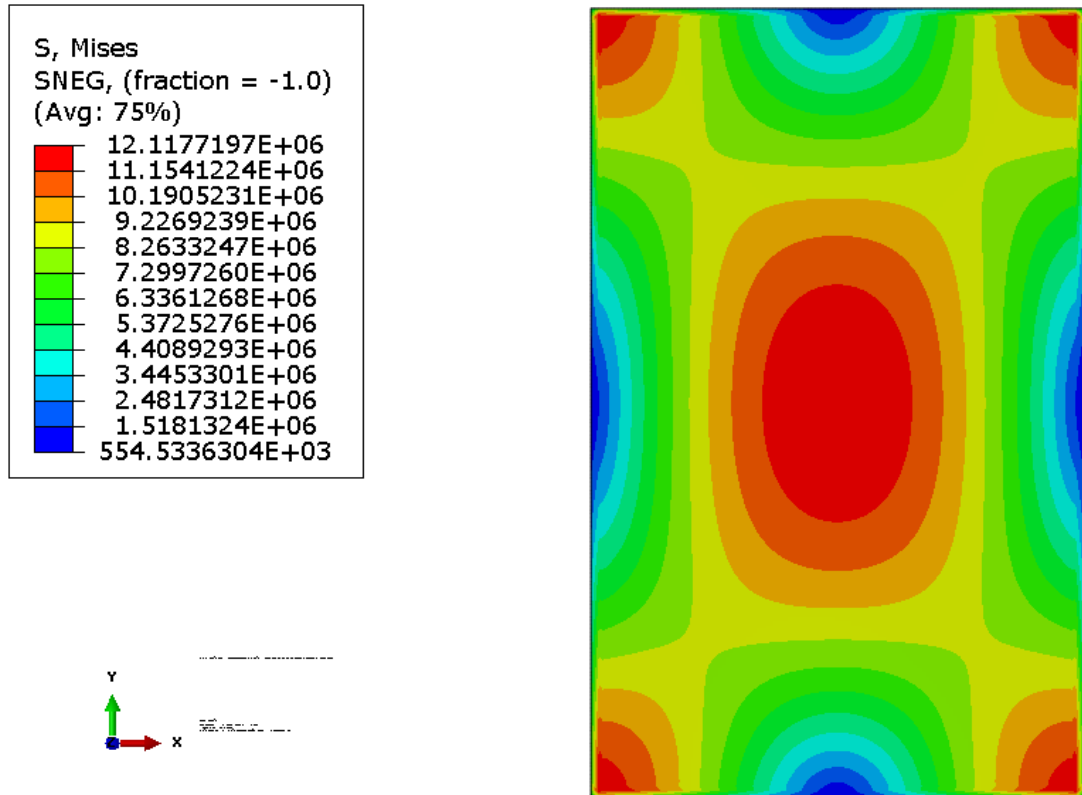


Figure 62: Stress distribution, in 2600 Pa, for a steel plate with SSSS boundary conditions.

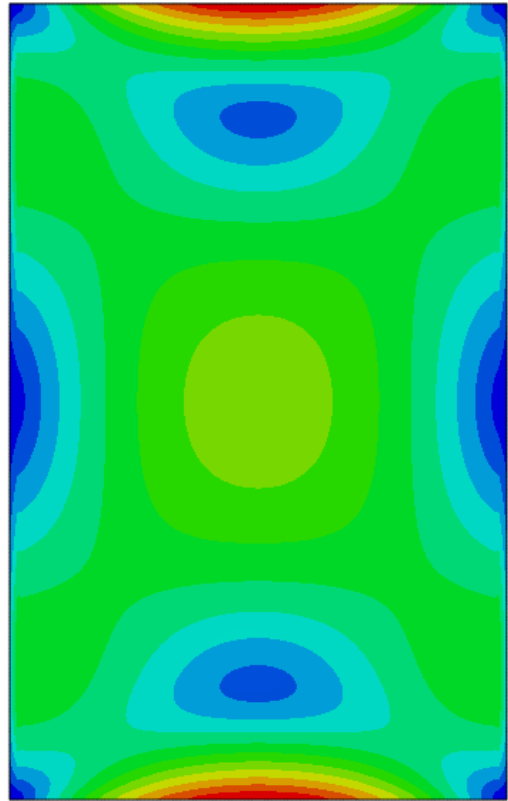
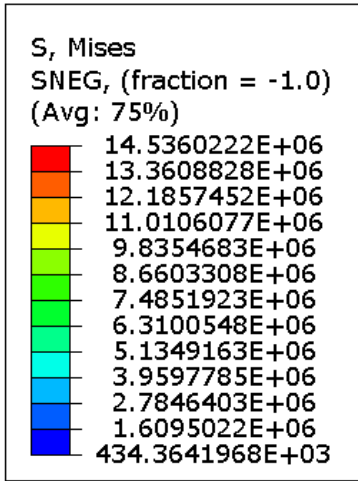


Figure 63: Stress distribution, in 2600 Pa, for a steel plate with CCSS boundary conditions.

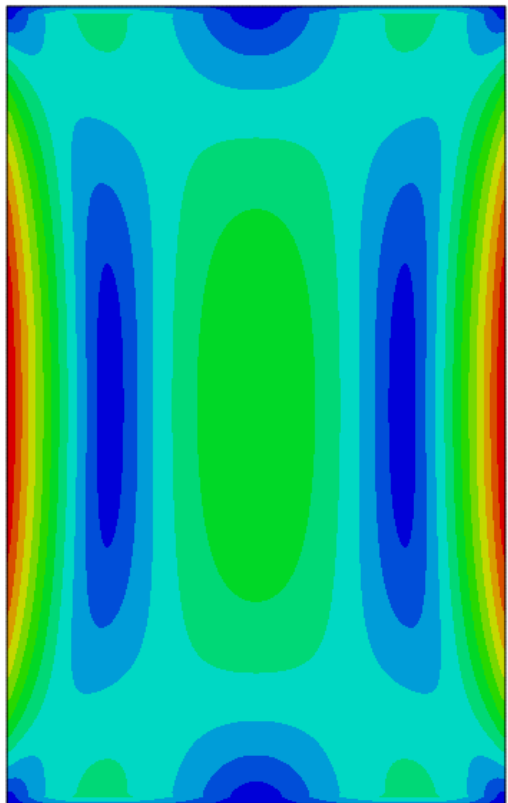
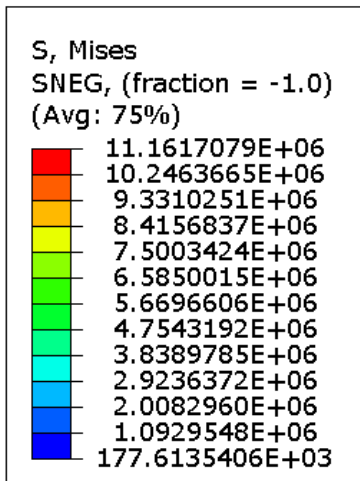


Figure 64: Stress distribution, in 2600 Pa, for a steel plate with SSCC boundary conditions.

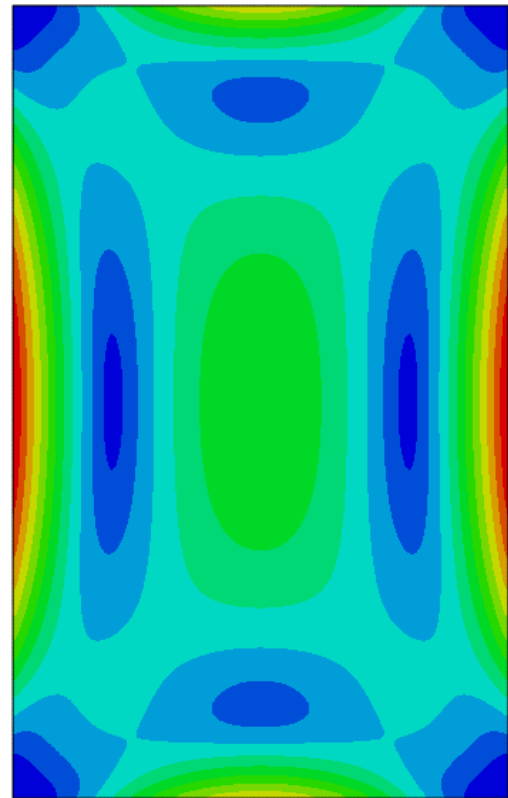
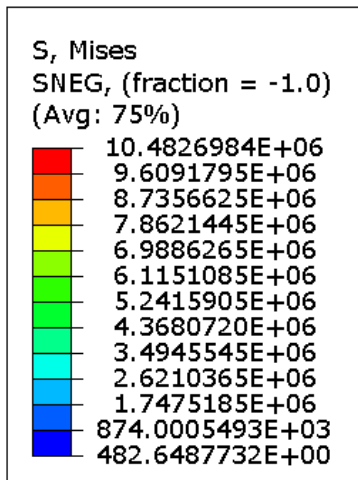


Figure 65: Stress distribution, in 2600 Pa, for a steel plate with CCCC boundary conditions